Technische Universität München

Lehrstuhl für Energiesysteme

Diplomarbeit

(Theoretisch)

von cand. Ing. Patrick Wagner

Thermodynamic simulation of solar thermal power stations with liquid salt as heat transfer fluid

Betreuer: Dipl.-Ing. Christoph Wieland

Ausgegeben: 01.04.2012

Abgegeben: 28.09.2012

Prof. Dr.-Ing. Hartmut Spliethoff

Eidesstattliche Erklärung

Hiermit versichere ich, die vorliegende Arbeit selbständig und ohne Hilfe Dritter angefertigt zu haben. Gedanken und Zitate, die ich aus fremden Quellen direkt oder indirekt übernommen habe sind als solche kenntlich gemacht. Diese Arbeit hat in gleicher oder ähnlicher Form noch keiner Prüfungsbehörde vorgelegen und wurde bisher nicht veröffentlicht.

Ich erkläre mich damit einverstanden, dass die Arbeit durch den Lehrstuhl für Energiesysteme der Öffentlichkeit zugänglich gemacht werden kann.

_____, den _____   _____

<div align="right">Unterschrift</div>
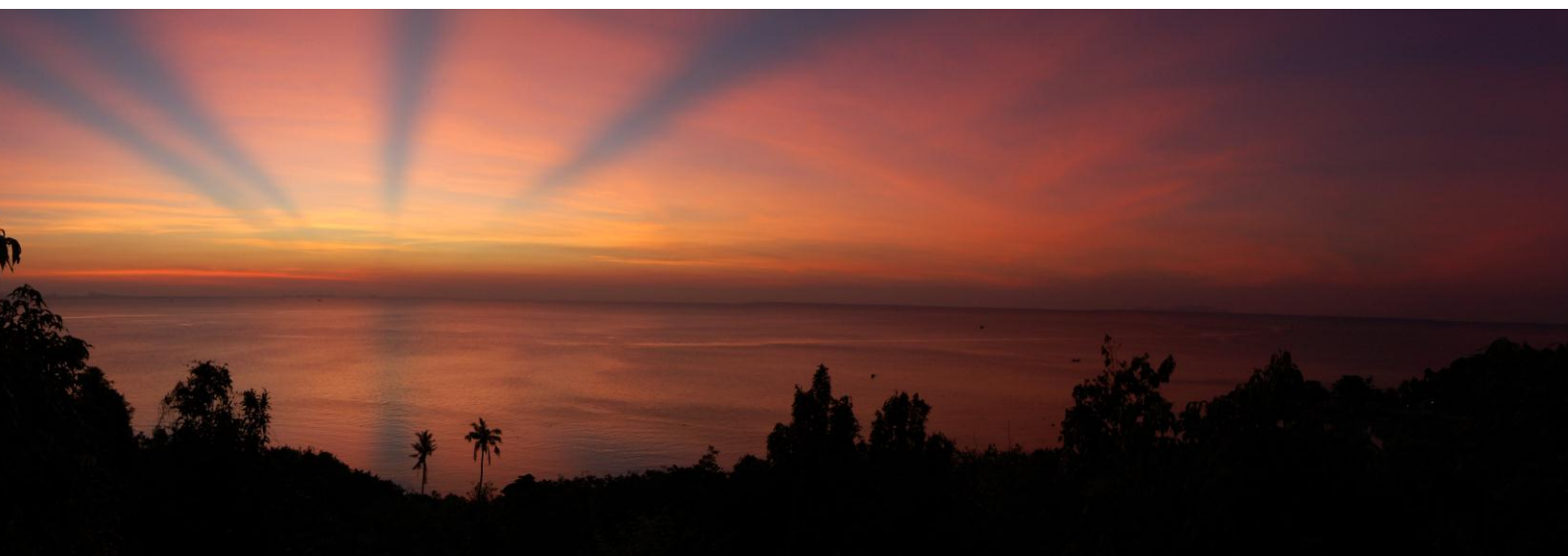
Abstract

This thesis was written at the Deutsches Zentrum für Luft- und Raumfahrt e. V. (German Aerospace Center) in the Institute of Solar Research, Stuttgart. The adviser was Dr.-Ing. Michael Wittmann from the Line Focus Systems division.

The Gemasolar solar power tower plant uses molten salt as heat transfer fluid and is therefore the first commercial project to apply this technology. Current research and development in line focusing systems is concentrated on transferring this proved salt technology to solar thermal power stations with parabolic trough collectors.

This thesis identifies the economic performance of such a power station. To that end, a transient thermodynamic model is implemented into the commercial software tool EBSILON®Professional. The system behavior of the solar field is modelled in transient and pseudo-transient mode for the power block.

The model discretized one year into 10-minute intervals in order to calculate the levelized electric costs (LECs) for a 125-MW_e reference plant with live steam parameters of 150 bar and 510° C. The solar field layout is assumed to be a 2 H layout with 352 collector loops, each consisting of four Eurotrough ET150 collectors (solar multiple of 2.233). The storage system is able to feed the steam generator for 10 hours.

Three different years with different annual averaged direct normal irradiation averaged annual sums were compared. Given the 90% confidence interval $(50\% + 45\%)$, the LECs are between 0.117 and 0.190 €/kWh_e (2659 kWh/m²/y), 0.136 and 0.221 €/kWh_e (2300 kWh/m²/y), and 0.149 and 0.243 €/kWh_e (2095 kWh/m²/y). The mode LECs are 0.149 €/kWh_e, 0.172 €/kWh_e, and 0.190 €/kWh_e.

Key Words: Solar thermal power station, parabolic trough collector, molten salt, annual yield calculation

Table of contents

List of figures

List of tables

Nomenclatur

AH	Auxiliary heater
ASE	Archimede Solar Energy
BMU	Bundesministerium für Umwelt, Naturschutz und Reaktorsicherheit
BOP	Balance of plant
cdf	Cumulative density function
CSP	Concentrating solar power
CT	Cold tank
Dii	Desertec Industrial Initative
DLR	Deutsches Zentrum für Luft- und Raumfahrt
EBSILON	Energy balance and simulation of the load response of power generating or process controlling network structures
Eco	Economiser
ENEA	National Agency for New Technologies, Energy and the Environment
ENEL	Ente nazionale per l'energia elettrica
Eva	Evaporator
FAME	French Agency for the Management of Energy
HPS	High Performance Solarthermie
HT	Hot tank
HTF	Heat transfer fluid
IAM	Incident angle modifier
LEC	Levelized electric cost

MENA	Middle East and North Africa
MM	Mass multiplier
NREAP	Renewable Energy Projections as Published in the National Renewable Energy Action Plans of the European Member States
NREL	National Renewable Energy Laboratory
P	Profile
PB	Power block
PCS	Prova collettori solari
pdf	Probability density function
PP	Power plant
PTC	Parabolic trough collector
PTR	Parabolic trough receiver
PV	Photovoltaic
RES-E	Renewable energy sources for electricity
RH	Reheater
SCA	Solar collector assembly
SCE	Solar collector elements
SEGS	Solar electric generation system
SF	Solar field
SG	Steam generator
SH	Superheater
TS	Time series time step

Subscripts

Abs	Absorber
amb	ambient
Ape	Aperture
b	bending
br	branch
clean	cleanliness
D	at the design point
dis	discount
e	electrical
em	employee
end	end losses
f	focus
f1	feeder 1
f2	feeder 2
geo	geometric
h	header
hl	heat losses
i	inner
i	incident
IS	indirect storage
j	numbering element
k	numbering element

l   numbering element

off-D   off-design

rep   representative

rowdist   row distance

s   sun

shad   shading

th   thermal

u   upper

w-s   water-steam

Notation

Notation	Unit	Meaning
A	[m²]	area
a	[-]	factor
$\boldsymbol{a}$	[m²/s]	thermal diffusivity
C	[-]	geometric concentration
c	[J/kg/K]	specific heat capacity
CRF	[-]	capital recovery factor
d	[m]	distance, diameter
DNI	[W/m²]	direct normal irradiance
e	[-]	exponent
f	[-]	focus
$f(x)$	[-]	cumulative density function
G	[€]	cost for gas
I	[€]	investment
IAM	[-]	incident angle modifier
INS	[€]	cost for insurance
K	[-]	correction factor
k	[W/m]	specific heat loss
l	[m]	length
LEC	[€/kWh$_e$]	levelized electric cost
m	[kg]	mass

$\dot{m}$	[kg/s]	mass flow
Nu	[-]	Nusselt number
n	[-]	number
OM	[€]	cost for operation and maintenance
P	various	specific cost
p	[Pa]	pressure
Pr	[-]	Prandtl number
$P(x)$	[-]	probability density function
Q	[J]	energy
$\dot{Q}$	[W]	heat flow
q	[J/m²]	specific energy
$\dot{q}$	[W/m²]	specific heat flow
r	[kg/s/s]	Ramp-up factor
Re	[-]	Reynolds number
s	[J/m³/K]	volumetric heat capacity
$\boldsymbol{s}$	[J/kg/K]	entropy
T	[K]	temperature
t	[s]	time
$\boldsymbol{t}$	[m]	thickness
U	[W/m²/K]	overall heat transfer coefficient
v	[m/s]	velocity
w	[m]	width

Greek

α	[W/m²/K]	heat transfer coefficient
$\boldsymbol{\alpha}$	[-]	absorptance
α_s	[°]	sun azimuth angle
γ_s	[°]	sun height angle
γ_θ	[-]	intercept factor
ε	[m]	pipe wall roughness
η	[-]	efficiency
$\boldsymbol{\eta}$	[kg/m/s]	dynamic viscosity
θ	[°]	angle (defined locally), angle between surface normal and incident radiation
λ	[W/m/K]	heat conductivity
μ	[-]	mean
ξ	[-]	friction force
ρ	[kg/m³]	density
$\boldsymbol{\rho}$	[-]	reflectance
ρ_{PTC}		tracking angle of the parabolic trough collector
σ	[-]	standard deviation
τ	[-]	transmittance
$\boldsymbol{\tau}$	[-]	start-up state of the PB

1 Introduction

On April 23, 2009, the European Parliament and the European Council released a directive "on the promotion of the use of energy from renewable sources" which states that the European Union's goal is to generate 20% of its energy using renewable energy sources by 2020. This includes energy for electricity, transport, and heating and cooling (European Parliament 2009).

In order to reach that goal, the directive proposes an increase in electricity production from renewables to approximately 34% (European Parliament 2007). Table 1 shows the breakdown of the EU-27's usage of renewable energy sources for electricity (RES-E) production for 2010, which together amounted to 19.42% of the total. Hydro power had the highest share, followed by wind, biomass, and solar power, which is further divided into photovoltaic (PV) at 3.2% and concentrating solar power (CSP) at 0.2%.

A clearer picture of the future development of RES-E may be obtained by examining the following reports:

- "Renewable Energy Projections as Published in the National Renewable Energy Action Plans of the European Member States" (NREAP) by the European Environment Agency (Beurskens 2011)
- "Perspectives on a Sustainable Power System for EUMENA" by the Desertec Industrial Initative (Dii) (Dii GmbH 2012)

The NREAP projects the situation of the EU-27 in the year 2020 based on a road map to reach the 20% goal set by the EU. The Dii report examines a scenario in 2050 in which the EU-27 imports 19% of its total electricity consumption from the Middle East and North Africa (MENA) region. The NREAP report puts the percentage of total electricity production from RES-E at 34.5%, while the Dii report puts it at 92%. Table 1 shows the electricity production figures for 2020 contained in the NREAP report: 495 TWh/y from wind power, 83 TWh/y from PV, and 20 TWh/y from CSP. The Dii report projects electric energy production in the EU-27 and MENA regions in 2050 at 2678 TWh/y from wind power, 412 TWh/y

Table 1: Resource share in renewable energy sources for electricity (RES-E) production for the EU-27 and the Middle East and North Africa (MENA) region for the years 2010, 2020, and 2050

		Hydro	Wind	Biomass	Solar PV	Solar CSP	Other
2010[1] **EU-27**	RES-E production [TWh/y]	343	165	104	20	1	7
	Percentages of RES-E	53.6	25.8	16.2	3.2	0.2	1
	Percentages of total E prod.	10.4	5	3.1	0.6	0.0	0.2
2020[1] **EU-27**	RES-E production [TWh/y]	369	495	232	83	20	18
	Percentages of RES-E	30.4	40.7	19.1	6.9	1.6	1.3
	Percentages of total E prod.	10.5	14.0	6.6	2.4	0.6	0.4
2050[2] **EU-27 +MENA**[a]	RES-E production [TWh/y]	721	2678	309	412	567	52
	Percentages of RES-E	15	57	7	9	12	1
	Percentages of total E prod.	14	52	6	8	11	1

[a] Algeria, Morocco, Tunisia, Egypt, Libya, Jordan, Saudi Arabia, Syria and Turkey
[1](Beurskens 2011, p.263) [2](Dii GmbH 2012, p.107)

from PV, and 567 TWh/y from CSP. Even given the time difference of 30 years between these two forecasts, the differences in electric production from wind and solar power are very high. The Dii report projects an especially high proportion of CSP at 12% of RES-E (Dii GmbH 2012; Beurskens 2011).

If such a high CSP capacity is to be achieved, CSP energy production costs must fall, and new technologies must be developed and tested. A technology normally requires multiple experiments before it is ready for the market and can be used in commercial projects, as the example of solar tower systems with liquid salt as heat transfer fluid (HTF) shows.

Since the early '80s, two small projects, the SSPS in Spain and the MSEE/Cat B in the U.S.A., have been fielded (Reilly 2001). A third research and development program, Thémis, a solar tower system with 2 MW_e output, was run in France near the village of Targassonne from 1983 until 1986 by the French Agency for the Management of Energy (FAME) (Drouot 1984). Using the data and results from Thémis, the U.S Department of Energy maintained a continuing development program called Solar Two. This project, undertaken in cooperation with industry,

ran from June 1996 to April 1999. The solar power tower plant had an output of 10 MW$_e$ (Reilly 2001). Following the validation process for a new receiver design for molten salt power towers at the Plataforma Solar de Almaría (PSA) in Spain from 2006 to 2009, the Solar Two's successor was built. Solar Trés, later called Gemasolar, is the first commercial molten salt power tower with an output of 20 MW$_e$. It supplied energy to the grid for the first time in May 2011. This project was carried out by Torresol Energy in Fuentes de Andalucía, Spain (Burgaleta 2011).

At the moment, a major focus of research and development in solar power stations is the transfer of proven molten salt technology from the tower system to other types of collectors, e.g. parabolic dish, linear Fresnel, and parabolic trough collectors (PTCs). Given the progress in PTC and absorber technology, a solar power station with PTCs and molten salt as HTF seems to have good prospects. This thesis optimises such a power station and outlines its economic potential.

2 State of the art

This chapter offers an overview of current technologies that are available on the present market. It explains a solar thermal power station with PTC and salt as HTF, examines the use of PTCs, receiver tubes, and molten salt as HTF in solar technology, deduces the advantages and disadvantages of using molten salt as HTF in PTC power plants, and provides an overview of current research and development projects.

2.1 Configuration of a solar power plant with parabolic trough collectors and molten salt as heat transfer fluid

Figure 1 shows the schematic configuration of a solar power plant with PTCs and salt as HTF. The PP can be subdivided into four locally separated units: the collector field, the back-up-system, the storage system, and the power block (PB). These systems are connected by two closed loops: the molten salt circuit, indicated by a green line, and the water steam circuit inside the PB.

If enough solar radiation is available, the molten salt from the cold tank is pumped through the collector field, which consists of several loops with PTCs. The molten salt is heated up to the design temperature and stored in the hot tank. The back-up-system, an auxiliary heater connected parallel to the collector field, can also heat the molten salt to the design temperature. If the hot tank is filled to its minimum charging level, the production process can begin upon demand for electricity: the molten salt is pumped through the steam generator (SG) in the PB, exchanges its heat with the water steam circuit, and returns to the cold tank.

The PB is a conventional thermal power station like those used in fossil fuel power stations. It is based on the Rankine cycle with reheat and steam extraction from the turbine. The heat of the HTF is transferred via an SG to the water-steam cycle. The thermal energy of the steam is converted into mechanical energy by the steam turbine and finally to electric energy by the generator.
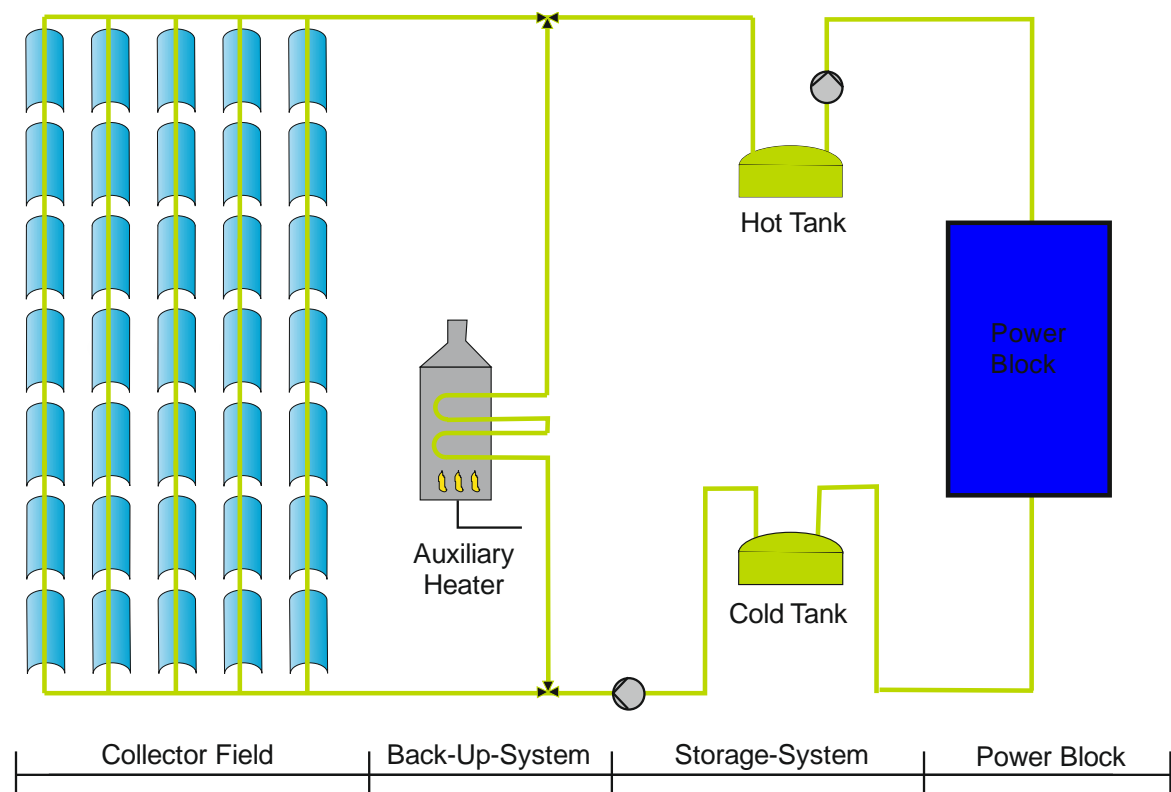
Figure 1: Schematic configuration of a solar power plant with PTCs and molten salt as HTF adapted from (Wittmann 2012)

2.2 Parabolic trough collectors

The collector field of the solar thermal power plant described in Chapter 2.1 consists of several PTCs, as shown in Figure 2. The parabolic reflector (1) concentrates direct normal irradiation onto a linear absorber tube (2) located in the focal line of the mirror. The geometric concentration, the ratio of aperture area (A_{Ape}) to absorber area (A_{Abs}),

$$C_{geo} = \frac{A_{Ape}}{A_{Abs}} \tag{1}$$

of current collectors can be as high as 80. All current commercial mirrors are second-surface silvered glass mirrors with a low fraction of iron oxide (Fe_2O_3), which gives them very high transmittance, as their reflectivity is about 93 to 96 % (Price 2002). Together, several mirrors along the vertical and horizontal axes form one solar collector element (SCE), and several SCEs form one solar collector assembly (SCA) with an aperture width of 4 to 6 m and a length of up to 150 m

1. Reflector
2. Absorber tube
3. Metal construction
4. Pipe installation
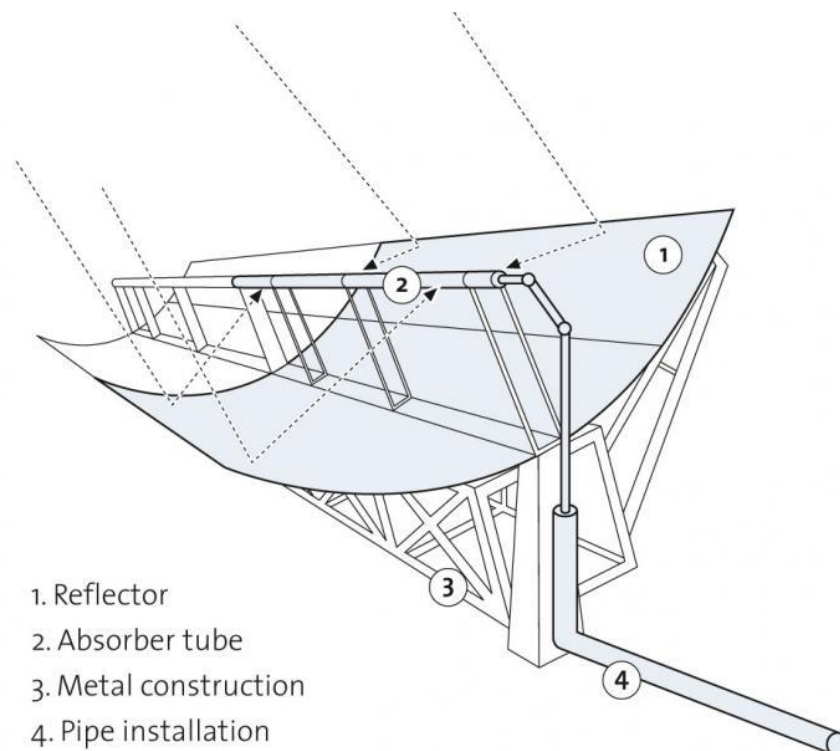
Figure 2: Schematic diagram of a parabolic trough collector (Flagsol 2012)

(Schenk 2012, p. 4). The collector tracks the sun in one dimension throughout the day by means of a hydraulic drive and a local controller. The HTF is pumped through the absorber tube and heated. Several collectors are serially connected into one loop to reach high temperatures.

At the Solar Electric Generation System (SEGS) in the U.S.A., parabolic trough system technology has been operated for more than 25 years, and its collectors have improved constantly (Mohr 1999, p. 47). Drawing on the experience gained during the LUZ LS-2 and LS-3 collector projects, the European consortium EuroTrough built the ET100 and ET150 collectors. Table 2 lists the main characteristic parameters of the ET150, which is made up of 12 SCEs, each comprised of seven mirror panels along the horizontal axis and four in a vertical cross-section. In all, one SCA contains 336 glass facets. At 18.5 kg per m², the steel structure and pylons are 14 % lighter than the LS-3 collector, which means that the solar field (SF) costs are also lower. However, there are fewer structural deformations, which allows better optical performance in gusting wind. One loop can be built with four to six SCAs producing HTF outlet temperatures of over

Table 2: Main characteristic parameters of EuroTrough ET150, HelioTrough, UltimateTrough, and Ronda RHT 2500 collectors

Property	EuroTrough ET150[1]	HelioTrough[2]	UltimateTrough[2]	Ronda RHT 2500[3]
Solar collector element (SCE)				
Absorber diameter	0.07 m	0.09 m	0.09[a] m	0.07 m
Focal length	1.71 m	1.86[a] m	1.95[a] m	1.81 m
Aperture width	5.77 m	6.78 m	7.5 m	5.9 m
Length	12 m	19.1 m	24 m	12 m
Solar collector assembly (SCA)				
Number of SCEs	12	10	10	n/a
Length	148.5 m	191 m	242 m	n/a
Number of glass facets	336	480	480	n/a
Net aperture area	817.5 m²	1263 m²	1689 m²	n/a
Optical parameters				
Mirror reflectivity ($\rho_{Collector}$)	94%	94[a]%	94[a]%	94%

[a] assumption [1](Geyer 2002) [2](Schweitzer 2011) [3](Falchetta 2009b)

500° C. Solar plants equipped with ET150 PTCs can generate up to 200 MW$_e$ (Geyer 2002).

After the testing of the EuroTrough collector in commercial PPs, e.g. Andasol I, II, and III, successive generations of collectors were developed. Table 2 lists their main parameters. The second generation, HelioTrough by Flagsol GmbH, has an aperture width of 6.78 m, a module length of 19.1 m, fewer and longer SCEs, and better optical performance. The third generation, UltimateTrough by Flabeg GmbH, has an aperture width of 7.51 m, and its SCEs are twice as long as the SCEs of the EuroTrough collector. It costs 25 % less than EuroTrough, and its optical performance is 8 % better (Schweitzer 2011).

The Italian National Agency for New Technologies, Energy and the Environment (ENEA) and the Ronda Group designed the RHT 2500 collector especially for the

use of molten salt as HTF. Its geometric parameters are slightly larger than EuroTrough's (5.9 m aperture width, 1.81 m focal length, and 12 m module length).

2.3 Parabolic trough receivers

Figure 3 shows a shortened view of a linear receiver for PTCs. The main feature is the steel absorber tube with a special solar-selective surface. It has good absorption in the solar spectrum range and low heat radiation emission. An anti-reflective evacuated glass tube surrounding the absorber reduces convection heat loss and protects the absorber from oxidation. A getter built inside the tube maintains the vacuum. Because glass and metal expand at different rates, the most sensitive part of the receiver is the glass-to-metal seal (Price 2002). Bellows on the ends of the receiver tube solve this difficulty.

In the Andasol I, II, and III solar thermal power plants and many other commercial projects, the Schott PTR 70 absorber is used, making this parabolic trough receiver (PTR) state-of-the-art. Table 3 lists its technical details. The maximum operating temperature of the steel pipe is 450° C, making it unsuitable for use with molten salt as HTF, which requires temperatures of over 500° C. So far, only the Italian company Archimede Solar Energy (ASE) has developed and tested an
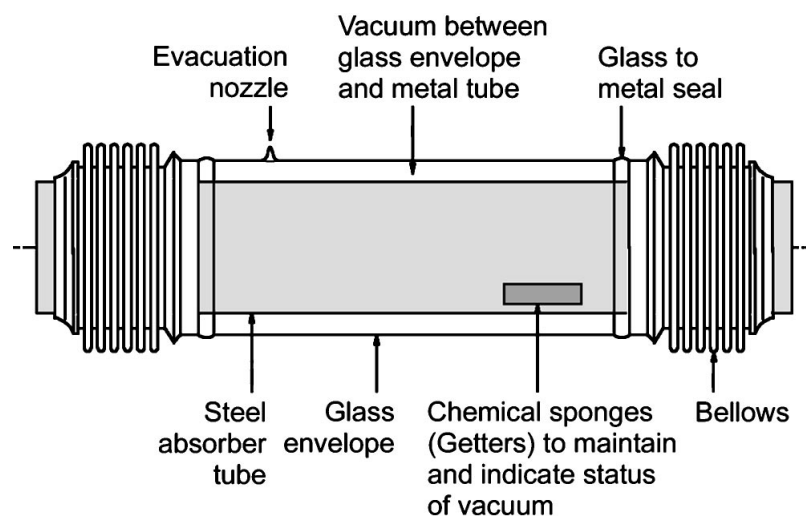
Figure 3: Schematic diagram of a shortened parabolic trough receiver adapted from (Mohr 1999, p. 9)

absorber for this field of application: the Archimede HEMS11. It is the "first commercial salt receiver" (Martini 2010) for HTF at temperatures of up to 550° C. ASE has developed a special coating for the steel receiver in cooperation with ENEA, which enables thermomechanical and thermochemical stability at temperatures of up to 600° C

A comparison of Schott PTR 70 and Archimedes HEMS11, found in Table 3, reveals that their geometry is nearly identical. Only thickness differs: at 3 mm, the Archimede absorber is 1 mm thicker than the PTR 70, but its maximum operating pressure is 20 bars lower. This probably results from the higher operating temperatures of the steel pipe. The HEMS11's optical parameters (solar absorbance, thermal emittance, and transmittance of solar radiation) are inferior to

Table 3: Comparison of the main parameters of Archimede HEMS11, Schott PTR 70, and PTR 80 parabolic trough receivers

Property	Schott		Archimede
	PTR 70[1]	PTR 90[2]	HEMS11[3]
Geometric parameters			
Length	4060 mm	4600–4800 mm	4060 mm
Outer diameter	70 mm	90 mm	70 mm
Inner diameter	66 mm	n/a	64 mm
Optical parameters			
Solar absorbance ($\alpha_{absorber}$)	95.5%	96.1%	95%
Thermal emittance at 400° C	9.5%	8.8%	10%
Transmittance of glass tube ($\tau_{absorber}$)	96.5%	96.5[a]%	96%
Active aperture area ($\eta_{bellows}$)	96.7%	97-97.2[a]%	95.8[a]%
Maximum operating parameters of the steel pipe			
Temperature	450° C	590° C	550° C
Pressure	40 bar	n/a	20 bar
Vacuum enclose pressure over lifetime	$<10^{-3}$ mbar	$<10^{-3}$ mbar	$<10^{-4}$ mbar

[a] assumption [1](Schott Solar CSP GmbH 2011) [2](Kuckelkorn 2009) [3](Archimede Solar Energy 2011)

the PTR 70's, making its overall optical performance lower. This indicates that the Schott absorber's coating is slightly better. The PTR 70's conductive heat losses are marginally higher because its maximum vacuum enclose pressure over lifetime is one order of magnitude higher.

To penetrate the next generation of the PTC solar power plant market, Schott Solar is currently developing two new receiver designs, the PTR 80 and PTR 90. Table 3 lists the parameters of the PTR 90 absorber. To compete with the Archimede HEMS11 and employ molten salt as HTF, Schott developed a new absorber coating which allows maximum operating temperatures of 590° C. The company also improved optical parameters, reduced heat losses by 20-30%, and increased receiver length and diameter for use in the next generation of PTC, e.g. the HelioTrough or UlimateTrough. The longer PTR increases the ratio of area of bellows to active aperture area ($\eta_{bellows}$), and the larger diameter increases the fraction of the reflected sun rays incident upon the aperture that reach the PTR, known as intercept factor (γ_{θ}). These changes raise the optical efficiency

$$\eta_0 = \boldsymbol{\rho}_{Collector}\boldsymbol{\alpha}_{absorber}\tau_{absorber}\gamma_{\theta}\,\eta_{bellows} \tag{2}$$

of the next PTC generation to 82%, 8% higher than the current design (Kuckelkorn 2009). The parameters of Eq. (2) are listed in Table 2 and Table 3.

2.4 Heat transfer fluids in solar power stations with parabolic trough collectors

Table 4 lists commercially available HTFs for CSP power plants. The state-of-the-art HTF for PTC power plants is a eutectic mixture of two very stable compounds, biphenyl ($C_{12}H_{10}$) and diphenyl oxide ($C_{12}H_{10}O$). This organic substance is sold by Solutia Inc. under the brand name Therminol VP-1 (Solutia Inc 2012) and by Dow Chemical Company under the brand name Dowtherm A (Dow Chemical Company 2001).

Therminol VP-1 is used for the SEGS in the U.S.A. Its advantages are its low freezing point (12° C) and low corrosion potential. But it also has several disadvantages. It limits the SF's maximum operating temperature to 400° C due to thermal degradation. Therminol VP-1 cannot be used as a thermal energy storage

Table 4: Characteristics of nitrate/nitrite salts and Therminol VP-1

Property		Solar Salt	Hitec	Hitec XL	Therminol VP-1
Composition (weight percentage)					
Salt[1]	$NaNO_3$	60%	7%	15%	
	KNO_3	40%	53%	43%	
	$NaNO_2$		40%		
	$Ca(NO_3)_2$			42%	
Organic	$C_{12}H_{10}$				73.5%
Compound [2]	$C_{12}H_{10}O$				26.5%
Operating temperatures					
Liquidus temperature [° C]		227[3]	141[5]	140[5]	12[2,4]
Upper temperature [° C]		593[4]-600[1]	454[5]–538[4]	460[5]-500[4,1]	400[2,4]
Chemical properties at 400° C[6]					
Viscosity (η) [mPas]		1.773	1.710	n/a	0.149
Heat conductivity (λ) [W/m/K]		0.511	0.330	n/a	0.076
Heat capacity (c) [J/kg/K]		1516	1562	1304	2635
Density (ρ) [kg/m³]		1834	1790	1903	694
Volumetric heat capacity (s) [kJ/m³/K]		2780	2796	2482	1829
Economical parameters[7]					
Nominal cost [$/kg]		0.49	0.93	1.19	2.2

[1](Kelly 2007) [2](Solutia Inc 2012) [3](Kramer 1980) [4](Raade 2011b) [5](Bradshaw 1990) [6](Steag 2012) [7](Kearney 2003)

medium due to its high vapour pressure (approximately 10 bar at 390° C), so an indirect storage system, using thermal energy transfer to a second HTF, is needed (Raade 2011b). This synthetic oil necessitates strict statutory requirements to protect the local environment because it is toxic and at over 621° C can spontaneously combust (Solutia Inc. 2012). The commercially available organic HTFs are also expensive (Mohr 1999, p. 74).

A more promising HTF seems to be nitrate (NO_3) and nitrite (NO_2) salt mixtures. These are used as HTF, as well as fluid for the storage tank, in the Gemasolar commercial project (Burgaleta 2011) and in the Archimedes research project (Falchetta 2010), which Chapter 2.6.1.2 describes in detail.

If a salt mixture is heated to its liquidus temperature, its cations and anions are generally completely dissociated. Molten salts have high thermal stability, density, and heat capacity, good thermal and electric conductivity, relatively low viscosity, and a low vapour pressure, even at elevated temperatures (Baudis 2001, p. 5f). Many varieties are available in large commercial quantities from several suppliers (Raade 2011b). Table 4 shows the properties of three commercially available salt mixtures sold by Solutia Incorporated: Solar Salt, Hitec, and Hitec XL. Solar salt is a nearly eutectic binary mixture of potassium nitrate (KNO_3) and sodium nitrate ($NaNO_3$), as shown in Figure 4. Hitec and Hitec XL are both eutectic ternary mixtures of sodium nitrate, potassium nitrate, and sodium nitrite ($NaNO_2$) (Hitec) or calcium nitrate ($Ca(NO_3)_2$) (Hitec XL).

As Table 4 shows, a range of upper temperature limits for nitrate and nitrite salts is given. At high temperatures, these salts undergo thermal decomposition, and the insoluble products can plug pipes and valves, foul heat transfer surfaces, and aggravate corrosion. Common impurities, such as water vapour or carbon
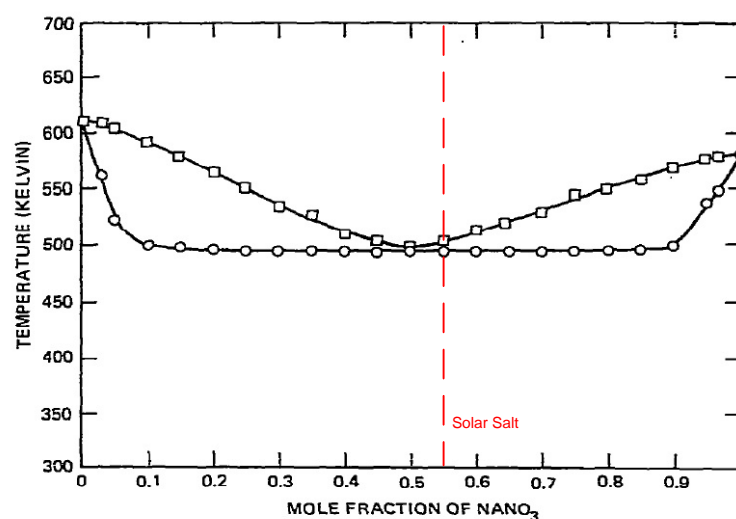
Fig. 3. Experimental DSC data for NaNO₃—KNO₃.

Figure 4: Phase diagram of NaNO3-KNO3 (Kramer 1980)

dioxides, affect the decomposition process. The upper temperature limit may also be qualified when decomposition products are present or "a significant concentration of decomposition products is reached" (Bradshaw 1990). All these factors explain the variety of upper temperature limits for nitrate and nitrite salts found in the literature.

Solar salt is the most stable salt in terms of thermal composition, usable at temperatures of up to 600° C under atmospheric conditions. It is also the cheapest salt. But its liquidus temperature (227° C) is very high. Hitec can be used at up to 454° C under atmospheric conditions, the temperature at which thermal decomposition starts, nitrite converts to nitrate, and Hitec's freezing point rises from 141° C. If nitrogen gas is blanked to the salt, thermal decomposition begins at 538° C (Kearney 2003). Hitec XL can be used at up to 500° C under atmospheric conditions.

New molten salts with a lower freezing temperature are currently under development. Table 5 shows four non-commercial examples of recently developed molten salt mixtures. Due to on-going testing, the chemical properties of these salt mixtures are rarely available in literature. Despite their expanded temperature range, the newly developed molten salts seem to have several problems, and much remains unknown. The cost of the advanced HTF is higher than that of solar salt. No chemical properties have been published so far (Raade 2011b). For low-melting HTF, no long-term thermal stability analyses have been conducted. The chlorides in the molten salt also tend to corrode steel alloys. Closer analyses are pending (Raade 2011a). The TNS-4 has a density of 1,850 kg/m³ and a dynamic viscosity of 1.8 mPas at 400° C. These parameters are comparable to those of solar salt. But the more critical parameter, specific heat capacity, has not yet been published (Ren 2011). Sodium has also been proposed as an HTF. Its density is 919 kg/m³, its specific heat capacity 1372 J/kg/K, its thermal conductivity 87 W/m/K, and its dynamic viscosity 0.008 mPas at 400° C. In addition to its greater temperature range, sodium's low viscosity reduces pumping parasitics and its very high thermal conductivity reduces the risk of hot spots. Its disadvantages are its low volumetric heat capacity and its cost, which is 200% of Hitec's. The main problem with using sodium is that it is toxic and very flammable

Table 5: Characteristics of newly developed molten salts

Property		Advanced HTF[1]	Low-melting HTF[2]	TNS-4[3]	Liquid Sodium[4]
Composition (weight percentage)					
Nitrate	$NaNO_3$	6%		?%	
	KNO_3	23%	1%	?%	
	$Ca(NO_3)_2$	19%			
	$CsNO_3$	44%			
	$LiNO_3$	8%	21%	?%	
Nitrite	KNO_2		45%		
	$Ca(NO_2)_2$		19%		
	$NaNO_2$		12%		
Other	KCL		2%		
	Na				100%
	Additive			?%	
Operating temperatures					
Liquidus temperature [° C]		65° C	53° C	83° C	97.9° C
Upper temperature [° C]		561° C	481° C	618° C	873° C

[1](Raade 2011b) [2](Raade 2011a) [3](Ren 2011) [4](Boerema 2012)

(Boerema 2012). The first solar tower project to use molten salt as HTF, the SSPS, begun in 1981, used sodium. Its test facility was completely destroyed in a sodium fire in 1986 (Reilly 2001). Sodium necessitates increased safety precautions, which normally involve higher investment and operation cost.

2.5 Advantages and disadvantages of using molten salt as heat transfer fluid in parabolic trough solar power plants

There are several advantages to using molten salt instead of organic compounds as HTF in PTC solar power plants. As explained in Chapter 2.4, the thermal stability of molten salts allows higher temperatures – up to 600° C, even at atmospheric pressure – at the outlet of the SF. This results in higher temperatures of live and reheat steam in the water-steam cycle, which improves the efficiency of the Rankine cycle.

Molten salt HTF can also reduce the cost of thermal storage. Because of its low price and good thermodynamic parameters, salt is widely used as a storage medium. Its volumetric heat capacity is reasonable, and its vapour pressure is very low, allowing storage under atmospheric pressure and eliminating the cost of thick walls for the storage tank. It allows a direct storage system, unlike Therminol VP-1, and so requires no additional heat exchangers, lowering investment costs and increasing storage system efficiency because the system produces less entropy. The temperature difference between the cold and the hot tanks – about 100° C in the current Andasol I solar power plant, for example (Relloso 2009) – is up to 300° C with molten salt HTF. This and its higher volumetric heat capacity increase the ratio of thermal storage capacity to storage tank volume.

Unlike Therminol VP-1, nitrate and nitrite salts are not toxic and have a high autoignition temperature. Leakage will not harm the local environment, and the danger of a fire is negligible (Benmarraze 2010).

The viscosity of the molten salt is twelve times that of Therminol VP-1. Pumping the fluid through the piping elements would therefore normally require more power, and SF parasitics would be higher. But "the mass flow in the solar field is considerable [!] lower with molten salt, which leads to a lower pressure loss in the piping. Both effects combined – low mass flow and low pressure loss – lead to relatively low pumping parasitics compared to a (Therminol, editor's note) VP-1 solar field" (Kearney 2002). Eq. (3) explains this effect. Given a constant heat flow due to solar radiation to one PTC loop ($\dot{Q}_{loop}$), constant area of PTR (A_{PTR}), and a

constant HTF temperature rise through a PTC loop (ΔT_{loop}), the only variable parameter is the velocity of the HTF (v_{HTF}) in the PTR.

$$\dot{Q}_{loop} = \dot{m}\bar{c}\Delta T_{loop} = A_{PTR}v_{HTF}s\Delta T_{loop} \tag{3}$$

Because the volumetric heat capacity (s) of the molten salt is higher than that of Therminol VP-1, the velocity is lower. Another reason is the higher ΔT_{loop} when using molten salt as HTF. These factors are more significant than the lower viscosity.

Another advantage is flexible power plant management. Because molten salt is used with a direct storage system, the SF and SG circuits are completely decoupled. During periods of high radiation, thermal power is stored in the hot tank. Upon demand for electric production, the hot molten salt supplies the SG with thermal power and the plant produces electricity as long as the hot tank level is high enough. Low storage system investment costs make a high storage capacity economically viable, and a molten-salt-based solar power plant can produce electricity even at night. 24-hour electricity production is possible, as demonstrated at the Gemasolar power plant in May 2011 (Burgaleta 2011). Power plant efficiency is also increased during the night because the ambient temperature is lower. These effects make projectable electricity production possible and increase the stability of electric power transmission. This is one of CSP's main advantages over other renewable energies such as photovoltaic or wind energy.

Unfortunately, molten salt also has disadvantages. Table 4 shows the high freezing point of nitrate and nitrite salts. The state-of-the-art nitrate salt, solar salt, has a very high freezing point at 227° C, which necessitates energy-intensive freeze protection to avoid blockage of pipes and valves. This involves the installation of additional hardware, e.g. impedance heating elements, heat tracing, or insulation, which in turn entails high investment and operation costs (Kearney 2004).

Higher process temperatures also raise the average temperature of the SF, causing higher radiation heat losses and lowering efficiency. Higher process parameters also lead to pipe, valve, and pump corrosion. Common carbon steel's

corrosion rate is about 0.12 mm/y at process temperatures of up to 460° C. At higher temperatures, nickel-based alloys show a good corrosion rate – less than 1mm per century at temperatures of up to 600° C. But they are also more expensive than carbon steels (Bradshaw 1987).

2.6 Current projects

Presently, no commercial PTC power plant with molten salt as HTF is in operation. However, two research and development programs run by ENEA and the German Aerospace Center (DLR) are currently working with molten salt.

2.6.1 ENEA research and development activities

In 2001, ENEA released a strategy paper (ENEA 2007) that focuses, among other things, on high-temperature (550° C) heat production and storage. At this temperature, a linear trough collector with molten salt as HTF is considered the best solution. According to the paper, the following are to be achieved:

- "A strong R&D programme in the few elements of parabolic trough" (ENEA 2007, p. 83)
- "The realisation of a (…) demonstration power plant with parabolic troughs (…) for a market niche in the 5 – 10 MW$_e$ production" (ENEA 2007, p. 83)

During the course of the research and development program, a PTC, the RHT 2500 collector, and a parabolic trough receiver (PTR), the Archimede HEMS08, were invented. These collectors are discussed in Chapters 2.2 and 2.3.

2.6.1.1 Prova Collettori Solari

In 2004, the Prova Collettori Solari (PCS), a 100m PTC test circuit with solar salt as HTF, began operation at ENEA Cassia Labs. Its goal was to test the PTC, PTR, collector interconnectors, pumps, and heating system which had been developed especially for molten salt usage. The test involved 1700 hours of operation and about 160 SF filling and draining cycles, during which no critical situations arose or accidents occurred. The draining and filling of the SF is the critical phase due to

thermal losses and low salt mass flow – constant circulation of the salt can prevent freezing even if temperature nears solidification. If the molten salt freezes, it contracts, reducing its volume and causing no mechanical stress for piping (Gaggioli 2007).

2.6.1.2 Archimede solar thermal power plant

After the successful PCS research and development period, ENEA and the Italian electric utility company Ente nazionale per l'energia elettrica (ENEL) built the Archimedes solar thermal power plant (5 MW$_e$ output) at Priolo Gargallo. According to an ENEL press release (ENEL 2010), the Archimede Power Plant was put into operation on July 14, 2010, and "is the first in the world (with PTC, editor's note), to use molten salts as the heat transfer fluid" (ENEL 2010). "Due to the little size of the solar plant and the prototypal characteristics of its components, the demonstration in [!] not fully representative with respect to economic viability of the concept, but it is anyway a fundamental test of the technical aspects as functionality, efficiency and reliability" (Crescenzi 2011).

Figure 5 shows a schematic of the power plant, and Table 6 lists Archimede's main design parameters. The SF consists of nine collector loops, each equipped with six 100-meter-long PTCs. The solar salt is stored in a cold tank at 290° C and in a hot tank at 550° C.

For the SF, there are three possible operating states (Falchetta 2009a):

- Production: the HTF is pumped from the cold tank through the SF, heated to 550° C, and finally stored in the hot tank. The PTCs track the sun.
- Re-circulation: the solar salt is pumped from the cold tank through SF and the recirculation loop back to the cold tank. The PTCs track the sun. This operating state occurs when there is insufficient solar radiation or during a transient state, e.g. start-up in the morning or shut-down in the evening.
- Night circulation: like re-circulation, but the collectors are in parked position, oriented towards the ground.

Table 6: Design data of the Archimede Power Plant (Falchetta 2010)

Solar field circuit	
Number of collectors	54
Number of collector loops	9
Total collector surface	30580 m²
Annual direct normal irradiation	1936 kWh/m²/y
Storage size	80 MW$_{th}$
Steam generator circuit	
Steam generator capacity	12 MW$_{th}$
Temperature of live steam	540° C
Pressure of live steam	102 bar
Additional electric capacity	4.96 MW$_e$
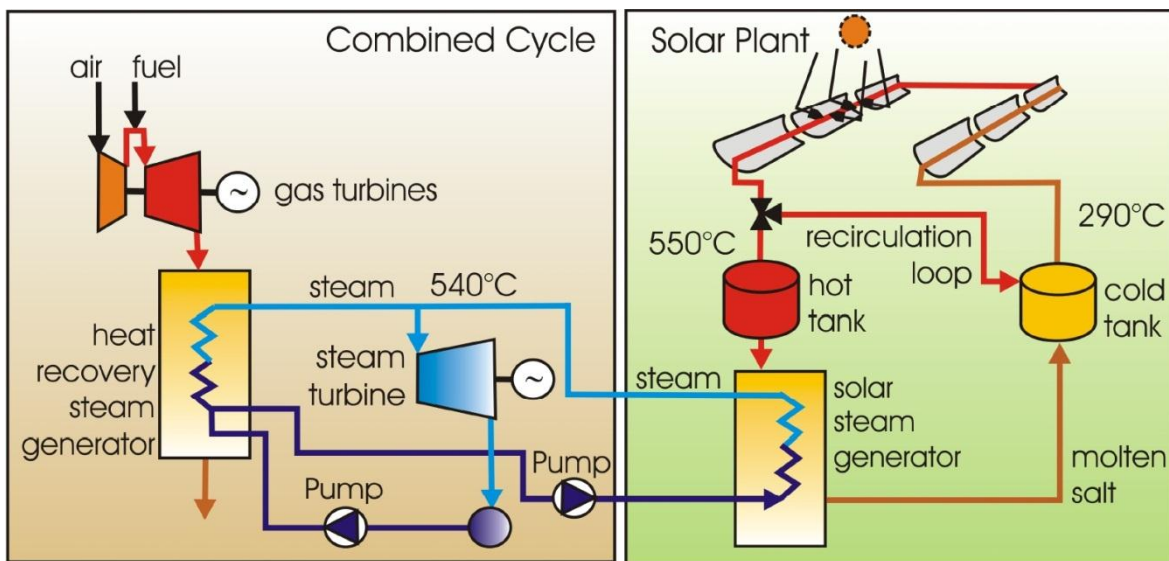
Figure 5: Schematic of the Archimede solar power plant with PTC and molten salt as HTF (Falchetta 2010)

At nighttime, solar salt should be kept above 270° C to prevent solidification of the salt. To this end, additional electric heating elements are fitted to the pipes and the two tanks. For the SG circuit, there are five possible operating states (Falchetta 2009a):

- Normal steam production

- Steam production and heat restore to the cold tank

- No steam production (standby)

- No steam production and heat restore to the cold tank

- Start-up

The SG is composed of three vertical heat exchangers: economizer, evaporator, and superheater. It uses a steam drum with natural circulation. Live steam with a pressure of 102 bar and a temperature of 540° C is produced and fed into the high-pressure stages of the combined-cycle power plant steam turbine (Falchetta 2009b).

Because two tanks are used, the SF circuit and SG circuit are completely decoupled, allowing production of live steam when the SF is not in operation. The hot tank capacity is sufficient for up to 6.6 hours.

2.6.2 DLR research and development activities

In a press release dated February 24, 2011 (Deutsches Zentrum für Luft- und Raumfahrt 2011), the DLR announced that it would build a research and development solar thermal power plant with PTCs and molten salt as HTF near Evora, Portugal. This plan is supported by Bundesministerium für Umwelt, Naturschutz und Reaktorsicherheit (BMU) within the framework of the High Performance Solarthermie (HPS) joint research project. DLR's project partners are Siemens AG, K+S AG and Senior Flexonics GmbH. The project's goal is to reach temperatures above 500° C with molten salt. To achieve this, the partners are using the Siemens SunField 6 PTC, and the Archimede HEMS11 PTR by ASE. The thermal energy of the molten salt is transferred in a newly developed once-through boiler to the water-steam circuit. The project will also demonstrate the economic feasibility and general plant safety of such technology. Solar salt is to be used as HTF. During the joint research project, other salts with lower freezing points are also to be investigated and their potentials identified (Deutsches Zentrum für Luft- und Raumfahrt 2011; Siemens AG 2011).

3   Modelling of the solar thermal power plant

The model of the solar thermal power plant with PTCs and molten salt as HTF is created with the commercial simulation software EBSILON®Professional 10.01.01, referred to as Ebsilon in this thesis, by Steag Energy Services GmbH. Ebsilon is an abbreviation for "energy balance and simulation of the load response of power generating or process controlling network structures". It is a Windows-based modelling tool with a graphical user interface that allows the drag-and-drop arrangement of multiple pre-built components connected by material and logic lines to simulate thermodynamic cycles.

The add-on EbsSolar, developed in cooperation with the DLR, offers components, e.g line focusing collectors, thermal storages, headers, and distributers, to simulate a solar thermal power plant. Besides the steady-state simulation both at the design point and under off-design conditions, a successful model of an SF requires transient simulation due the very dynamic environmental factors involved in solar power plant operation. For this purpose, a time series calculation module, an Excel-like spread-sheet, imports dynamic process variables, e.g. ambient temperature and direct normal radiation, into the simulation model for different time instants. Most components perform a steady simulation for each time instant. Performing several consecutive steady simulations with the time series module results in a quasi-instationary simulation. But there are also two fully transient components: direct and indirect storage. The indirect storage is a simple pipe model that calculates transient heat exchanges between the pipe and the fluid flowing through it. The direct storage is a model of a transient storage tank that can be charged or discharged between two time instants. It shows heat exchange with the environment — cooling down or heating up. To track these two components and the entire power plant over a series time instants, a Pascal-based scripting language, EbsScript, is used.

EbsSolar and EbsScript allow the realistic simulation of the behavior of a solar thermal power plant. The resulting simulation model is simple, fast, and numerically robust enough to calculate annual yield based on transient system

behavior. Appendix A contains a model of the solar field using PTCs and salt as HTF, while Appendix B contains a model of the power block. The model creates an interface for parameter input using the macro interface "Intelligence of power plant", shown as a blue box on the upper left border of the screenshot in Appendix A. The interface allows several solar thermal power plant parameters (listed in Appendix C) to be specified, generating an individual simulation model. After parameter input, executing the EbsScript "Design power plant" results in the design of specific parts of the power plant according to the input parameters. Appendix F contains a schematic flow-chart of this script. The power plant design process resulting parameters are listed in the lower rows of the table in Appendix C. Following the solar thermal power plant design process, the time series dialog shown in Appendix D allows annual yield calculations. The simulation is performed by importing the ambient temperature and the direct normal radiation for each time instant, represented by a row in the spreadsheet, into the simulation model and entering the resulting parameters, listed in the table of Appendix E, into the spreadsheet.

The following chapter describes in detail the simulation model of the solar field and the power block. It examines the modelling of its components and the transient system behavior more closely, and describes the model's plant operation management strategy based on the EbsScript schematically shown in Appendix G, and the economic and statistical model to calculate the levelized electric cost (LEC) in detail.

3.1 Solar field

The model of the solar field consists of the sun, the parabolic trough collectors described in Chapter 2.2, distributing and collecting headers, feeders, two salt submersion pumps, an auxiliary heater, and a cold and a hot storage tank. Figure 6 contains a schematic drawing of the Ebsilon model.
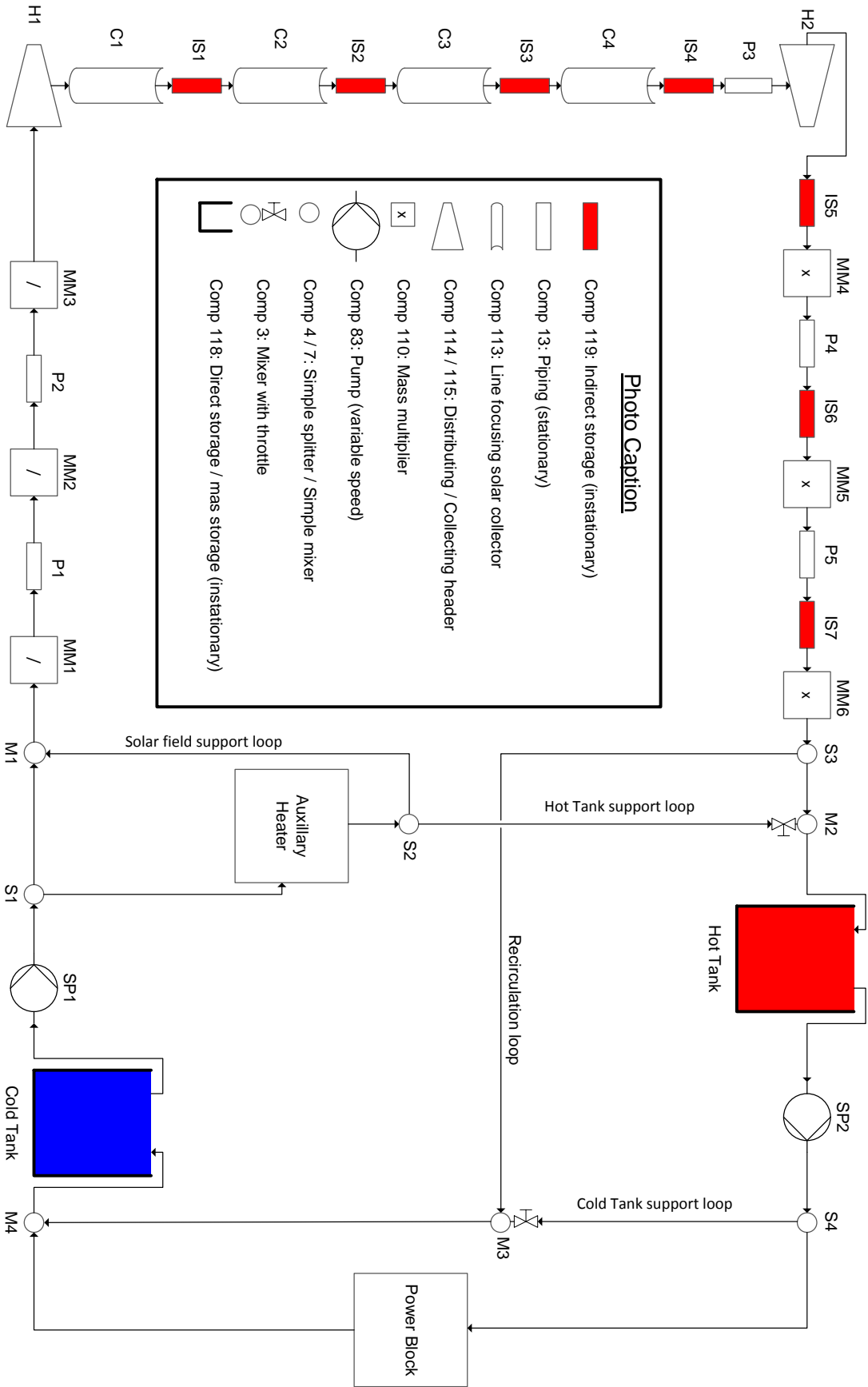
Figure 6: Model of the solar field with Ebsilon

Photo Caption

Comp 119: Indirect storage (instationary)

Comp 13: Piping (stationary)

Comp 114 / 115: Distributing / Collecting header

Comp 113: Line focusing solar collector

Comp 110: Mass multiplier

Comp 83: Pump (variable speed)

Comp 4 / 7: Simple splitter / Simple mixer

Comp 3: Mixer with throttle

Comp 118: Direct storage / mas storage (instationary)

The solar heat input into the HTF is simulated with components C1, C2, C3, and C4, representing a loop of PTCs. This heat input depends on the boundary conditions of normal solar irradiation, the location, and the current date and time. The mass flow through the PTCs is controlled so that the HTF reaches the hot tank's design temperature at the outlet of the SF. Heat losses of piping elements and the PTRs implemented into the simulation realistically model the HTF's nighttime cool-down behavior. The pressure losses in these components are used to simulate the parasitics of the two submersion pumps. This allows an estimation of the pump electricity consumption for the annual yield calculation. The thermal inertia of the entire SF is approximated by entering the steel mass of all PTRs, collecting headers, and feeders into the simulation model.

In the Ebsilon model, the SF or the hot tank can be maintained with HTF at the hot tank design temperature by activating the model of the AH and pumping the HTF through the corresponding loops (the hot tank or solar field support loop). During nighttime operations, the HTF from the SF is pumped through the recirculation loop to the cold tank. As stated in Chapter 2.6.1.2, this recirculation of the HTF is necessary to prevent solidification. If the cold tank reaches its critical temperature during nighttime cool-down, HTF from the hot tank is pumped through the cold tank support loop to prevent the HTF in the SF from reaching its critical temperature.

3.1.1 Heat transfer fluid

Ebsilon models HTF properties (j) (specific heat capacity (c), density (ρ), heat conductivity (λ), viscosity ($\boldsymbol{\eta}$), and entropy ($\boldsymbol{s}$)) using a fourth-order polynomial. The reference temperature is 0° C.

$$j = a_{j,0} + a_{j,1}T + a_{j,2}T^2 + a_{j,3}T^3 + a_{j,4}T^4, \quad j = c, \rho, \lambda, \boldsymbol{\eta}, \boldsymbol{s} \tag{4}$$

Solar salt, introduced in Chapter 2.4, within a temperature range of 230° C to 600° C is selected as HTF. The coefficients of the fourth-order polynomial (a) are adopted from the pre-set in Ebsilon.

3.1.2 The sun

In the Ebsilon simulation model, the sun is represented by component 117, which is not shown in Figure 6. The DIN-5034 algorithm (Frommhold 2008) is used to calculate sun height angle (γ_s) and sun azimuth angle (α_s), both shown in Figure 7, using the inputs of local time, latitude, and longitude. Assuming that the PTC is not built on a slope and the collector axis is oriented north-south (α_{PTC}=0), the tracking angle of the PTC (ρ_{PTC})

$$\tan \rho_{PTC} = \frac{\sin \alpha_s}{\tan \gamma_s} \tag{5}$$

can be calculated from the sun azimuth and height angle, as can the incident angle (θ_i), the angle between the aperture normal and the incident sun beam.

$$\theta_i = \sqrt{1 - \cos {\alpha_s}^2 \sin {\gamma_s}^2} \tag{6}$$
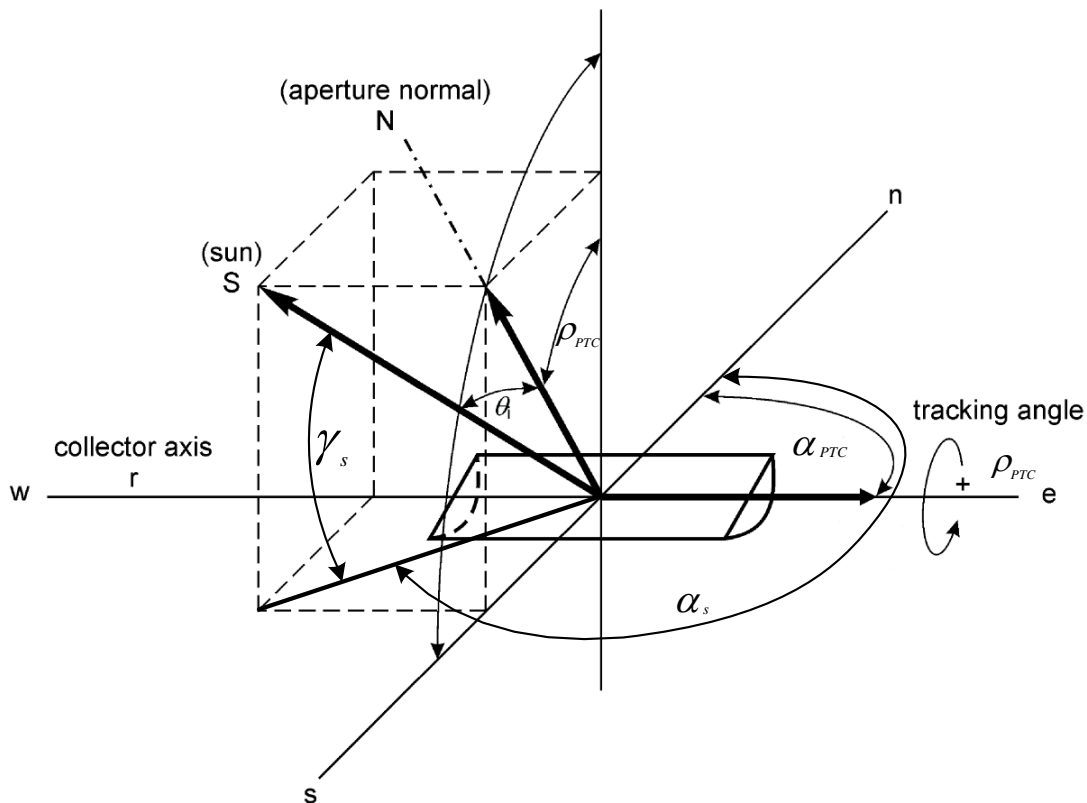
Figure 7: The angles of a parabolic trough collector and of the sun adopted from (Schenk 2012, p. 21)

3.1.3 Solar field layout

In an SF, the HTF from the cold tank is pumped through the feeders to the distributing header, where the mass flow is split into several collector loops. After passing the PTCs, the HTF is collected in the collecting header and returned to the balance of plant (BOP) and the hot tank through the feeder pipelines. The headers and feeders can be arranged in different layouts. Today's solar thermal power plants with outputs of up to 50 MW_e have an I layout or H layout. For example, the PTCs of Andasol I, II, and III are arranged in an I layout around the BOP. A schematic of one quarter of the I layout and H layout is shown on the right side of Figure 8. The next generation of power plants, with outputs of up to 250 MW_e, have many more PTCs and therefore require more area. Other layouts have been proposed for this class of power plant, such as the 3/2 H layout and the 2 H layout (Meyer 2010). A schematic of one quarter of these two layouts is shown on the left side of the Figure 8.

The choice of solar thermal power plant layout depends on a design process weighing the heat losses in the piping elements against pressure losses. The optimized layout for a solar thermal power plant depends on the number of its PTCs. The I layout is the best for a low number of PTCs because it requires no feeders, which means that the piping element area and, in turn, heat loss is reduced.
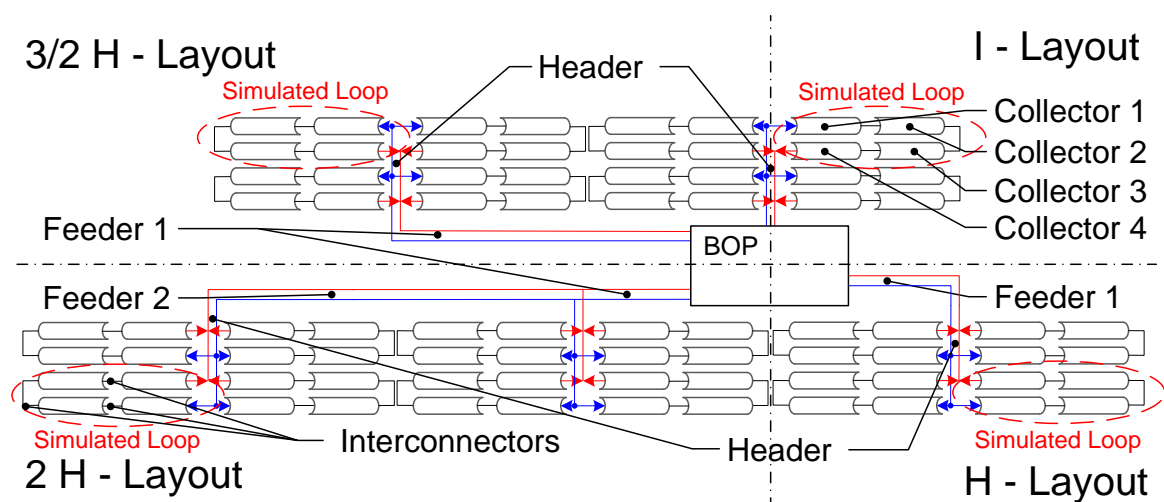
Figure 8: Schematic of one quarter of the I layout, H layout, 3/2 H layout and 2 H layout with labelled characteristic components

For a larger number of collectors, the length of the distributing header and feeder is greater, which results in a rectangular SF design. To minimise pressure losses, the length and width of the SF should be nearly the same to minimise the maximum distance the HTF is pumped through the piping elements. Other layouts, such as the H layout, 2/3 H layout, or 2 H layout should therefore be considered. These layouts need feeders to feed the distributing and collecting headers, so the thermal losses are higher than those in an I layout, but the pressure losses are lower.

To investigate the described effect and simulate both a state-of-the-art power plant and a next-generation power plant, all four layouts are entered into the Ebsilon model. It is therefore necessary to model all individual layout components shown in Figure 8. The simulation models only one representative PTC loop for each layout, marked with a red dashed ellipse in Figure 8. The real components and their corresponding Ebsilon simulation components are listed in Table 7.

Table 7: The real components of a solar field and the modelled components in Ebsilon

Modelling of the piping and collector of the solar field			
Real component		**Model**	
		Component	**Transient**
Piping cold	Feeder 1	P1	no
	Feeder 2	P2	no
	Header	H1	no
Collectors	Collector 1	C1, IS1	yes
	Collector 2	C2, IS2	yes
	Collector 3	C3, IS3	yes
	Collector 4	C4, IS4	yes
	Interconnectors	P3	no
Piping hot	Header	H2, IS5	yes
	Feeder 2	P4, IS6	yes
	Feeder 1	P5, IS7	yes

To approximate the thermal loss and pressure drop of the piping elements within the different layouts, a simple model is run in Ebsilon. To simulate the representative loop, mass multipliers (MM) are introduced into the simulation model. The MM component divides or multiplies the mass flow of the HTF in the pipe with a specific factor, listed for the four SF layouts in Table 8. Because not all components are used in each layout, each modelled component may or may not be activated, as shown in Table 8.

Another variable simulation parameter is the number of collectors in one loop. Current state-of-the-art solar thermal power plants with Dowtherm A or Therminol VP-1 have four collectors in one loop. Other configurations probably offer better results when salt is used as HTF because of its different thermal properties, e.g. volumetric heat capacity (Metzger 2010, p. 21).

If PTR wall thickness is neglected, the heat input into the HTF over one loop ($\dot{Q}_{loop}$) with the length (l_{PTR}) can be calculated using the local inner heat transfer coefficient ($\alpha_i(z)$), local PTR temperature ($T_{PTR}(z)$), and local HTF temperature ($T_{HTF}(z)$).

$$\dot{Q}_{loop} = \int_0^{l_{PTR}} \alpha_i(z)\big(T_{PTR}(z) - T_{HTF}(z)\big)\, dz \cdot \big(\pi d_{i,PTR}\big) \tag{7}$$

If the number of collectors in a given loop increases, its length and therefore the thermal energy absorbed by the HTF, increases. If HTF temperature rise is constant over a PTC loop (ΔT_{loop}) in Eq. (3), its velocity in the PTR rises with PTR length. Because the pressure losses are proportional to the velocity and the length of the PTR

Table 8: Modelling of different solar field layouts

Components	I layout	H layout	3/2 H layout	2 H layout
MM1 and MM6	1	2	3	2
MM2 and MM5	1	1	1	2
MM3 and MM4	2	2	2	2
P2, P4 and IS6	not active	not active	not active	active
P1, P5 and IS7	not active	active	active	active

$$\Delta p = f(Re)\frac{l_{PTR}}{d_{i,PTR}} \cdot \frac{\rho * v^2}{2} \tag{8}$$

the pumping parasitics increase as well. The heat transfer coefficient

$$\alpha_i(z) = f(Pr, Re) \tag{9}$$

is proportional to the Prandtl and Reynolds number and therefore to the velocity in the PTR. A higher heat transfer coefficient means a higher heat input into the HTF. Thus the ideal number of collectors can be determined by weighing PTR heat input against PTR pressure losses.

As shown in Figure 6, the Ebsilon simulation models only four collector components (C1, C2, C3, and C4). To simulate a different number of PTCs in one loop (n_{PTC}), the following simple equation is entered into the model to calculate the length of each PTC component ($L_{PTR,j}$).

$$l_{PTC,j} = \frac{n_{PTC}}{4}l_{PTC,real}, \qquad j = C1, C2, C3, C4, \qquad n \, \epsilon \, \{2; 4; 6; 8; ...\} \tag{10}$$

3.1.4 Parabolic trough collector

The simulation models three different PTCs, which can be selected in the user interface:

- EuroTrough with Schott PTR 70 (next generation)
- HelioTrough with Schott PTR 90
- UltimateTrough with Schott PTR 90

The next-generation Schott PTR 70 receiver simulated in the model is a combination of the Archimedes HEMS11 and the Schott PTR 90 receiver, both described in Chapter 2.3. The geometric parameters of the HEMS11 PTR have been combined with the slightly better optical parameters of the Schott PTR 90, resulting in a next-generation PTR for use with molten salt as HTF. The parameters of the three PTCs used in the Ebsilon model are listed in Appendix H. Because HelioTrough and UltimateTrough are currently under development, some parameters are undocumented and must be assumed for the PTC models. These assumptions are listed in Appendix H.

The heat absorbed by the collector ($\dot{Q}_{PTC}$) is calculated using the direct normal irradiance (DNI), PTC net aperture area (A_{net}), optical efficiency (η_0), incident angle modifier (IAM), a shading loss factor (η_{shad}), an end loss factor (η_{endl}), a reflecting mirror cleanliness factor (η_{clean}), and the current focus of the collector (f).

$$\dot{Q}_{PTC} = DNI \cdot A_{net}\eta_0 IAM(\theta_i)\eta_{shad}\eta_{end}\eta_{clean}f \tag{11}$$

The peak optical efficiency of the PTC is calculated using Eq. (2). The incident angle modifier (IAM) accounts for increasing optical losses and spillage of solar radiation with increasing incident angle. This modifier depends on the incident angle (θ_i) in degree, shown in Figure 7, and is simulated by the second-order equation (Benz 2008, p. 27).

$$IAM = \max\left(0, (1 + 0.00010596 \cdot \theta_i - 0.00017091 \cdot \theta_i^2)\right) \tag{12}$$

The shading factor (η_{shad}) takes into account the shading of the PTC using the aperture width (w_{PTC}) and distance between PTCs ($l_{radial\_distance}$) in conjunction with the PTC tracking angle (ρ_{PTC}) shown in Figure 7.

$$\eta_{shad} = 1 - \max\left(0, \frac{w_{PTC} - l_{radial\_distance}\cos\rho_{PTC}}{w_{PTC}}\right) \tag{13}$$

Shading occurs during start-up, when the absolute value of the tracking angle ($|\rho_{PTC}|$) is higher than 70.5°. Because only one PTC loop is simulated, the model reflects shading for all PTC loops in the SF. The fact that some PTCs do not suffer shading during start-up or shut-down is neglected. This is neglected in the simulation. The factor (η_{end}) accounts for PTC end losses due to a solar ray at the end of the PTC loop not being incident on the PTR when the incident angle is higher than 0°. It can be calculated using focal length (l_f) and PTC length (l_{PTC}).

$$\eta_{end} = 1 - \frac{l_f \tan\theta_i}{l_{PTC}} \tag{14}$$

End losses are only considered at the HTF inlet of the first PTC in the loop and at the outlet of the last PTC, represented by C1 and C4 in Figure 6, respectively. Therefore no end losses and end gains between the PTCs are accounted for. Dust on the PTC surface decreases PTC reflectivity, necessitating periodic washing.

Between washing processes, the reflectivity is decreased linearly by 0.45% per day. The model applies an average cleanliness factor (η_{clean}) of 0.98 (Mohr 1999, p. 62ff). The focus factor (f) simulates PTCs being defocused when the hot storage tank is full. The model sets this factor at a value between 0 and 1, with 0 being a completely defocused state, such as occurs at nighttime, and 1 being normal PTC operation mode. Because only one PTC loop is simulated, the model defocuses all PTCs in the SF using the same factor. The defocusing or disconnecting of sub-SFs is not simulated. While the PTC is in defocused mode, mass flow into the SF is equal to design mass flow into the SG. If the hot tank level falls below 100%, the PTC is refocused and the focus factor set to 1 again. This process is shown in Figure 9.

The heat losses for the 2008 Schott PTR 70 receiver model were tested at NREL between 100° C and 500° C in 50° C increments. With the resulting equation (Burkholder 2009, p. 1)

$$\dot{q}_{loss,2008,PTR\ 70} = 0.141 \cdot T_{PTR} + (6.48 \cdot 10^{-9}) \cdot T_{PTR}^4 \qquad (15)$$

the heat losses can be calculated in watts per meter (W/m). The absorber temperature unit in the above correlation is ° C. The resulting curve with an uncertainty of $\pm$ 10 W/m can be found in Figure 10. Eq. (15) is used for the Ebsilon model, which therefore reflects a PTR temperature that is almost the same as the HTF temperature.
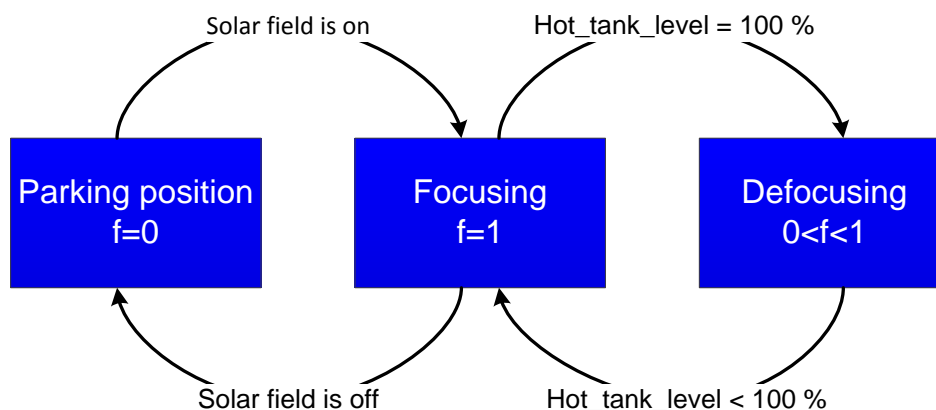
Figure 9: Scheme of the PTC focus control

$$T_{PTR} \approx T_{HTF} \tag{16}$$

NREL provides further equations to calculate the PTR heat losses if the vacuum is not maintained or the absorber coating damaged (Burkholder 2009, p. 19ff). These eventualities are taken into account with the simple factor η_{broken} in Eq. (2), set at 0.98, which reduces the optical performance of the PTR and therefore of the whole PTC (Lippke 1995).

The effective heat input into the HTF ($\dot{Q}_{HTF}$) of average temperature ($\bar{T}_{HTF}$) over one PTC of length (l_{PTC}), and can be calculated by combining Eq. (10), (11), and (15) with

$$\dot{Q}_{HTF,j} = \dot{q}_{loss,j}(\bar{T}_{HTF,j})l_{PTC,j} - \dot{Q}_{sun,j}, \;\; j = C1, C2, C3, C4 \;\; . \tag{17}$$

Totalling the heat input into the HTF from Eq. (17) for all four collectors (C1, C2, C3, and C4) shown in Figure 6,

$$\dot{Q}_{loop} = \sum_j \dot{Q}_{HTF,j}, \;\; j = C1, C2, C3, C4 \tag{18}$$

the temperature rise over the collector loop can be calculated using Eq. (3).
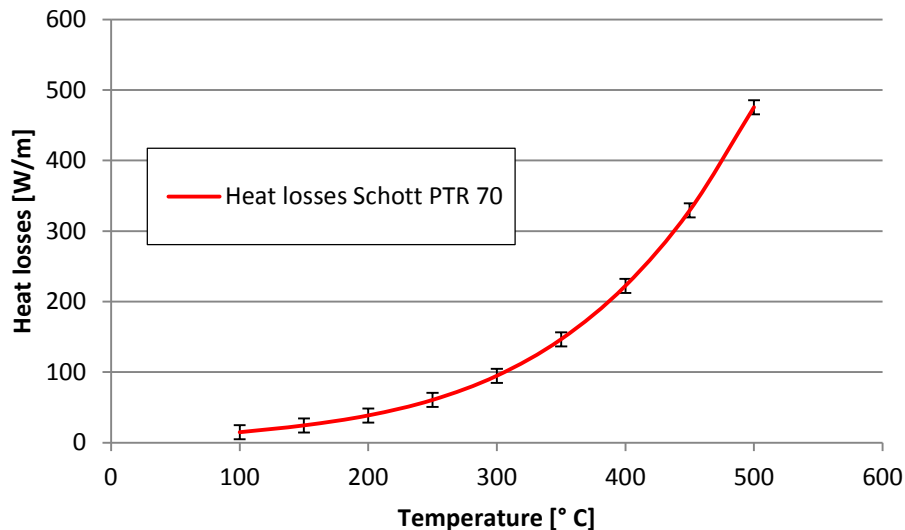
Figure 10: Heat losses of the Schott PTR 70 receiver tested at NREL – uncertainty of ± 10 W/m is shown

To account for PTC pressure drop at the design point and under off-design conditions, the implemented pressure drop function in component 113 is used. The model includes piping element P1, shown in Figure 6, at the end of the PTC loop to reflect additional pressure losses in the interconnections between the PTCs.

3.1.5 Pipings and headers

To calculate the heat losses and pressure drops in feeders 1 and 2, and the header, shown in Figure 6, the length of these components must be calculated. The length of feeder 1 (l_{f1}) is calculated using Eq. (19) and the parameter $j = 2$ for the 2 H and H layouts or $j = 4$ for the 3/2 H layout. It depends on the length of the collector and the width of the BOP (w_{BOP}). Spacing between the sub-SFs of 25 m is assumed in the model.

$$l_{f1} = j \cdot l_{PTC} + \frac{w_{BOP}}{2} + 25 \, m, \;\; j \, \epsilon \, \{2,4\} \tag{19}$$

The length of feeder 2 (l_{f2}), only available in the 2 H layout, is also calculated using the width of the BOP and the spacing between sub-SFs.

$$l_{f2} = 4 \cdot l_{PTC} + \frac{w_{BOP}}{2} + 25 \, m \tag{20}$$

The calculation of the length of the header (l_h) depends on the number of branches (n_{br}) and on the radial distance between PTCs ($l_{radial\_distance}$), given in Appendix H for three PTC types.

$$l_h = (n_{br} - 1)l_{radial\_distance} \cdot 2 \tag{21}$$

The calculated lengths in Eqs (19), (20), and (21) are not equal to the lengths of the piping elements in a real solar thermal power station. Because of the high temperature differences in hot piping elements, high thermal stress due thermal expansion occurs. The model accounts for this by using quadratic u-pipe elements of length (l_{u-pipe}), as shown in Figure 11. These have the distance (D_{u-pipe}) between them. Because the diameters of feeders 1 and 2 are different, resulting in different thermal tensions, the model uses a u-pipe length for feeder 1 ($l_{u-pipe,f1}$)

and for feeder 2 ($l_{u-pipe,f2}$). The diameter of the cold header decreases constantly in the upstream direction, so the model uses an average u-pipe side length to approximate it, as shown in Figure 11. Generally, the following context can be stated.

$$l_{u-pipe,f1} > l_{u-pipe,f2} > l_{u-pipe,h} \tag{22}$$

The number of u-pipe elements ($n_{u-pipe,i}$) can be calculated by combining Eqs (19), (20), and (21) with

$$\lfloor n_{u-pipe,j} \rfloor = \frac{l_j}{D_{u-pipe}} , \quad j = f1, f2, h \; . \tag{23}$$

The real combined length of feeder 1 ($l_{f1,real}$), feeder 2 ($l_{f2,real}$), and the header elements ($l_{h,real}$) is therefore given by combining Eqs (19), (20), (21), and (23) with

$$l_{j,real} = l_j + n_{u-pipe,j} l_{u-pipe,j} \cdot 2, \qquad j = f1, f2, h \; . \tag{24}$$

Using the real header length, the average length of the header pipeline between PTC rows ($l_{rowdistance}$) can be calculated, as shown in Figure 16.

$$l_{rowdistance} = \frac{l_{h,real}}{2 \cdot (n_{br} - 1)} \tag{25}$$

Unlike those in the PTRs, heat losses in piping elements result mainly from convection. This can be seen in Figure 12, which shows the heat losses of a
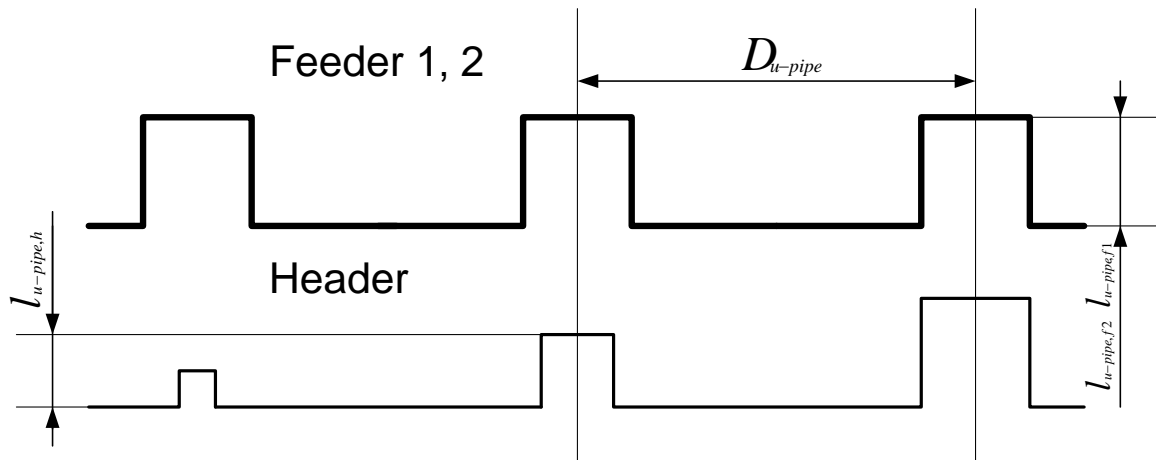
Figure 11: Geometry of the headers and feeders used in the Ebsilon model of the solar thermal power plant

piping element tested by ENEA from 300° C to 420° C. The insulation was stainless steel foil, 50 mm calcium silicate, 200 mm mineral wool, and an aluminum jacket (Maccari 2006). Heat loss ($\dot{Q}_{loss,j}$) is modelled by means of a linear equation using the heat loss factor for pipes ($k_{hl,pipe}$), real length of piping elements from Eq. (24), average temperature of the pipe ($\bar{T}_j$), ambient temperature (T_{amb}), design temperature of the hot tank ($T_{HT,D}$) and design ambient temperature ($T_{amb,D}$).

$$\dot{Q}_{loss,j} = k_{hl,pipe} \cdot l_{j,real} \cdot \frac{(\bar{T}_j - T_{amb})}{(T_{HT,D} - T_{amb,D})}, \; j = f1, f2, h \qquad (26)$$

In calculating the pressure drops inside the feeder pipes, the Prandtl / v. Karman equation, which depends only on the wall roughness (ε), is used to calculate the friction force (ξ).

$$\sqrt{\xi} = 2 \cdot \log\frac{1}{\varepsilon} + 1.14 \qquad (27)$$

The model assumes therefore hydraulically smooth flow. For each bending in the pipe, a resistance coefficient (ξ_b) of 0.1 is used (VDI 2006, p. Lac 5). The pressure drop (Δp_j) is therefore calculated using Eqs (23), (24), (27), and (28).
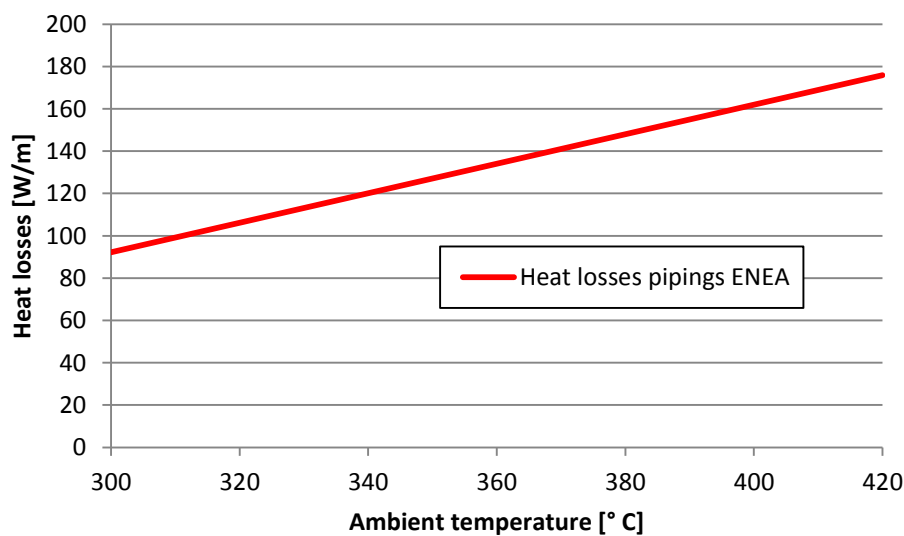
Figure 12: Heat losses of piping elements tested by ENEA adopted from (Maccari 2006)

$$\Delta p_j = \left(\xi \frac{l_{j,real}}{d_{i,j}} + 4 \cdot n_{u-pipe,j} \cdot \xi_b \right) \frac{\rho v_D^2}{2}, \quad j = f1, f2, h \tag{28}$$

The inner pipe diameter ($d_{i,j}$) is calculated using the mass flow through feeder 1 or 2 at the design point and the constant design velocity (v_D), which is between 1.5 to 3 m/s. The optimal design velocity depends on a cost analysis (VDI 2006, p. Lab2).

The pressure drop in the header is not constant because the pipe diameter changes at each branching section. For this reason, Ebsilon uses a second-order function to calculate the pressure drop at a given position (x) in the pipe.

$$\Delta p(x) = a_1 + a_2 x + a_3 x^2, \quad x \in \left[0; l_{h,real}\right] \tag{29}$$

The parameters a_1, a_2, and a_3 of Eq. (29) are calculated using three conditions:

- Pressure drop at the inlet: $\Delta p(x = 0) = 0$
- Pressure drop at a specific user-defined branch IDP: $\Delta p(x = 2 \cdot (n_{IDP} - 1)l_{rowdist})$
- Pressure drop at the last branch: $\Delta p\left(x = l_{h,real}\right)$

The user-defined specific branch IDP is selected, in order that the deviation of pressure ($\Delta p_{deviation}$), calculated using Eq. (30), be minimal. The specific pressure drop in one section between two branching elements (Δp_j) in Eq. (30) is calculated using Eq. (28).

$$\Delta p_{deviation} = \int_0^{l_{h,real}} ax^2 + bx + c \ dx - \sum_1^{n=n_{br}-1} \Delta p_j(x) \tag{30}$$

3.1.6 Solar thermal storage system

As shown in Figure 6, the Ebsilon model uses transient hot and cold storage tanks with the same storage capacity, large enough to store the entire HTF fluid mass. The mass of the HTF inside the hot tank

$$m_{HTF,HT} = \dot{m}_{HTF,PB,D} t_{HT} \tag{31}$$

is calculated using a specific time (t_{HT}) the hot storage tank can feed the SG with a mass flow ($\dot{m}_{HTF,PB,D}$) so that the PB is able to produce electricity at 100% load. The optimal storage time for a given power plant, as dictated by the economic efficiency, depends on its location.

Because molten salt has a low vapour pressure, as described in Chapters 2.4 and 2.5, the storage system operates at the ambient pressure of 1 bar, assumed to be constant during the entire operation of the power plant. Storage tank heat losses are also accounted for in the model. "According to the experience (in the Andasol I solar thermal power plant, editor's note), both tanks approximately lose less than 1ºC per day when at maximum capacity" (Relloso 2009). The hot tank of the Andasol I power plant contains 28,500 metric tons of solar salt as storage medium ($m_{HT,1}$) at 386° C ($T_{HT,1}$). The tank has a height ($h_{HT,1}$) of 14 m and a diameter ($d_{HT,1}$) of 38.5 m (Relloso 2009). Due to good insulation, convection and radiation inside the hot tank, it is assumed that the inside wall temperature of the storage tank is the same temperature as the storage fluid ($T_{HT,1}$). As a result, the specific heat flow through the walls of the hot tank

$$\dot{q}_{HT,1} = U_{HT,1}\left(T_{HT,1} - \bar{T}_{amb,1}\right) \tag{32}$$

is assumed to be constant and can be calculated using the overall heat transfer coefficient ($U_{HT,1}$). For any full hot storage tank with the same heat transfer coefficient (and thus the same insulation) with a specific mass of salt as storage medium ($m_{HT,2}$) at a given temperature ($T_{HT,2}$), height ($h_{HT,2}$) and diameter ($d_{HT,2}$), the temperature loss over one day can be calculated as follows.

$$\Delta T_{HT,2} = \frac{\left(mc(T_{HT,1})\right)_{HT,1} \cdot 1° C}{\left(mc(T_{HT,2})\right)_{HT,2}} \cdot \frac{(dh + 0.5 \cdot d^2)_{HT,2}\left(T_{HT,2} - T_{amb,2,D}\right)}{(dh + 0.5 \cdot d^2)_{HT,1}\left(T_{HT,1} - \bar{T}_{amb,1}\right)} \tag{33}$$

The model assumes that the heat flow into the ground is equal to heat flow into the environment and that the average ambient temperature ($\bar{T}_{amb,1}$) is 25° C. The Ebsilon software uses a temperature loss coefficient (QLOSSR) with the unit kW/K for the tank component.

$$QLOSSR = \frac{(mc\Delta T)_{HT,2}}{(T_{HT,2} - T_{amb,2,D}) \cdot 86400s \cdot 1000} \tag{34}$$

It can be calculated by combining Eqs (33) and (34).

Each tank is equipped with one variable-speed salt submersion pump. The model assumes a constant isentropic efficiency of 70% and mechanical efficiency of 99.5%. The pumps are driven by a generator, component 29, with an electrical efficiency of 99% and mechanical efficiency of 99.5%.

3.1.7 Auxiliary heater

As illustrated in Figure 13, the Ebsilon simulation uses a very simplified model of the auxiliary heater, shown as part of the SF in Figure 6. The mass flow into the AH is separated by a logical component, after which the temperature of the HTF is set to the design temperature of the hot tank. Thus the heat input into the HTF over the AH

$$\dot{Q}_{AH} = \dot{m}_{AH,D}(c_2 T_2 - c_1 T_1) \tag{35}$$

depends only on the HTF input temperature (T_1) because the outflow temperature (T_2) and the mass flow of the AH at design point ($\dot{m}_{AH,D}$) are assumed to be constant. This means that the model takes no account of off-design behavior or pressure losses, assuming instead that the AH always works at the design point. Its efficiency (Wagner 2005, p. 260)

$$\eta_{AH} = \frac{\dot{Q}_{AH}}{\dot{m}_{gas} H_u} \quad , \tag{36}$$

assumed to be 90%, is constant and does not depend on environmental
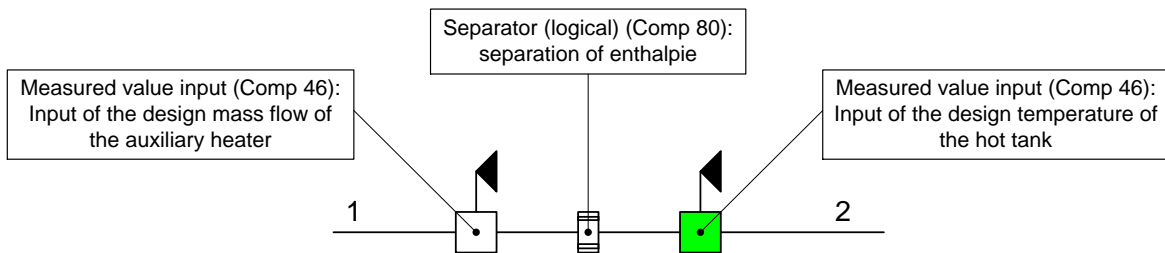
Figure 13: Model of the auxiliary heater in Ebsilon

parameters, e.g. the ambient temperature or the HTF input temperature. The AH's impact on the LECs can thus be determined using the annual yield calculation.

3.1.8 Transient behavior of the solar field

Besides the transient behavior of the storage tank, described in Chapter 3.1.6, the transient system behavior of the SF is modelled by the indirect storage component, shown in Figure 14. It is a pipe model that simulates transient heat exchanges between the pipe and the fluid flowing through it. The two-dimensional Fourier differential equation, rotational symmetry of the pipe is assumed,

$$\frac{\partial T_{IS}}{\partial t} = \boldsymbol{a}_{IS}\left(\frac{\partial^2 T_{IS}}{\partial x^2} + \frac{\partial^2 T_{IS}}{\partial y^2}\right) \tag{37}$$

is discretized using the finite volume method on an approximately 30x30 Cartesian grid, which represents the wall of the indirect storage component. The time is discretized using the Crank-Nicolson method (Pulyaev 2011, p. 25). As stated in Eq. (37), the thermal diffusivity ($\boldsymbol{a}_{IS}$) of the indirect storage element is assumed to be constant. As shown in Figure 14, the heat exchange between the indirect storage and the HTF

$$\dot{Q}_0(x,t) = \bar{\alpha}_{i,HTF,IS}\big(T_{IS}(x,t) - T_{HTF}(x,t)\big)\Delta x \pi d_{i,IS} \tag{38}$$

is calculated in a local volume cell (Δx) and is therefore a third-type boundary condition (Polifke 2005, p. 56ff). Assuming

$$\frac{\partial \rho_{HTF}}{\partial t} \approx 0 \tag{39}$$

for the HTF, the conservation of energy in one volume cell at the time instant (t)

$$\dot{Q}_0(x) = \dot{m}_{IS}\left(\big(c(T_{HTF,out})T\big)_{HTF,out} - \big(c(T_{HTF,in})T\big)_{HTF,in}\right) \tag{40}$$

can be calculated using Eq. (38), the mass flow through the indirect storage ($\dot{m}_{IS}$), as well as the HTF temperature at the input ($T_{HTF,in}$) and output ($T_{HTF,out}$) of the volume cell (Pulyaev 2011, p. 25).

As shown in Figure 6 and Table 7, the model assumes transient system behavior for all four collectors (C1, C2, C3, and C4), as well as for the hot header and feeder pipelines. In order to realize a faster simulation, the model assumes no transient behavior for the cold piping elements, because the temperature change over time in the cold piping elements is far less than that in the hot piping elements

$$\frac{\partial T_{piping,hot}}{\partial t} \gg \frac{\partial T_{piping,cold}}{\partial t} \quad , \tag{41}$$

in which the temperature of the HTF and the piping elements nears solidification temperature during nighttime and upper HTF temperature during normal daytime SF operation. This results in a high temperature difference during SF start-up or shut-down, for example. The temperature gradient is assumed to be much higher on the x-axis than on the y-axis

$$\frac{\partial T_{IS}}{\partial x} \gg \frac{\partial T_{IS}}{\partial y} \quad , \tag{42}$$

and the Cartesian grid is therefore reduced to one increment on the y-axis to improve the speed of the simulation. Discretization in the x-direction has been selected in order that the maximum Courant number (Schilling 2010)

$$C_{j,max} = \frac{v_{j,max}\Delta t}{\Delta x_j} < 1 \quad , \quad j = IS1, IS2, IS3, IS4, IS5, IS6, IS7 \tag{43}$$
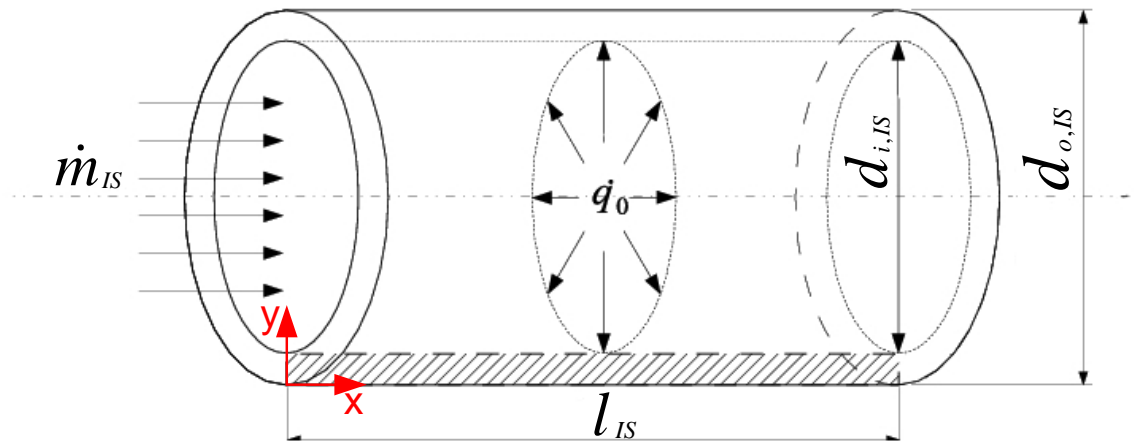
Figure 14: The geometry of the indirect storage element, component 119, adapted from (Pulyaev 2011, p. 23)

be less than one. The Courant number depends on the velocity in the component 119 (v_j), and therefore on the current mass flow into the SF.

Figure 14 shows the geometry of the indirect storage component. A model of the correct thermal inertia of the piping elements requires their inner diameter ($d_{i,IS}$), outer diameter ($d_{o,IS}$), and length (l_{IS}). The Ebsilon model uses the inner heat transfer coefficient ($\bar{\alpha}_{i,HTF,D.IS}$) to simulate heat transfer from the fluid to the indirect storage, as calculated using the Hausen correlation.

$$Nu_{HTF,D,j} = 0.037\big(Re_{HTF,D,j}^{0.75} - 180\big)Pr_{HTF,D,j}^{0.42}$$

$$j = IS1, IS2, IS3, IS4, IS5, IS6, IS7 \tag{44}$$

$$2300 < Re_{HTF,D,j} < 10^6, \quad 0.6 < Pr_{HTF,D,j} < 1000$$

The model uses average HTF properties over the indirect storage at the design point to calculate the Nusselt ($Nu_{HTF,D,j}$), Reynolds ($Re_{HTF,D,j}$), and Prandtl ($Pr_{HTF,D,j}$) numbers. Eq. (46) has been tested at temperatures ranging from 400° C to 500° C with solar salt by (Coscia 2011). In calculating the heat transfer coefficients, the off-design simulation neglects the deviation of the HTF properties and therefore of the Prandtl number. On this assumption, the heat transfer coefficient during off-design behavior

$$\bar{\alpha}_{Off-D} = \bar{\alpha}_D \left(\frac{\dot{m}_{off-D}}{\dot{m}_D}\right)^e \tag{45}$$

can be estimated, using the design heat transfer coefficient from Eq. (44), the design mass flow ($\dot{m}_D$), and off-design mass flow ($\dot{m}_{off-D}$) of the HTF. The exponent (e) of 0.75 corresponds with Eq. (44).

Neither heat losses to the environment nor pressure drops are simulated in the indirect storage component because the model has already accounted for these with piping elements P1, P2, P4, and P5, as shown in Figure 6. The insulation thickness ($t_{insulation,IS} \rightarrow \infty$) is therefore assumed to be very great, and the outer heat transfer coefficient ($\alpha_{o,IS}$) is set to zero, reflecting an adiabatic system.

3.1.8.1 Collector

The geometric parameters of the three chosen PTCs are listed in Appendix H. The model uses the length and thickness of the PTR calculated from the outer and inner diameters for the four indirect storage elements (IS1, IS2, IS3 and IS4) shown in Figure 6. It discretizes one collector loop with four units, each with a PTC simulated by component 113 and an indirect storage element. As described in Chapter 3.1.4, the PTC component simulates heat input into the HTF, after which the indirect storage element simulates a hot HTF front delay and an HTF heat output due to the heating of the PTR steel mass. A real simulation of SF behavior would account for an infinite number of units made up of one PTC and one indirect storage element. A discretization of four is a compromise between precision and speed of simulation.

Figure 15 shows an example of a simulated start-up process in Las Vegas on June 20, 2008 of the reference SF, described in Chapter 4.1. The chart's x-axis reflects simulated time intervals of 10 minutes. The HTF, solar salt, is heated from 270° C to the hot tank design temperature of 510° C. The transient process begins at 4:25 local time and lasts until 6:05. At 4:25, the matrix of the indirect storage is initialised with the current stationary solution. Before and after this time interval, the SF operates in a quasi-stationary state. The steady state solution for each time increment is used to calculate the HTF mass flow ($\dot{m}_{HTF}$) through the SF. Therefore the derivation

$$\frac{\partial \left(\frac{\partial T_{HTF}}{\partial x} \right)}{\partial t} \approx const. \quad , x \in [0; l_{is}] \tag{46}$$

is approximately constant, and each steel pipe element at position x is heated to its stationary temperature. This results in a fast start-up process. The stationary HTF mass flow is predicted using the forecast loop, shown on the left border in the screenshot of the Ebsilon simulation in the Appendix A. The temperature in the PTC loop from the cold tank ($T_{HTF,in}$) is shown as a dark blue line. Because the hot HTF from the SF is pumped through the recirculation loop, shown in Figure 6, back to the cold tank during start-up, the tank's temperature rises. At 6:25 local
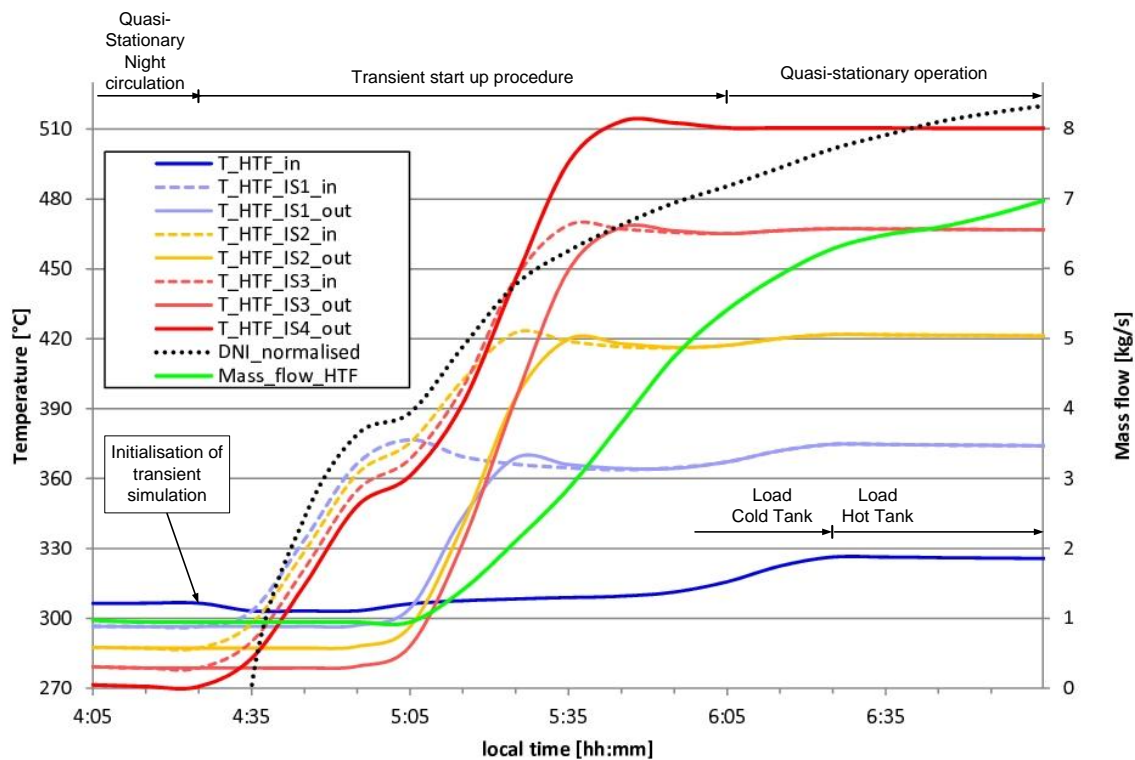
Figure 15: Simulated start-up process of the solar field with solar salt as HTF from minimum temperature of 270° C to operating temperature of 510° C on June 20, 2008 in Las Vegas

time, loading of the hot tank begins, and the temperature of the cold tank becomes quasi-stationary.

The input temperature of the indirect storage elements is represented by a dashed, the output temperature by a continuous line. Unit one, consisting of PTC C1 and indirect storage element IS1, reaches stationary conditions first, followed after an interval by the other units until the start-up procedure is finished and the SF begins quasi-stationary operations at 6:05.

3.1.8.2 Header

The model simulates the instationary cascaded header piping with a given number of branches (n_{br}), shown in Figure 16, using a simple pipe with constant inner diameter ($d_{i,rep}$) and length (l_{rep}) as representative header model.

This model should have the same thermal inertia as the cascaded header. Thus the mass of molten salt and the mass of the steel in the representative pipe must be equal to the corresponding masses of the ideally cascaded header if the same

energetic effort during heating is to be obtained. The throughput time of the representative header should also be equal to the average throughput time of the original header in order to simulate similar delay (Hirsch 2010).

Therefore the mass of the molten salt in the ideally cascaded header

$$m_{salt} = \sum_{j=1}^{n_{br}-1} m_j = \frac{2 \cdot l_{rowdist}}{v_D} \dot{m}_{subfield,D} \sum_{j=1}^{n_{br}-1} \frac{n_{br} - j}{n_{br}}$$

$$= \frac{2 \cdot l_{rowdist}}{v_D} \dot{m}_{subfield,D} \frac{n_{br} - 1}{2}$$

(47)

can be calculated using the mass flow into the subfield at the design point ($\dot{m}_{subfield,D}$), the average length of the header pipeline between two PTC rows from Eq. (25), and the assumed constant design velocity (v_D), as outlined in Chapter 3.1.5. As previously stated, Eq. (47) must be equal to Eq. (48), the equation to calculate the molten salt mass in the representative pipe ($m_{salt,rep}$).

$$m_{salt,rep} = \frac{\pi}{4} \cdot d_{i,rep}^2 l_{rep} \bar{\rho}_{salt}$$

(48)

Using the maximum inner diameter of the ideally cascaded header as the inner diameter of the representative pipe, the length of the representative pipe can be calculated by combining Eqs (47) and (48).

$$l_{rep} = l_{rowdist} \cdot (n_{br} - 1)$$

(49)

The steel masses of the representative pipe
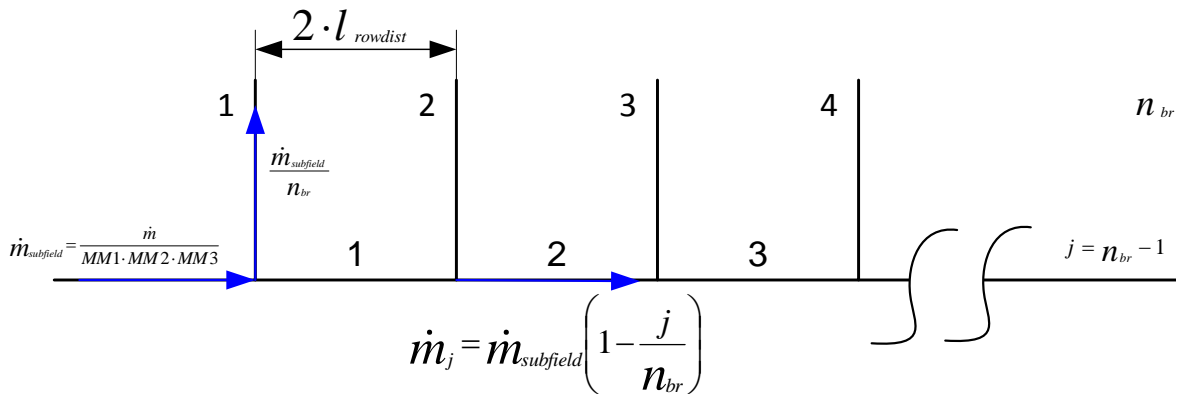
Figure 16: Schematic of the distributing header with a specific number of branches adapted from (Hirsch 2010)

$$m_{steel,rep} = \frac{\pi}{4} \cdot l_{rep} \cdot \left(\left(d_{i,rep} + 2 * \boldsymbol{t}_{rep} \right)^2 - d_{i,rep}^2 \right) \cdot \rho_{IS} \tag{50}$$

must also be identical to the steel mass of the ideally cascaded header ($m_{steel,br}$).

$$m_{steel,br} = \sum_{j=1}^{n_{br}-1} \frac{\pi}{4} \cdot 2 \cdot l_{rowdist} \cdot \left(\left(d_{i,br,j} + 2 * \boldsymbol{t}_{IS} \right)^2 - d_{i,br,j}^2 \right) \cdot \rho_{IS} \tag{51}$$

The model assumes constant thickness ($\boldsymbol{t}_{IS}$) for all elements of the ideally cascaded header. Combining Eqs (50) and (51) allows the thickness of the representative pipe ($\boldsymbol{t}_{rep}$) to be calculated. The average throughput time of a header ($\bar{t}$) with a specific number of branches (n_{br}) can be calculated using the constant throughput time of a section ($t_{section}$)

$$\bar{t} = \frac{1}{n_{br}} \sum_{j=0}^{n_{br}-1} t_{section} \cdot j = \frac{1}{n_{br}} \cdot \frac{2 \cdot l_{rowdist}}{v_D} \sum_{j=0}^{n_{br}-1} j$$

$$= \frac{l_{rowdist}}{v_D} (n_{br} - 1) = \frac{l_{rep}}{v_D} = t_{rep} \tag{52}$$

and is equal to the throughput time of the representative header (t_{rep}).

3.1.8.3 Feeders 1 and 2

To simulate the thermal inertia of feeders 1 and 2, the model assumes a constant thickness ($\boldsymbol{t}_{IS}$) and design velocity (v_D), as stated in Chapter 3.1.8.2. The inner diameter of feeders 1 and 2

$$d_{i,j} = \sqrt{\frac{4\dot{m}_{j,D}}{\bar{\rho}v_D}}, \quad j = f1, f2 \tag{53}$$

is calculated using the mass flow through the component at the design point ($\dot{m}_{j,D}$). The length of the feeders is determined using Eq. (24).

Feeder pipe thickness is a further design parameter for thermal optimization. Thick pipes have a damping effect on the SF. That means that, during start-up, thicker pipes delay the hot HTF front more because they are able to store more heat. This effect is reversed during shut-down. It is possible to use thick pipes as passive heating elements in order to prevent solidification during nighttime operations.

3.2 Power block

The power block is based on a conventional thermal power plant. The sub-critical steam generator, a once-through boiler, is the only non-conventional part. State-of-the-art SGs are based on fossil fuels, e.g. coal or oil, and the heat is transferred by convection and radiation to the water-steam cycle. In the once-through boiler with salt as HTF, heat is transferred by convection only, and the behavior of such an SG is therefore different from state-of-the-art SGs.

The model of the PB is shown in Figure 17. In the SG, the water is heated to boiling by the economiser (Eco) and then passes the evaporator (Eva) and the superheater (SH). The resulting live steam with temperatures of up to 540° C is fed into the high-pressure stages (HPS1, HPS2) of the steam turbine and reheated in the reheater (RH) of the SG before it is fed into the five low-pressure stages (LPS1, LPS2, LPS3, LPS4, LPS5). The mechanical energy produced by the steam turbine is converted into electrical energy by the generator (G). The exhaust steam from the steam turbine is converted into water by the condenser (C). Steam content reaches about 90%. The turbine back-pressure depends on the type of the cooling system, as well as on ambient factors such as dry-bulb temperature and humidity (California Energy Commission 2002, p. 4-4).

The condensate is pumped by the condensate pump (CP2) through three feed water heaters, each consisting of an after cooler (AC1, AC2, AC3) and a preheater (PH1, PH2, PH3). Extracted steam from the low-pressure turbine stage is used to preheat the feed water. Low-pressure vapour is also used for preheating in the feed water tank (D). Finally, the feed water pump (FWP) pumps the fluid through two further preheaters (AC4, PH4, AC5, PH5), which are fed by extracted steam from the high-pressure turbine. For off-design operations, the model assumes live steam extraction (AC6, PH6) to prevent low feed water temperatures in the economiser resulting in solidification of the salt at the outlet of the SG.
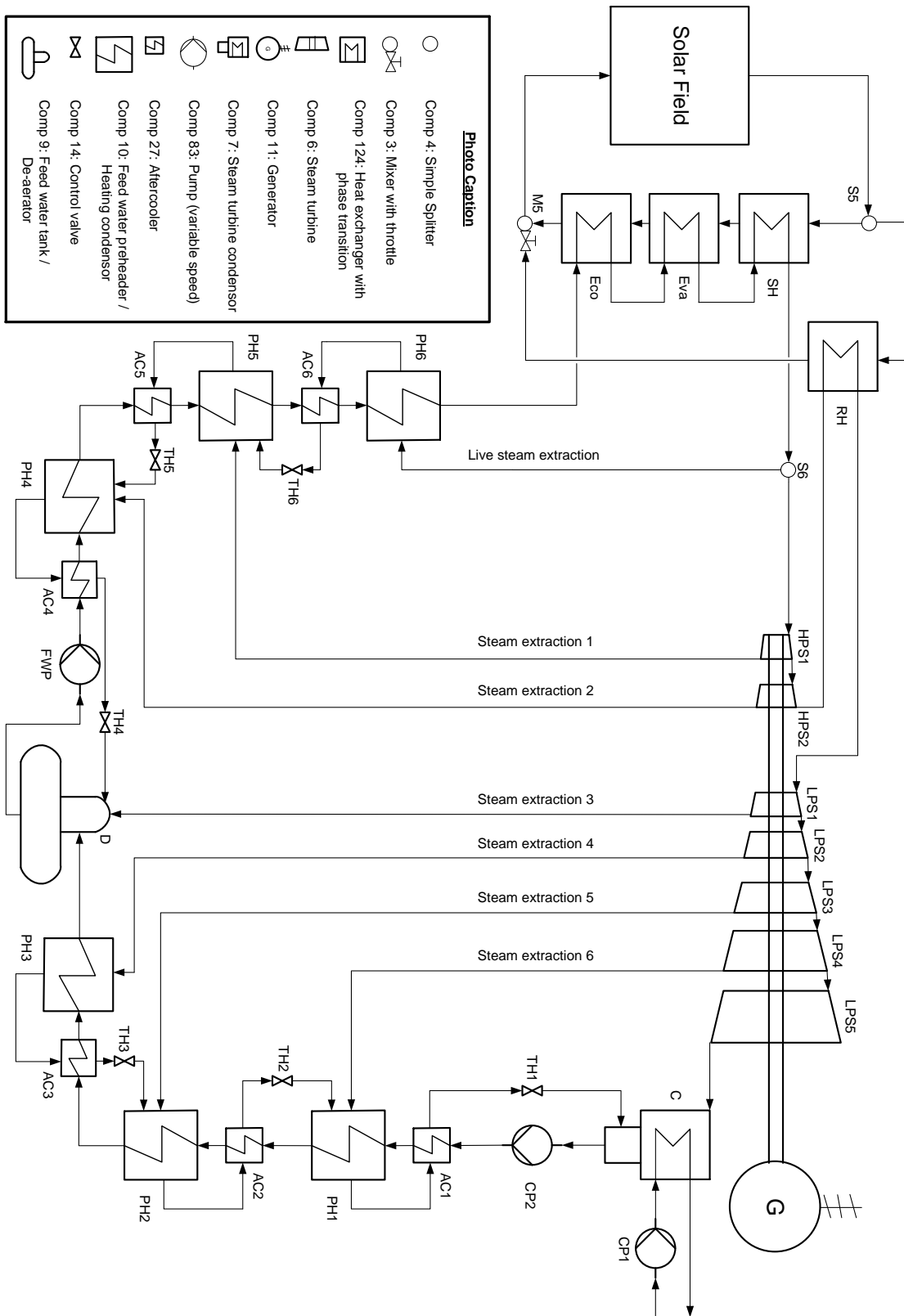
Figure 17: Model of the power block with Ebsilon

Appendix I shows the T,s diagram of the reference plant, described in Chapter 4.1.2, based on the scheme shown in Figure 17. The live steam parameters are 150 bar and 500° C at the design point, and the steam is reheated up to 500° C at a pressure of 30 bar before it is fed into the low-pressure stage. The turbine back-pressure is 0.08 bar, and the steam content is 89.7%. The model assumes an isentropic efficiency of 88% at the design point of the steam turbine.

3.2.1 Steam generator

The modelled SG is a Benson once-through type. The water is preheated, evaporated, and superheated in a single pass. During off-design conditions, the start and end point, as well as the length of the evaporation zone, shifts inside the tubes according to the mass flow of the HTF and the feed water. Either a higher-than-design-point HTF flow or a lower-than-design-point feed water flow shortens the evaporation zone and shifts it closer to the feed water inlet or the HTF outlet, respectively. This effect is reversed for a lower-than-design-point HTF mass flow, or a higher-than-design-point feed water flow (Klefenz 1973, p. 66). Forced flow in the evaporator is only generated off-design from 15-35% PB load by a circulator pump (Grote 2007, p. L53). The Ebsilon model does not simulate this low off-design SG circulation.

Figure 18 shows the Q,T diagram of the simulated once-through Benson boiler for the reference plant described in Chapter 4.1.2 at the design point. Solar salt at 510° C is used on the secondary side of the SG. The model assumes the temperature differences between the primary and secondary sides at the SH and RH inlets and the RH outlet to be 10° C. It also assumes the temperature difference at the Eva inlet to be 10° C. The entire feed water evaporation takes place in the evaporator at the design point. In off-design, outlet temperatures of live and reheated steam of 500° C are maintained, but the evaporation zone shifts within the SG.
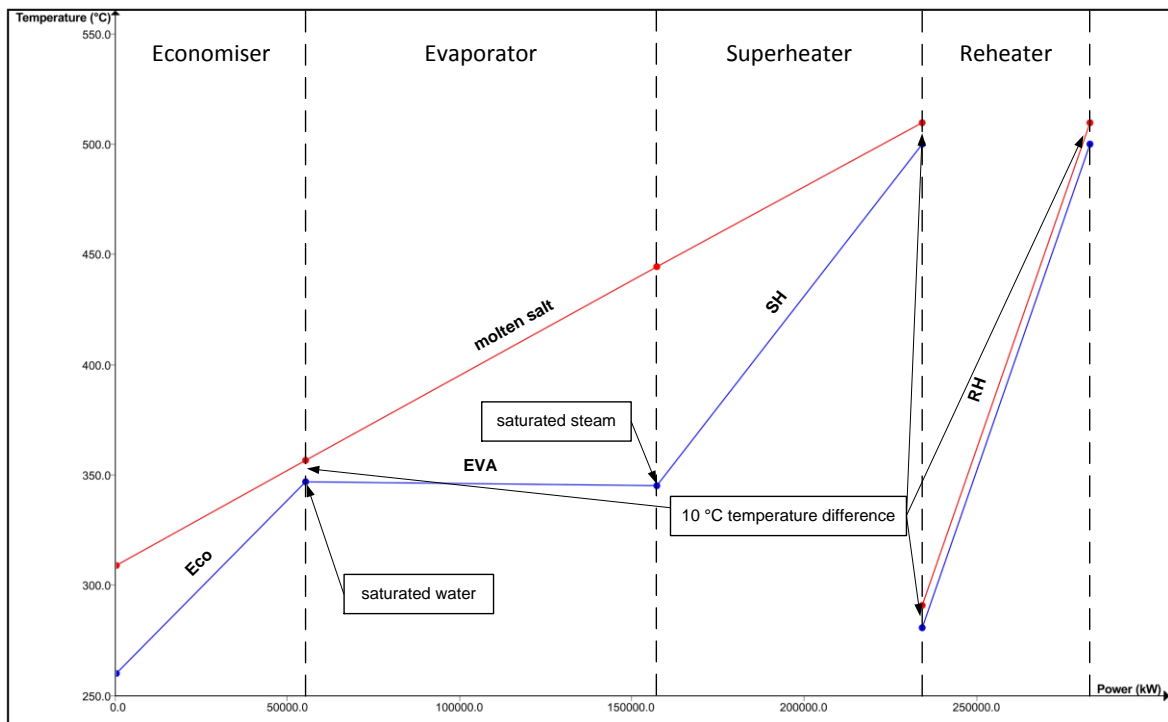
Figure 18: Q,T diagram of a steam generator at the design point for a 125-MW$_e$ power plant with solar salt at 510° C as HTF

The model assumes the geometry of the SG to be a shell and tube heat exchanger with countercurrent flow, as shown in Figure 19. To simulate realistic off-design behavior, the model uses average heat transfer coefficients at the design point of the primary ($\bar{\alpha}_{i,w-s,D}$) and secondary ($\bar{\alpha}_{o,HTF,D}$) sides of the SG.

To calculate the heat transfer coefficient of the HTF side, the model assumes a radial HTF flow around tube bundles and neglects axial flow around the bundles.
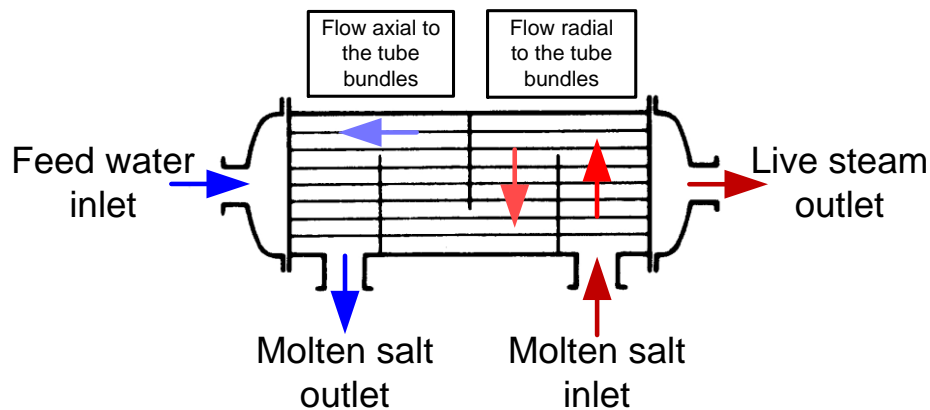
Figure 19: Shell and tube heat exchanger adapted from (VDI 2006, p. Cc1)

Assuming the outer tube diameter ($d_{o,SG}$=0.034 m), and the velocity of the molten salt through the SG at the design point ($v_{HTF,D}$=0.35 m/s), the average heat transfer coefficient at the design point of the Eco, Eva, SH, and RH ($\bar{\alpha}_{i,HTF,D,j}$) can be calculated (Polifke 2005, p. 229f)

$$Nu_{HTF,D,j} = 0.32 \cdot Re_{HTF,D,j}^{0.61} Pr_{HTF,D,j}^{0.31}, \quad j = Eco, Eva, SH, RH$$

$$2 \cdot 10^3 < Re_{HTF,D,j} < 4 \cdot 10^4 \tag{54}$$

by using the average HTF properties over the Eco, Eva, SH, and RH to calculate the Nusselt, Reynolds, and Prandtl numbers. The average heat transfer coefficients of the primary side at the design point of the Eco, SH, and RH ($\bar{\alpha}_{i,w-s,D,j}$) can be calculated, assuming the inner tube diameter ($d_{i,SG}$=0.030 m) and the velocity of the water through the SG at the design point ($v_{water,D}$=1 m/s) (Polifke 2005, p. 233).

$$Nu_{w-s,D,j} = 0.023 \cdot Re_{w-s,D,j}^{0.8} Pr_{w-s,D,j}^{0.33}, \quad j = Eco, SH, RH$$

$$Re_{w-s,D,j} > 10^4, \quad 0.7 < Pr_{w-s,D,j} < 160 \tag{55}$$

The average speed of the steam at the design point in the SH and RH

$$\bar{v}_{steam,D} = v_{water,D} \frac{\rho_{water,D}}{\bar{\rho}_{steam,D}} \tag{56}$$

can be calculated from the mass conservation, assuming constant areas in Eco and SH. To calculate the average heat transfer coefficients of the Eva at the design point ($\bar{\alpha}_{i,w-s,D,Eva}$), (VDI 2006, p. Cc1) proposes an overall heat transfer ($U_{once\text{-}through}$) of between 900 and 3000 W/m²/K. Letting $U_{once\text{-}through} \approx 2200$ W/m²/K, using the average heat transfer coefficient of the HTF in the Eva ($\bar{\alpha}_{o,HTF,D,Eva}$) from Eq. (54), and assuming the heat conductivity (λ_{Eva}) of 25 W/m/K,

$$\bar{\alpha}_{i,w-s,D,Eva} = \cfrac{1}{\cfrac{1}{U_{oncethrough}} - \cfrac{d_{i,SG} \ln\frac{d_{o,SG}}{d_{i,SG}}}{2 \cdot \lambda_{Eva}} - \cfrac{d_{i,SG}}{d_{o,SG}\bar{\alpha}_{o,HTF,D,Eva}}} \tag{57}$$

Table 9: Pressure drops of the steam generator at the design point

Eco	Eva	SH	RH
Primary side (water-steam)			
1 bar	3 bar	6 bar	1 bar
Secondary side (molten salt)			
0.3 bar	0.4 bar	0.3 bar	0.2 bar

can be calculated. The model uses off-design behavior as stated in Eq. (45). The exponent (e) for the HTF side of the SG is 0.61 according to Eq. (54) and 0.8 for the water-vapour side according to Eq. (55).

The pressure drops depend on the length of the pipelines in the SG and are assumed as listed in Table 9.

3.2.2 Steam turbine

Because the Benson once-through boiler does not use a kettle to evaporate the water, it is very flexible, and the turbine operates in sliding-pressure mode. No throttle is used before the steam turbine, and the pumping parasitics of the feed water pump, component FWP in Figure 17, are lower than they would be in the fixed-pressure mode of the steam turbine.

To simulate the off-design behavior of the steam turbine, the model uses a simplified ZOELLY-throttle and assumes the following (Pfleiderer 2005, p. 281):

- The rotational speed of the steam turbine is constant (3000 U/min)
- The temperature of the live steam and the reheated steam is constant, as stated in the Chapter 3.2.1
- The turbine inlet flow cross section is constant (no throttle is used in off-design)

The cone law by Stodola (Pfleiderer 2005, p. 284) is therefore used to model the off-design behavior of the steam turbine and to calculate the steam turbine off-design inlet pressure ($p_{1,off-D,HPS1}$), which is the outlet pressure of the SG. In

Table 10: The parameters of the steam turbine at the design point

	HPS1	HPS2	LPS1	LPS2	LPS3	LPS4	LPS5
Pressure [bar]							
Inlet	150	51	30	16	10	4.50	1.50
Outlet	51	31	16	10	4.50	1.50	0.07-0.5
Efficiency [-]							
Isentropic				0.880			
Mechanical				0.998			

Eq. (58), the pressure at the inlet of the steam turbine stage is marked with the subscript 1 and at the outlet with 2.

$$p_{1,off-D,j} = \sqrt{\left(\frac{\dot{m}_{off-D,j}}{\dot{m}_{D,j}}\right)^2 \left(p_{1,D,j}^2 - p_{2,D,j}^2\right) + p_{2,off-D,j}^2},$$

(58)

$$j = HPS1, HPS2, LPS1, LPS2, LPS3, LPS4, LPS5$$

The model assumes no pressure losses or leakages between turbine stages. This Eqs (58) can therefore be solved, since the outlet pressure of the LPS5 (the turbine back-pressure) is assumed to be constant. The parameters at the design point of the turbine stages are listed in Table 10.

Mechanical efficiency is assumed to be constant, whereas the isentropic efficiency is lower in off-design. This characteristic of the steam turbine depends on the ratio of volume flow in off-design to volume flow at design point and is adopted from the Ebsilon pre-set.

3.2.3 Condenser and cooling system

As stated in Chapter 3.2.2, the model assumes the turbine back-pressure to be constant. It therefore ignores correlation with the dry-bulb ambient temperature or the humidity because the Ebsilon model does not simulate the cooling system. Wet cooling systems have the best performance, are relatively independent of ambient temperatures, and allow turbine back-pressures as low as 0.07 bar. Dry cooling systems have lower performance with turbine back-pressure as high as

0.5 bar. Hybrid cooling systems combine both technologies, and the resulting turbine back-pressure is between those of the dry and wet cooling systems (NREL 2009, p. 14ff). Ebsilon models the cooling system indirectly by assuming a constant turbine back-pressure. The secondary fluid of the condenser, the cooling fluid, has a constant temperature of 20° C at the inlet and 30° C at the outlet.

3.2.4 Feed water heating

Figure 20 shows the feed water heating in the PB, during which condensers (PH1 to PH5) condensate the extracted steam from the turbine stages. Aftercoolers (AC1 to AC5), past the condensers, further increase the feed water's temperature. The components AC6 and PH6 are only activated in low PB off-design. The model assumes the temperature difference at the outlets of these components to be 5° C and the pressure drop of the primary fluid, the feed water, to be 0.05 bar in each component.
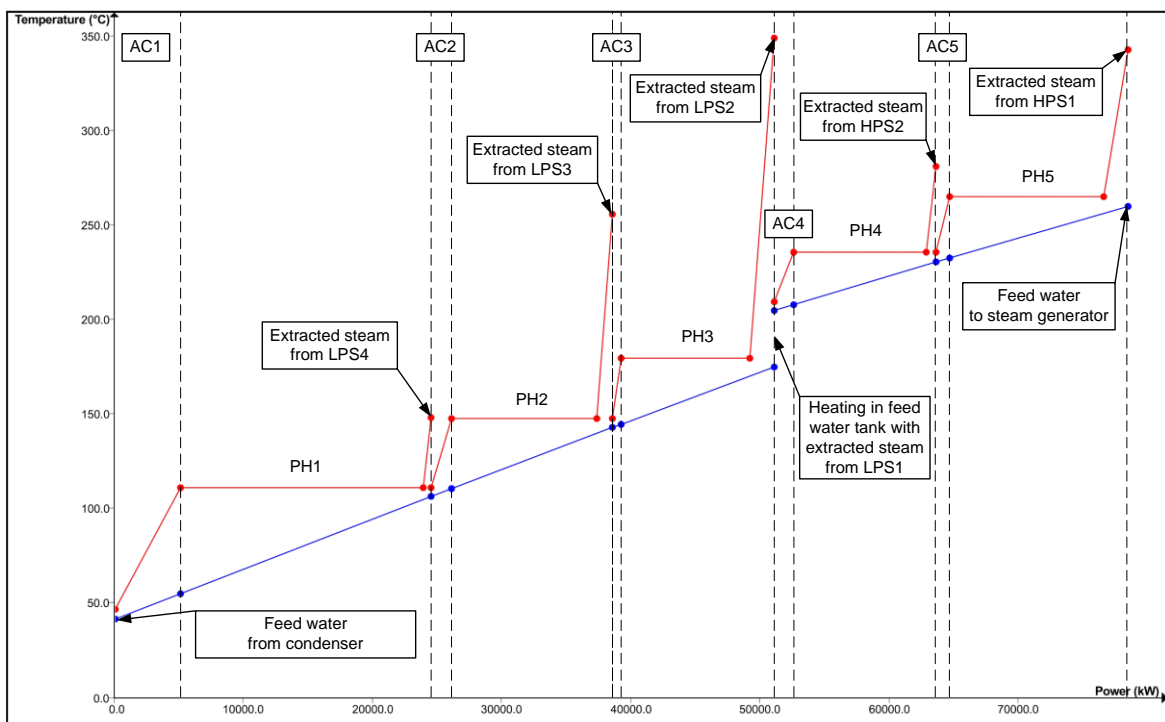
Figure 20: Q,T diagram of the feed water heating at the design point for a 125-MW$_e$ power plant with solar salt at 510° C as HTF – AC6, PH6 are not active

3.2.5 Live steam extraction and off-design of the power block

Chapters 3.2.1 and 3.2.2 describe the off-design behavior of the SG and the steam turbine, respectively. The model also uses off-design behavior, as described in (45), for all heat exchangers. Figure 21 shows the off-design behavior of the entire 125-MW power plant with solar salt at 510° C as HTF, as described in Chapter 4.1.2. The pressure of the live steam, the yellow line in Figure 21, falls linearly with the PB load. Because the turbine back-pressure is nearly zero,

$$p_{2,off-D,LPS5} = p_{2,D,LPS5} \approx 0 \quad , \tag{59}$$

this linear characteristic can be calculated using Eq. (58). The salt mass flow into the SG is also nearly directly proportional to the PB load until the live steam extraction is activated because the temperature of the molten salt at the outlet of the Eco should not fall below its threshold temperature. As Figure 21 shows, at 57% PB load, the temperature of the HTF is close to the threshold temperature, and live steam is extracted. This is the reason for the lower gradient of the salt mass flow into the SG between 35% and 57% load. The PB efficiency also decreases faster when live steam is extracted. During off-design, the relative mass flow through the Eco, Eva, and SH
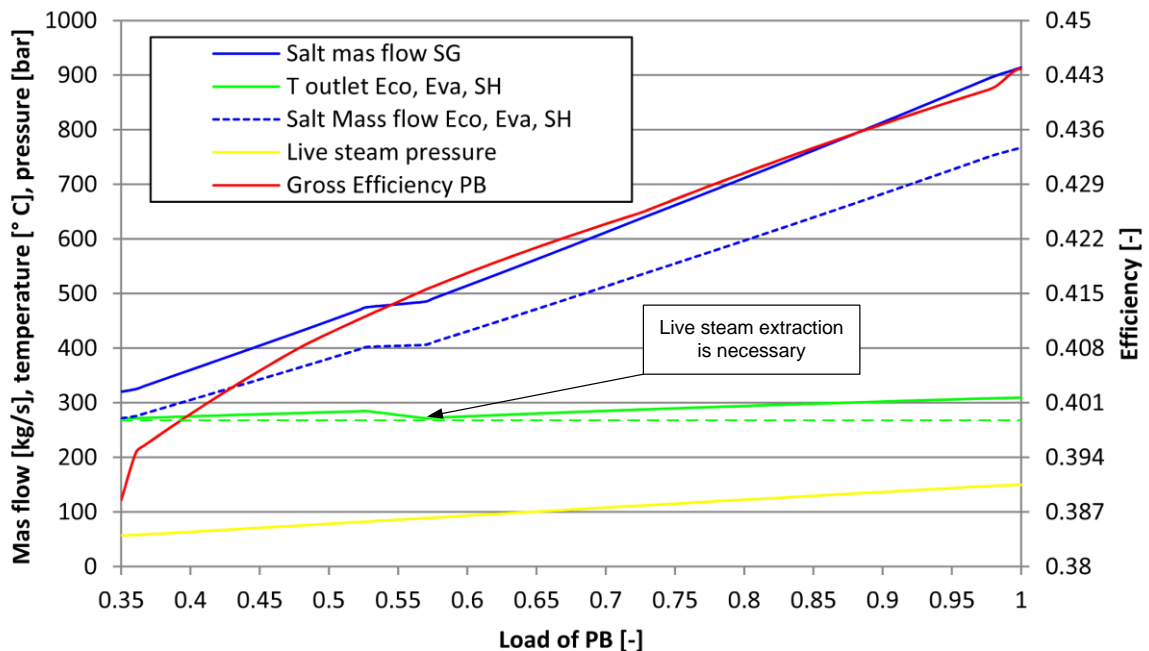
Figure 21: Off-design behavior for a 125-MW$_e$ power plant with solar salt at 510° C as HTF

$$\dot{m}_{rel,Eco,Eva,SH} = \frac{\dot{m}_{Eco,Eva,SH}}{\dot{m}_{SG}} \qquad (60)$$

increases because the vapour pressure decreases, and the relative heat input required to evaporate the feed water

$$\dot{Q}_{vap,rel} = \frac{\dot{m}_{Eco,Eva,SH}\Delta h_{vap}}{\dot{Q}_{SG}} \qquad (61)$$

is therefore higher. This is why the gradient of the salt mass flow into the Eco, Eva, and SH, over the PB load, is lower than that of the SG salt mass flow. Both are shown in Figure 21.

3.2.6 Pseudo-transient behavior of the power block

The transient behavior of the PB is not modelled as much detail, as that of the SF, described in Chapter 3.1.8. Instead of modelling full transient behavior, the model assumes a pseudo-transient one. An energy state of the PB (Q_{PB}) is therefore introduced that models the current energy stored in the power block.

$$\Delta Q_{PB,th}(t = t_1 - t_0) = \int_{t_0}^{t_1} \dot{Q}_{PB,th}dt \approx \sum_{j=1}^{n} \dot{Q}_{PB,th,j}\Delta t_k \qquad (62)$$

Eq. (62) takes the thermal energy flow into the PB ($\dot{Q}_{PB,th,j}$) at a specific time instant (k) with the time series time step (Δt_k) in account.

All component masses in the PB ($n \cdot m_j$), e.g. the water, the steel masses of the pipes, the heat exchangers, and the turbine, are heated from the start temperature ($T_{j,start-up}$) to average design temperature ($\bar{T}_{j,D}$) during start-up procedure. Therefore the energy

$$\Delta Q_{PB,start-up,real} = \sum_{j=1}^{n} \bar{c}_j m_j (\bar{T}_{j,D} - T_{j,start-up}) \cdot \qquad (63)$$

is stored in the PB. Because this required start-up PB energy is difficult to simulate, the model uses a more simplified ansatz.

$$\Delta Q_{PB,start-up} = \frac{\dot{Q}_{e,PB,D}}{\eta_{net,D}} \cdot \Delta t_{start-up} \tag{64}$$

A start-up time ($\Delta t_{start-up}$) is introduced to estimate the thermal power needed for PB start-up. This time is multiplied by the thermal input of the power block at the design point ($\dot{Q}_{e,PB,D}/\eta_{net,D}$) and is assumed to be from 0.5 to 1 hour. This start-up time increases as with PB downtime. Because the literature provides no cool-down data for a PB with a once-through boiler and salt as HTF, the model assumes that PB heat losses during standby operations ($\dot{Q}_{hl,PB,stand-by}$) are 1% of PB thermal energy input during operations at the design point ($\dot{Q}_{th,PB,D}$).

$$\dot{Q}_{hl,PB,stand-by} \approx 0.01 \cdot \dot{Q}_{th,PB,D} \tag{65}$$

During PB standby mode, a salt mass flow corresponding to $\dot{Q}_{hl,PB,stand-by}$ passes through the SG, and as a result, the start-up time ($\Delta t_{start-up}$) is assumed to be constant. The PB start-up state

$$\tau_{PB} = \frac{\Delta Q_{PB}(t)}{\Delta Q_{PB,start-up}} \tag{66}$$

can be calculated by combining Eqs (64), and (62), and is between 0, or unheated, and 1, or ready for energy production.

Besides the PB thermal inertia, the start-up process is also delayed due the mass inertia of the steam turbine. High temperature gradients are also to be avoided to reduce thermal strain, so the speed of the heating process is limited. To account for these factors, the simulation introduces the ramp-up factor (r) with the unit [kg/s/s]. This factor allows the mass flow into the PB at a given time

$$\dot{m}_{PB}(t) = \dot{m}_{PB,30\%-load} + r(t - t_0) \approx \dot{m}_{PB,30\%-load} + \sum_{j=0}^{(n-1)} r \frac{(2j+1) \cdot \Delta t_k}{2} \tag{67}$$

to be calculated using the mass flow into the SG at 30% PB load ($\dot{m}_{PB,30\%-load}$) and the beginning time of the start-up (t_0).

Figure 22 shows an example of the modelled pseudo-transient PB behavior located in Las Vegas on the January 1, 2008, simulated in ten-minute resolution.
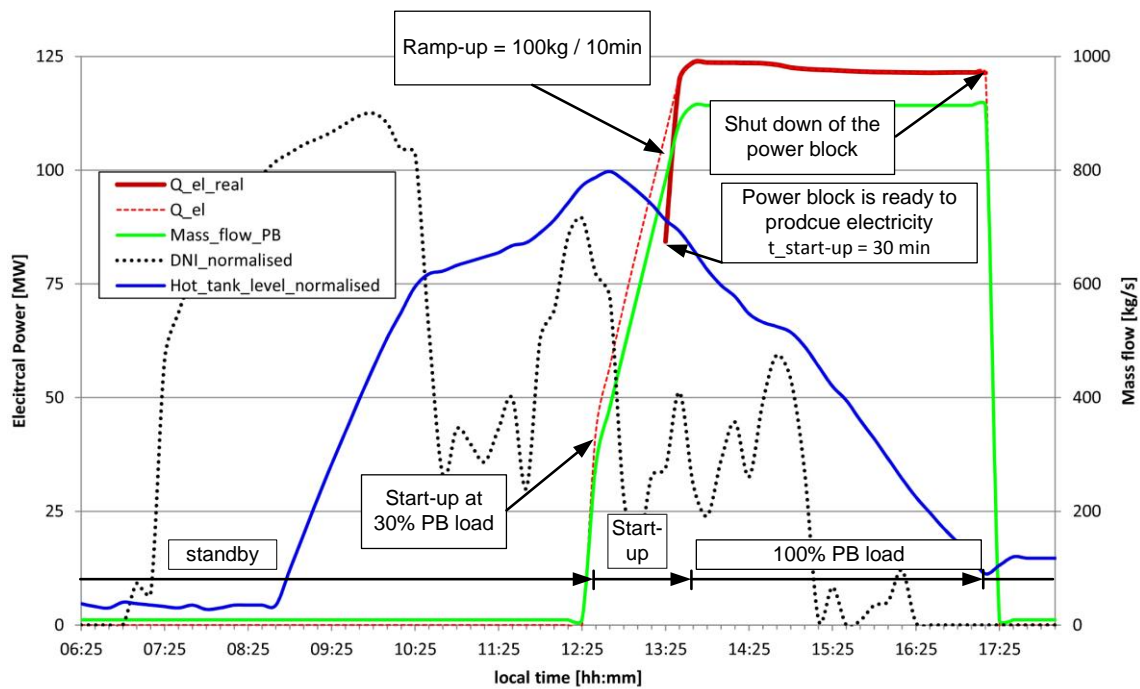
Figure 22: Simulated start-up procedure of the power block from 30% load (37.5 MW$_e$) to 100% load (125 MW$_e$) in ten-minute resolution in Las Vegas on January 1, 2008

After reaching a specific hot tank level at 12:35, the PB starts to operate at 30% load. The mass flow into the SG increases linearly by the ramp-up factor until it reaches 100% of PB load, or 125 MW$_e$. Then the PB operates in quasi-stationary mode at 100% load. The load is slightly reduced until shut-down at 17:15 due to hot tank cool-down. The dashed red line corresponds to the simulated output of electric energy. The continuous dark red line corresponds to the real electric output calculated from the state of the power block given by Eq. (66). Between 13:25 to 13:35, the PB start-up state (τ_{PB}) reaches 1. Note that the excess thermal energy at this time instant is counted against electrical output, so reduced electrical output is plotted starting at 13:25.

3.3 Plant operation management

The simulation model consists of three separate units:

- The solar field, shown in Figure 6 and examined in Chapter 3.1
- The auxiliary heater, shown in Figure 13 and examined in Chapter 3.1.7
- The power block, shown in Figure 17 and examined in Chapter 3.2

Because of the SF's ability to operate in stationary or transient mode, twelve different possible solar thermal power plant operation modes are possible, all shown in Table 11. The Ebsilon model uses eight of them, listed in Table 11 as profiles (P) 1 to 8. It neglects the other four possibilities because they require a more detailed plant operation strategy, e.g supporting the SF during start-up with hot HTF from the AH (profile XX0), producing hot HTF with the AH during nighttime and operating the PB in low off-design mode (0XX), or a combination of both (XXX).

Before the model simulates a given time instant, the EbsScript schematically shown in Appendix G selects a profile. Each profile imports various process

Table 11: Solar thermal power plant operation mode possibilities and the implemented profiles (P)

Steady state of the PTCs

P	SF	AH	PB	Description
1	X	0	X	stationary SF and PB operation, AH is off
2	X	0	0	Stationary SF operation, PB is on standby, AH is off
3	0	0	X	SF is on standby, stationary PB operation, AH is off
4	0	0	0	SF and PB are on standby, AH is off
5	0	X	0	SF and PB are on standby, AH supports HT
n/a	X	X	0	Stationary SF operation, PB is on standby, AH supports SF, HT, or both
n/a	0	X	X	SF is in standby, PB operates stationary, AH supports HT
n/a	X	X	X	Stationary SF and PB operation, AH supports SF, HT, or both

Transient state of the the PTCs

P	SF	AH	PB	Description
6	X	0	X	Instationary SF operation, stationary PB operation, AH is off
7	X	0	0	Instationary SF operation, PB is on standby, AH is off
8	X	X	0	Instationary SF operation, PB is on standby, AH supports SF, HT, or both
n/a	X	X	X	Instationary SF operation, stationary PB operation, AH supports SF, HT, or both

parameters into the simulation model. The profile selection process is shown in Appendix J. The first step is determining whether the PTC simulation mode is steady or transient. Then the threshold hot tank level for AH operation is identified according to time of day. During daytime, the SF can operate if a minimum predicted salt mass flow from the SF is secured. This salt mass flow is forecasted with the "Forecast of salt mass flow" module, shown on the left side of the screenshot in Appendix A. The PB is able to operate if the hot tank minimum level is reached. This threshold level changes dynamically each day according to weather conditions. Then the PB operates until an HT threshold level is reached.

Figure 23 shows the schematic of the Ebsilon simulation mode selection. To improve simulation speed, the model uses two separate instationary units:

- The four PTCs (IS1, IS2, IS3, IS4 in Figure 6), named C unit
- The header and feeder pipelines (IS5, IS6, IS7 in Figure 6), named H-F unit

These two instationary units can change the simulation mode from steady to transient or vice versa. If the C unit simulation mode is transient, the H-F unit simulation mode is also transient. The thermal state of the header and feeders is therefore only assumed to be steady if the SF operation is also steady. A transient simulation starts at sunrise. This process is marked red in Figure 23. The C unit is transient until the HTF temperature after the H2 component, shown in Figure 6, is above hot tank design temperature, or until the HTF temperature is below the lowest HTF temperature during nighttime circulation and the sun has set. This occurs when there is not enough solar radiation to start-up the SF during daytime. Transient processes during daytime, e.g. clouding or end-of-day shut-down, are marked blue in Figure 23. If the SF changes its status from operational to non-operational or vice versa in succeeding time instants, the model initialises a transient simulation which lasts until the hot tank design temperature or the lowest HTF nighttime circulation temperature is reached. The H-F unit is always assumed to be steady when these temperatures are reached after the IS7 component, shown in Figure 6. As shown in Table 11, a profile is considered transient if the instationary unit of the PTC is transient. This is because the numeric controller regulating the SF outlet temperature can only operate during C unit stationary operation.
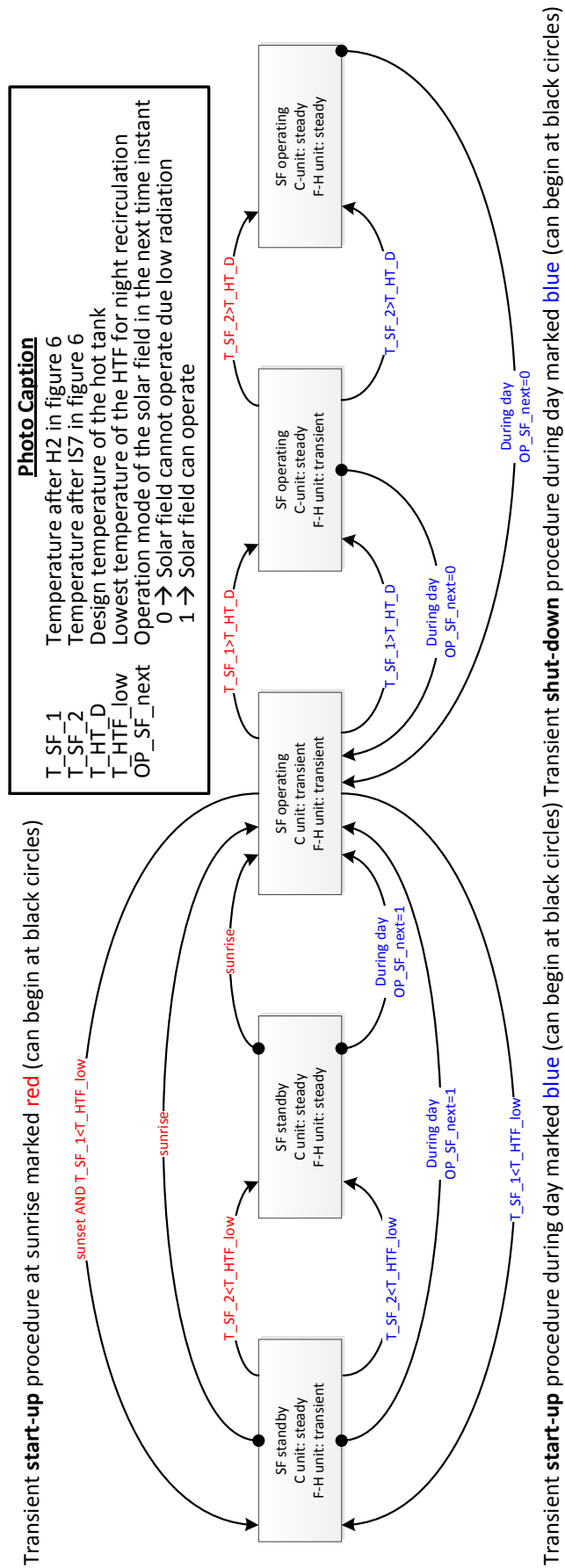
Figure 23: Schematic of the simulation mode selection implemented in Ebsilon

The control of the instationary units is simulated using the Ebsscript shown in Appendix G.

As previously stated, the minimum hot tank level for a given day's PB operations depends on weather conditions. The decision criteria are the day's maximum DNI

$$DNI_{max} = \max(DNI(t)\cos\theta_i(t)) \ , \tag{68}$$

and the day's average DNI.

$$\overline{DNI} = \frac{1}{t_{sunset} - t_{sunrise}} \int_{t_{sunrise}}^{t_{sunset}} DNI(t)\cos\theta_i(t) \tag{69}$$

There are four types of day:

- Very bad day: $DNI_{max} \leq DNI_{min,PB}$ (PB does not start)
- Bad day: $\overline{DNI} \leq \overline{DNI}_{bad\_day}$ (PB starts at $a_{Min\_HT\_level\_bad\_day}$ load)
- Good day: $\overline{DNI}_{bad\_day} < \overline{DNI} < \overline{DNI}_{very\_good\_day}$

    (PB starts at $a_{Min\_HT\_level\_good\_day}$ load)

- Very good day: $\overline{DNI} \geq \overline{DNI}_{very\_good\_day}$

    (PB starts at $a_{Min\_HT\_level\_very\_good\_day}$ load)

For each day, a threshold hot tank level for PB operations is specified. When this level is reached, the PB operates until the hot tank level falls below a threshold level. These plant operation management parameters are listed in the table in Appendix C under "Parameters to identify the weather conditions of a day" and "Parameters to identify whether power block can operate".

Another profile changes is hot tank load during transient processes. During start-up or shut-down, the HTF is recirculated over the recirculation loop shown in Figure 6. If the HTF has reached a specific upper temperature before component S3, shown in Figure 6, it is pumped into the hot tank, as shown in Figure 15. During start-up, the cold tank temperature (the dark blue line in Figure 15) rises until the hot HTF is pumped into the hot tank.

To prevent the HTF from solidifying in the SF, it is pumped via the recirculation loop shown in Figure 6 during night operation, taking advantage of the thermal energy stored in the cold tank during shut-down. If the cold tank temperature falls below design temperature, HTF from the hot tank is pumped through the cold tank support loop shown in Figure 6. If the hot tank falls below a critical load level, the AH is activated to support it. HTF from the cold tank is pumped to the AH, heated, and pumped via the hot tank support loop, shown in Figure 6, to the hot tank in order to raise its level.

3.4 Calculation procedure of the levelized electric costs

To compare the simulated solar thermal power plant with other configurations, the levelized electric costs (LECs) are calculated according to the "Guidelines for the economic analysis of renewable energy technology applications" (International Energy Agency 1991, p. 90ff). Figure 24 shows the calculation procedure. First the Ebsscript "Design power plant", shown in Appendix F, calculates the characteristic parameters of the PB, such as the total SF gross aperture area ($A_{Ape,SF}$), the total PP area (A_{PP}) and the tank thermal capacity (Q_{tank}), according to the user input parameters. The power plant annual yield calculation for a characteristic year reveal the annual net electric output of the power plant ($Q_{e,net,year}$) and the annual thermal energy input of the gas ($Q_{AH,year}$). These parameters and the design gross electrical output ($\dot{Q}_{e,PB,D}$, a user input parameter) allow calculation of the LECs in €/kWh$_e$ using the economic and statistical model presented in this chapter.

3.4.1 Economic model

The LEC is the ratio of all costs the power plant generates during one year to its annual net electric output. These costs are the annual cost for gas (G_0), insurance (INS_0), and operation and maintenance (OM_0). The total investment cost (I) at the beginning of the project, the year zero, is multiplied by the capital recovery factor (CRF) in order to convert it into an annual value over the project lifetime. The
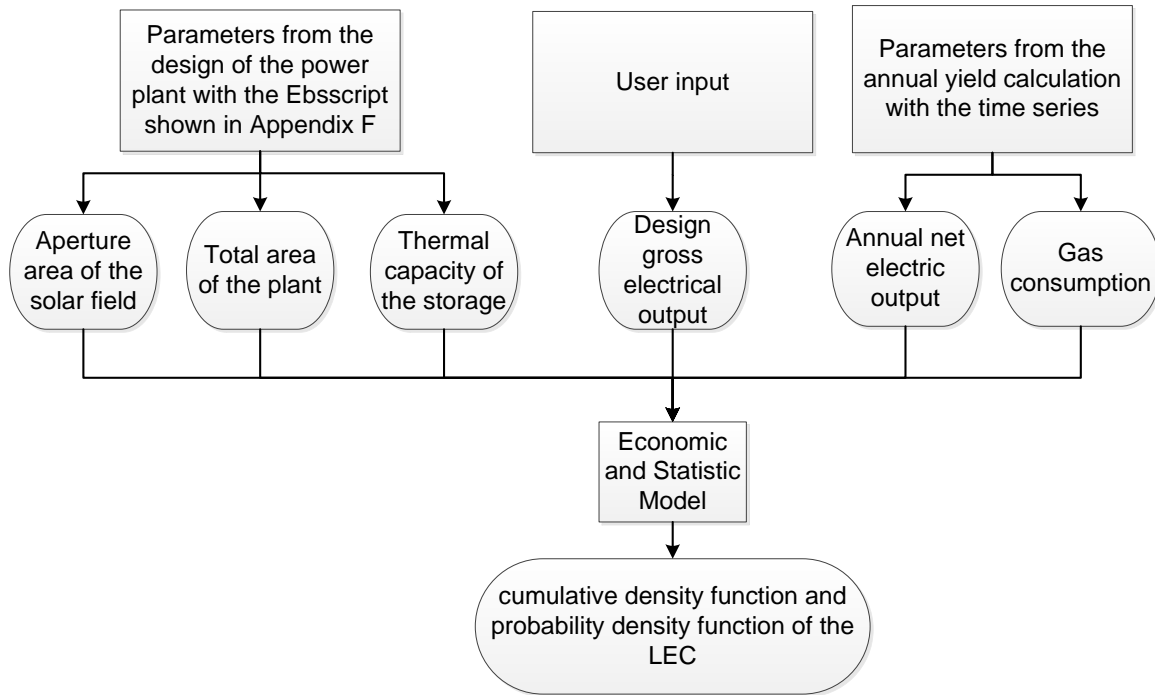
Figure 24: Schematic of the economic model to calculate the levelized electric costs

$$LEC = \frac{I \cdot CRF + OM_0 + INS_0 + G_0}{Q_{el,net,year}} \tag{70}$$

is calculated by combining Eqs (70)(71), (72), (73), (74), (75), and (76). The cost for gas

$$G_0 = \frac{Q_{AH,year}}{\eta_{AH}} P_{gas} \tag{71}$$

is calculated using the annual thermal energy input of the gas, the efficiency of the AH, and the cost of the gas (P_{gas}) in €/MWh_{th}. The cost of insurance

$$INS_0 = I a_{Insurance} \tag{72}$$

is calculated using the total investment cost and the factor $a_{Insurance}$. The operation and maintenance costs

$$OM_0 = a_{OM} \left((n_{em} + n_{em,SF}) P_{em} + P_{water} Q_{e,net,year} + I a_{equipment} \right) \tag{73}$$

cover costs for staff, water consumption and treatment, and equipment. A fixed number of employees (n_{em}) for the BOP and a number of employees for SF maintenance

$$n_{em,SF} = a_{SF,maintance} A_{Ape,SF} \quad , \tag{74}$$

that depends on the total gross aperture area of the SF, and the factor $a_{SF,maintance}$ in 1/1000m², is multiplied by the cost per employee (P_{em}) in €/a. The cost of water consumption and treatment depends on the specific water consumption costs (P_{water}) in €/MWh$_{el}$ and on the net electric output of the power plant. The cost for equipment depends on the total investment cost and the factor $a_{euipment}$. The annual OM factor (a_{OM}) allows adjustment of operation and maintenance costs because of regional differences, for example.

The total investment cost is the sum of costs for the power block (P_{PB}) in €/kW$_e$, SF (P_{SF}) in €/m², storage system (P_S) in €/kWh$_{th}$, land P_{land} in €/m², and indirect costs of construction, calculated using the factor $a_{indirect}$.

$$I = (1 + a_{indirect})(P_{PB}\dot{Q}_{e,PB,D} + P_{SF}A_{Ape,SF} + P_S Q_{tank} + P_{land}A_{PP}) \tag{75}$$

To convert the total investment cost into an annual value over the project lifetime, the capital recovery factor

$$CRF = \frac{a_{dis}(1 + a_{dis})^n}{(1 + a_{dis})^n - 1} \tag{76}$$

is calculated using the project lifetime (n) and the real discount rate of the project (a_{dis}).

3.4.2 Statistical model

As stated in Chapter 2.6, no commercial PTC power plant with molten salt as HTF is in operation, and only research and development projects have been carried out so far. For this reason, no exact data about the specific cost, e.g. the cost of the SF or storage system, is available. Many external parameters such as regional, political, or financial considerations, also influence the LECs. The LECs are therefore to be understood as estimates.

To account for all these uncertainties, the Matlab script shown in Appendix K calculates the LECs using a Monte Carlo simulation based on a random sampling of input parameters $a_1, a_2, \dots, a_j$ into a function $X(a_1, a_2, \dots, a_j)$. In the specific case

of the economic analysis, the parameter X corresponds to the LECs and the parameters a_j to the input parameters in the economic model. Before each simulation, the input parameters are selected individually according to their predefined probability distribution. Then the function X is calculated. Repeating this process for several iterations provides a distribution function of the value X, which is equal to the probability of a range of values. The accuracy of this simulation depends on the number of simulation iterations and the number of input parameters. Therefore only parameters with appreciable effect on X are taken in account. The cost for land, for example, is assumed to be constant because its effect is negligible.

To specify the probability distribution of the input parameters, the continuous uniform distribution and normal distribution are selected. The continuous uniform distribution is a distribution of values between a minimum and maximum value. Each number in this interval is equally probable. This function is selected when no data about probability of a value is available and only the minimum and maximum values can be estimated. This is the case for the cost of SF or the real discount rate of the project, for example. Because no commercial SFs with molten salt as HTF have so far been built, only data about SFs with Thermoliquid as HTF and their minimum and maximum costs are available. The real discount rate depends on the inflation rate, debt interest rate, equity rate, ratio of debt to equity financing, and political grants, so no exact probabilities for this value can be estimated. The normal distribution function

$$P(x, \sigma, \mu) = \frac{1}{\sigma\sqrt{2\pi}}\, e^{-\frac{1}{2}\left(\frac{x-\mu}{\sigma}\right)^2} \tag{77}$$

is used if the a parameter value is relatively fixed and therefore its variation is not as high. The mean value (μ) and the standard deviation of 99% for all values (2.576 σ) are used to calculate the distribution function in equation (80). The PB, for example, is an established conventional technology, and its cost is relatively well-known. The normal distribution is therefore selected.

The probability density function (pdf, $P(x)$) and the cumulative density function (cdf, $f(x)$) are used to visualise the probability of a given parameter. Between the pdf and cdf, the following correlation can be stated (Merziger 2007, p. 197).

$$f(x) = \int_{-\infty}^{x} P(x) \tag{78}$$

According to the central limit theorem (Merziger 2007, p.202), the mean values of n independent and identically distributed input parameters a_j,

$$\bar{a}_{j,n} = \frac{1}{n} \sum_{k=1}^{n} a_{j,k} \tag{79}$$

is normally distributed, as equation (80) shows, and asymptotic for an infinite number of iterations ($n \to \infty$). Each mean value of the parameters a_j is therefore asymptotic, and, as a result, the mean value of the function $X(a_1, a_2, \dots, a_j)$ is also asymptotic. To identify a suitable number of iterations, the residuals of the mean LEC ($\overline{LEC}$) is taken in account. The more Monte Carlo experiments undertaken, the closer $\overline{LEC}$ will approximate its exact value. The residual decreases linearly with the number of experiments. A number of 1,000,000 and therefore residuals of 10^{-7} is assumed to be exact enough.

Because both continuous uniform distributions and normal distributions are used to calculate the LECs, the resulting pdf is not identical to the normal distribution function in equation (77), and therefore the mean, mode, and median LEC value are not necessarily equal.

4   Application of the solar thermal power station model

This chapter investigates the performance of the solar thermal power station model by applying it to a reference plant. It compares quasi-stationary and transient simulations, as well as simulations with four different time steps in the time series calculation, with respect to the reference plant. It also compares the economic performance of the reference plant at three locations with different direct normal irradiation averaged annual sums by calculating the power plant's LECs and presents an improved power plant. Finally, it outlines the economic impact of the cooling method.

4.1   The reference plant

To investigate the performance of the solar thermal power station model, the results of a reference plant are presented in Chapter 4.2. This chapter outlines the reference plant's SF and PB in detail. Las Vegas has been chosen as the reference plant location. The DNI and temperature inputs into the simulation are made from the 2008 Las Vegas solar data set. More details about the location and solar data selection process are found in Appendix M. The parameters used for the reference plant are listed in Appendix L.

4.1.1   Solar field

The solar field's layout is the 2 H layout, which consists of 352 collector loops, each consisting of four Eurotrough ET150 collectors, whose parameters are listed in Appendix H. In all, the gross aperture area is 1.21 km². The solar multiple of the solar thermal power plant, the ratio of thermal power from the SF at the design point ($\dot{Q}_{SF,D}$) to thermal power into the PB at 100% load ($\dot{Q}_{PB,D}$)

$$SM = \frac{\dot{Q}_{SF,D}}{\dot{Q}_{PB,D}}$$

(80)

is assumed to be 2.233. Each storage tank has a capacity of 33,555 metric tons of solar salt and is able to feed the steam generator for 10 hours to produce electricity. The design temperature is assumed to be 510° C for the hot tank and 310° C for the cold tank. During transient start-up or shut-down, the molten salt from the SF is pumped to the hot tank if its temperature is higher than 485° C, and to the cold tank if its temperature is lower. The lowest temperature of the solar salt during night operations is assumed to be 270° C in order to ensure a safety clearance above the molten salt's liquidus temperature (240° C).

The velocity of the HTF in the header and feeder pipes is assumed to be 2.5 m/s, and its heat losses to be 200 W/m. This is equal to 4.0 watts per square meter of aperture area (4.0 W/m_Ape^2). The thickness of the pipes is assumed to be 71 mm, which results in a steel weight of 1,789 t. The HTF mass in the pipes is 3,115 t. The hot tank's heat losses are calculated using Eq. (33) at 1.1 K/d at full tank level.

The solar thermal power plant's design date is assumed to June 21, 2008 with a DNI of 850 W/m² and an ambient temperature of 30° C. Its efficiency on the design date is 67.20%.

4.1.2 Power block

The PB's gross capacity is 125 MW, and the live steam parameters are 500° C and 150 bar. The turbine back-pressure is assumed to be 0.08 bar, which corresponds to wet cooling. The SG's Q,T diagram is shown in Figure 18, and Figure 20 shows the diagram of the feed water heating. Table 10 lists the parameters of the modelled steam turbine. The PB's gross efficiency at the design point is 44.25%, and its net efficiency 43.86%. The PB's off-design behavior is shown in Figure 21. The parameters for the pseudo-transient behavior of the PB, as described in Chapter 3.2.6, are assumed to be 100 kg/s/(600s) for the ramp-up factor, and 0.5 h for the start-up time. An example of the PB's start-up procedure is given in Figure 22.

4.2 Simulation of the reference plant

The solar thermal power station in Las Vegas during 2008 was simulated using the time series dialog within a ten-minute resolution. A ten-second resolution has been chosen for component 119 in order to simulate the transient processes during start-up, shut-down, and periods of low radiation. In all, this results in 52,704 simulations in the time series dialog, lasting for 11.7 hours of wall clock time at common work station. During the simulation, 16 errors occurred, and 1,743 simulations did not converge to the desired residuals of 10^{-7}. The numerical accuracy, plant operation management, and the results of the simulation are presented in this chapter.

4.2.1 Numerical accuracy

As stated in Eq.(43), the discretization of component 119 in the x-direction has been chosen, so that the maximum Courant number is less than one. The maximal Courant numbers can be observed when the mass flow into the SF is maximal. They are 0.32 for the PTCs, 0.75 for the header, 0.51 for feeder 2, and 0.88 for feeder 1. For the summer period of the simulated year, involving high mass flows into the SF and high temperature gradients due to high radiation, numerical errors occur during the simulation. A simulation check is therefore implemented into the simulation model, as shown in Appendix G. The check first changes the mass flow into the SF, changing the Courant number, and re-simulates the time instant. If the numerical error still appears, the simulation mode of the instationary component that causes the error is set from transient to stationary. This simulation check was carried out 224 times during the simulated year, which represents 0.4% of the total instants of time. Each simulation check causes a dumping of thermal energy stored in the HTF and steel mass of the instationary component, which results in an additional thermal loss, as stated in Figure 26 (heat loss switch steady-->transient). That loss is 8 GWh, or 0.26% of solar heat input.

Thermal loss can also be observed during SF shut-down. The HTF's temperature in the SF ($T_{HTF}(t)$) falls from the temperature at the first instationary iteration step

$(T_{HTF}(t_0) =510°$ C) to its lowest temperature during nighttime operations $(T_{HTF,low} =270°$ C) within an exponential function

$$T_{HTF}(t) = T_{HTF}(t_0) - \left(T_{HTF}(t_0) - T_{HTF,low}\right)e^{-\frac{t-t_0}{a_{\Delta t}}} \ , \tag{81}$$

where the factor $a_{\Delta t}$ is about 60 minutes. This causes very long shut-down procedures, long transient calculations, and therefore long simulation wall clock time. To avoid this, the instationary process is stopped if the HTF reaches the temperature $T_{HTF,low} + 2° C = 272° C$, causing an additional dumping of energy.

$$Q_{loss,IS} = \sum_j m_j \bar{c}_j \cdot 2° C \quad , j = IS1, IS2, IS3, IS4, IS5, IS6, IS7 \tag{82}$$

To obtain more precise results, the whole year can be calculated in transient mode by setting the factor $a_{\text{Forecast\_Timesteps}}$ in the implemented user interface to one, which results in very long simulation wall clock times (up to ten times longer). The error in Eq. (82) is 8.2 GWh. As shown in Figure 26, the total error of the indirect storage components $(Q_{loss,IS,total})$, from Eq. (82) and the simulation check, is 16.2 GWh, or 0.5% of the total solar energy input. It can be credited as additional SF heat loss, or in a first approximation as additional PB electric output.

$$Q_{e,,corrected,j} = Q_{e,j} + Q_{loss,IS,total}\eta_{PB,j} \quad j = gross, net \ , \tag{83}$$

As previously stated, the most unstable part of the simulation is the transient system behavior of the SF during high temperature gradients, e.g. during SF start-up. The simulation also did not converge to the desired residuals of 10^{-7} for 3.3% of all performed simulations, mostly during instationary operations. To investigate the numerical error over the entire simulated year, the SF energy conservation is modelled as shown in Figure 26. The SF's energy output is calculated using Eqs (84) and (85). Eq. (84) uses the heat flow of the sun $(\dot{Q}_{sun})$, PTC optical loss $(\dot{Q}_{loss,PTC})$, PTR thermal loss $(\dot{Q}_{loss,PTR})$, piping thermal loss $(\dot{Q}_{loss,piping})$, and indirect storage thermal loss $(\dot{Q}_{loss,IS})$ for each time step (j) with a time interval of ten minutes $(\Delta t = 600s)$ to calculate the SF's total energy output

$(Q_{SF,1},\ Q_{SF,2})$. Eq. (85) uses the energy flow into the SF system $(\dot{Q}_{M1})$ and out of the system $(\dot{Q}_{S3})$, where S3 and M1 refer to the components in Figure 6.

$$Q_{SF,1} = \Delta t \sum_{n=1}^{52,704} \dot{Q}_{j,sun} - \dot{Q}_{j,loss,PTC} - \dot{Q}_{j,loss,PTR} - \dot{Q}_{j,loss,piping} - \dot{Q}_{j,loss,IS} \qquad (84)$$

$$Q_{SF,2} = \Delta t \sum_{n=1}^{52,704} \dot{Q}_{j,S3} - \dot{Q}_{j,M1} = \Delta t \sum_{n=1}^{52,704} \dot{Q}_{j,SF} \qquad (85)$$

As shown in Figure 26, the numerical error is 0.7 GWh, calculated by subtracting Eq. (84) from Eq. (85). This corresponds with 10^{-5} over the entire year and is smaller than the maximum possible residuals, assuming residuals of 10^{-7} for all 52,704 simulated instants of time.

$$10^{-7} \cdot 5.2704 \cdot 10^4 \approx 10^{-3} \qquad (86)$$

The first two result value figures can therefore be said to be numerically exact, considering the worst case in Eq. (86), up to four, considering the tested case in Eq. (84) and (85).

4.2.2 Plant operation management

The plant operation management strategy, described in Chapter 3.3, is based on each day's weather classification, as shown in Figure 25 a). Seven very bad days with a maximum DNI of less than 300 W/m² occurred. During these days, the PB did not start at all. In all, the PB did not operate on 31 days, which means that on 24 bad days, with an average DNI as high as 500 W/m², the 30% threshold level of the hot tank was not reached. The solar heat input was stored in the hot tank and used to maintain the SF's temperature or to feed the SG on the next day. On 335 days, the PB was able to operate. The PB operation threshold level was set to 10% for good days (average DNI from 500 to 800 W/m²) and 4% for very good days (average DNI higher than 800 W/m²). In all, the PB carried out 338 start-up processes, as described in Chapter 3.2.6. This means that on three days, the PB had to start-up a second time because the hot tank threshold level

(4% load) was reached within the day. On these days, the PB was heated twice, resulting in higher energy input for heating and more time in off-design mode.

The PTCs were defocused for 14.96% of the SF operation time. That means that thermal energy of the sun was dumped by setting the focus factor in Eq. (11) to a value in between 0 to 1. This happened on 145 days between March 18 and September 24, most of which are during summer. The PTCs remained defocused on 28 good days.

The ideal operation management strategy would prevent more than one PB start-up process per day, setting the hot tank threshold level to the correct load level. But late PB start-ups during days of high solar radiation, resulting in solar power dumping by defocusing the PTCs, must also be prevented. As outlined, this happened on 28 good days (threshold level of 10% load) during the 2008 Las Vegas simulation. The operation management strategy therefore has the potential to improve with the optimization of the parameters $DNI_{bad\ day}$, $DNI_{very\ good\ day}$, and $a_{Min\_HT\_level}$. But a perfect operation management strategy is not realistic because during real-life power plant operations, a late or early PB start-up, resulting from an inaccurate weather forecast, for example, is also possible.

Figure 25 b) shows the percentages of the selected profiles, as listed in Table 11, during the simulated year. A transient profile, which refers to transient C unit components, was necessary 23% of the total time because of the SF start-up process (mode 1, 42% of transient simulation), and shut-down or clouding
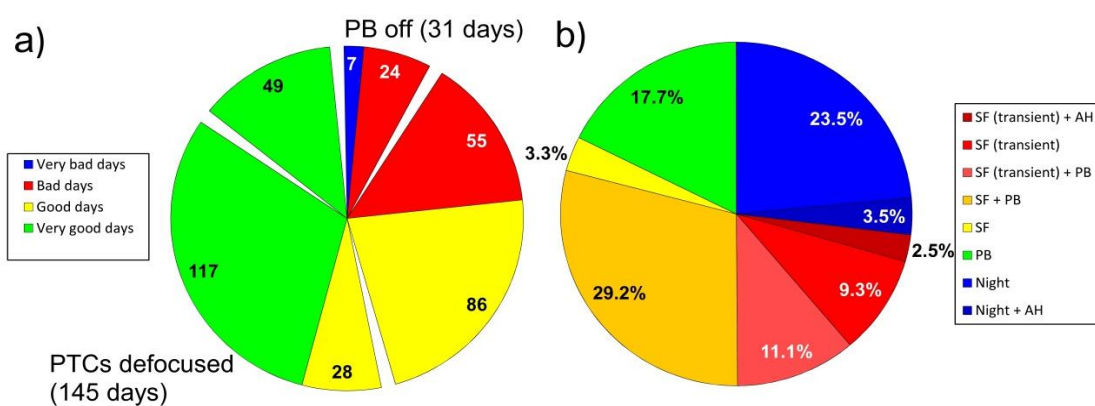
Figure 25: Classification of 2008 in Las Vegas in a) weather conditions and b) selected profiles

(mode 2, 58%). The F-H unit was in transient mode for 31% of the total time. Only during time instants with high temperature gradients in the SF was a transient simulation selected, which resulted in 69% of quasi-stationary simulations over the entire simulated year. During 3.3% of the year, only the SF was operating in quasi-stationary mode, a condition which is attributable morning operations, when the hot tank threshold level for PB operations had not yet been reached. In the most commonly used profile, 29.2% of the time, the PB and SF operated in a quasi-stationary manner at the same time. 17.7% of the time, only the PB operated, a condition which is attributable to nighttime periods. In all, the PB is in operational mode during 57.9% of the simulated time. The SF operates 32.4% of the time in quasi-stationary SF mode, a figure which rises to 55.4% if transient modes, e.g. during shut-down, are also included. The nighttime profile, which refers to quasi-stationary operations during nighttime, was used 27% of the simulated time. During these times, the PB is in standby mode, and HTF from the cold tank is pumped through the SF, reaching the lowest HTF temperature (270° C) at its end. If the cold tank's thermal energy is consumed and the hot tank reaches its threshold limit for AH operations, the AH is activated. This happened 6% of the time.

4.2.3 Results

In order to investigate the solar thermal power plant's energy flow for one year, three systems have been chosen. The first system is the SF, between components M1 and S3, shown in Figure 6. The second system is the AH and the cold and hot tanks, between components M1, S3, S4, and M4, also shown in Figure 6. The third system is the PB, the rest of the power plant. These systems and their energy flows are shown in Figure 26. The first two systems are transient, and therefore their energies are not constant over time ($dQ/dt \neq 0$). At the beginning and at the end of the time series, the SF is in quasi-stationary mode, so the energy stored in this system over the year is zero ($\Delta Q/\Delta a = 0$). The hot and cold tanks' temperatures, as well as their loads, are not equal at the beginning and at the end of one year, which results in a change of system energy ($\Delta Q/\Delta a = 0.011$ GWh). Because this difference is very low, it is neglected in Figure 26.

By reducing the three systems to one simple system, the entire power plant, following inputs can be specified:

- 3057.2 GWh thermal power from the sun
- 45.2 GWh thermal power from gas
- 24.8 GWh electric power input to operate the pumps in the SF and PB

The outputs of the whole systems are:

- 2513.3 GWh losses (optical, thermal)
- 16.9 GWh simulation error as described in Chapter 4.2.1
- 596.0 GWh electric power

The power plant's gross efficiency is therefore calculated at 19.2%, and its net efficiency at 18.4%. The gross optical performance of the PTCs is 60.5%, accounting for PTC optical loss, while the net performance is 55.9%, calculated by including dumping losses. The SF's gross efficiency is 44.9% and nearly equal to the net efficiency, accounting for the electric power consumed by the SF pumps. The major heat loss is caused by the PTRs (72.3%), followed by the power block heat-up (11.9%), pipings (6.3%), simulation error (4.0%), PB standby (2.4%), tank (2.0%), and the AH (1.1%). The AH co-firing (45.2 GWh) was only used to
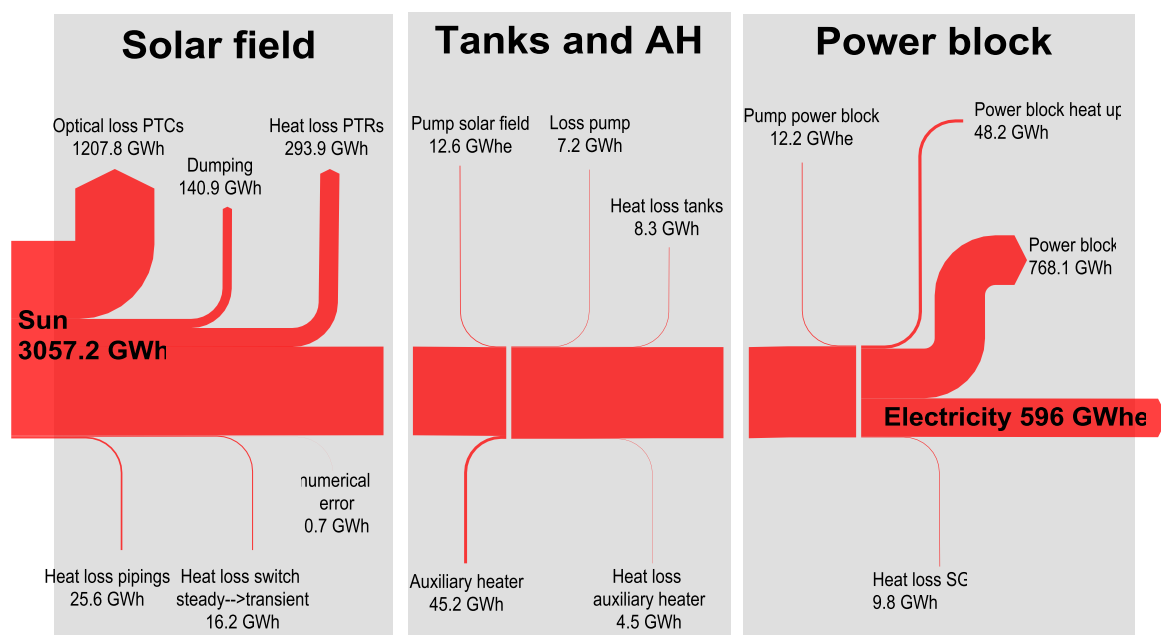
Figure 26: Sankey diagram of the reference plant

maintain the SF's temperature and is 3.3% of the SF thermal energy output. As stated in Eq. (65), during PB standby mode, molten salt from the hot tank is used to maintain the SG's temperature. This causes 9.8 GWh of thermal losses. PB heat-up consumes 48.2 GWh of thermal energy. In all, the PB operates at 6.9% in off-design mode, resulting in a gross efficiency of 42.3% and net efficiency of 41.4% over the entire year. The PB electric output is 596 GWh. Further discussion of the economic efficiency and the LECs is found in Chapters 4.5, 4.6, and 4.7.

4.3   Comparison of stationary and transient solar field model

In order to compare the transient and stationary SF simulation model, the reference plant, described in Chapter 4.1, is modified. The value of the two parameters $a_{\mathrm{Mode\_SF}}$ and $a_{\mathrm{Mode\_H}}$, listed in Appendix C, are changed from 1 to 0, which signifies a quasi-stationary simulation. The instationary components IS1, IS2, IS3, IS4, IS5, IS6, and IS7, shown in Figure 6, are therefore deactivated. All other parameters are equal to the reference plant's parameters. The additional indirect storage component heat loss of 16.2GWh, described in Chapter 4.2.1, is added in accordance with Eq. (83) to the PB electric output. Because the models' system behavior differ, their AH heat inputs are not equal. The difference is 7.4 GWh. To compare the two simulations, they must have the same energy input, so the reference energy of the AH ($Q_{AH,ref}$=45 GWh) is introduced. The electric output can therefore be calculated in a first approximation.

$$Q_{e,corrected2,j} = Q_{e,j} + \left(Q_{AH,ref} - Q_{AH}\right)\eta_{PB,j} \quad j = gross, net \qquad (87)$$

Figure 27 shows the comparison of energy flows over the entire simulated year. In this figure, the results of the reference plant energy flows, shown in Figure 26, always refer to 100%. In order to describe the effects causing the two simulations' differing results, one day has been chosen, shown in Figure 28. The hot and cold tank temperatures, as well as the hot tank's load level, are plotted over one day, October 3, 2008, for the transient (continuous line) and the stationary (dashed line) simulation. The temperature of the HTF at the SF outlet, which refers to the temperature past component IS7 in Figure 6, is also plotted for both simulations.

At 5:45, sunrise, both simulations are in start-up mode. Changes in the DNI immediately result in changes in the SF's outlet temperature in the steady simulation. Because the sky is clouded for several hours on this day, which results in high DNI changes, the red dashed SF temperature is discrete, whereas the temperature course of the transient simulation is continuous. SF outlet temperature changes, due to DNI changes, are delayed in the transient simulation because the steel mass is heated, and the HTF's velocity in the pipes is simulated. At 15:05, both models simulate SF shut-down due to low radiation. This shut-down process lasts 30 minutes, until the DNI is zero, in the steady simulation, and 340 minutes in the transient simulation. There are two reasons for this delay. First, the hot HTF from the PTCs is delayed because its velocity in the pipes is reduced during shut-down. Second the heat stored in the 1,789 metric tons of steel pipes is transferred to the HTF. Because of the low mass flow, the heat transfer coefficient is low, which results in a lower HTF temperature gradient than that present during the start-up process. From 16:45 to 16:55, the skies clear, and low normal radiation is plotted in Figure 28. This solar energy is collected by the transient simulation PTCs, whereas the steady simulation is in night operations mode, indicated by a focus factor in Eq. (11) of 0. This solar energy is therefore not collected by the steady PTCs. Over the entire simulated year, this effect results in 0.20% reduced effective solar energy input, as shown in Figure 27.

A major effect is the reduced storage capacity of the steady simulation. Because the headers and feeders are modelled exactly in the transient simulation, the storage capacity is expanded by 1,789 metric tons of steel mass ($s = 4,612$ kJ/m³/K) and 3,115 metric tons of solar salt in the piping elements. Because of the reduced storage capacity, more energy is dumped in the stationary simulation during periods of high radiation. The PTCs are defocused for 16% of SF operations in the steady simulation, whereas the PTCs of the transient simulation are only defocused 15% of the time. This results in an additional 0.62% reduction in energy input to the HTF, as shown in Figure 27.
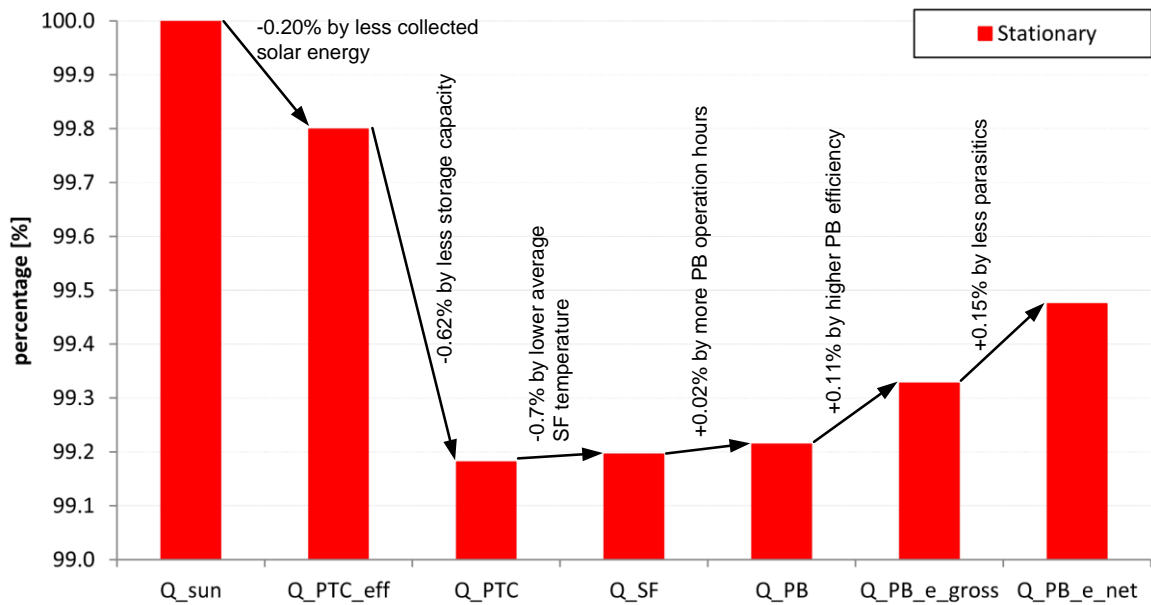
Figure 27: Annual energy comparison for stationary and transient simulation – transient simulation refers to 100%
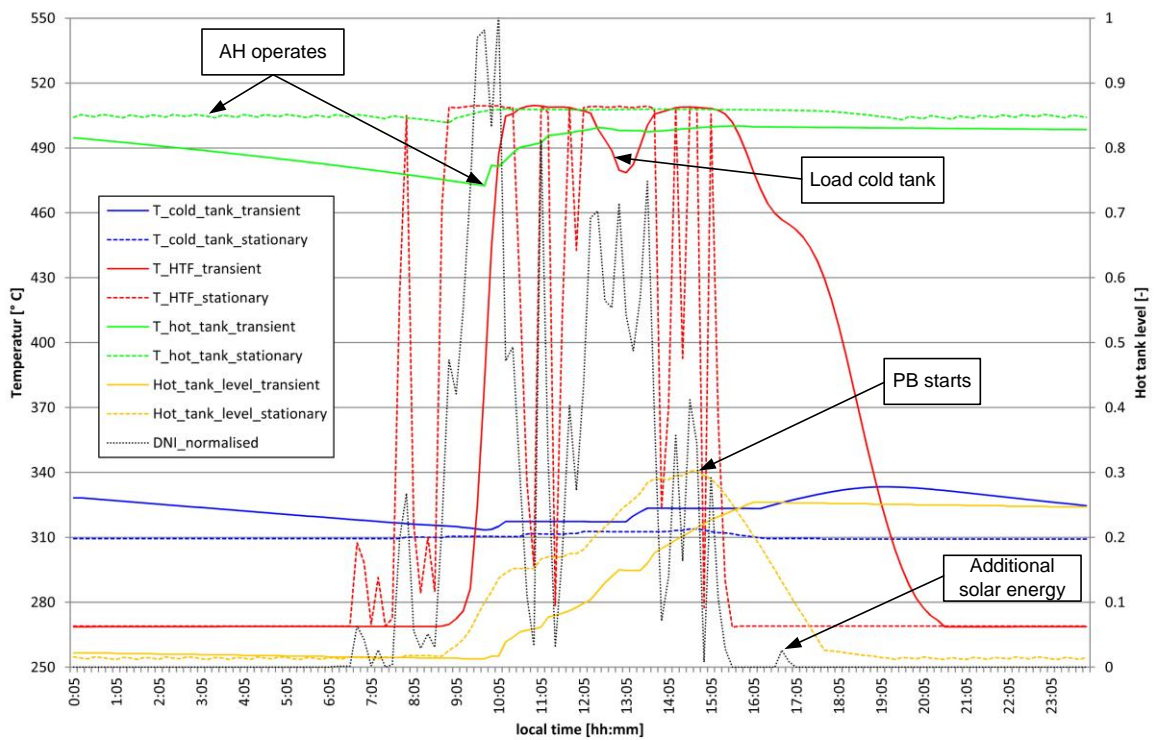
Figure 28: Comparison of stationary and transient simulation on October 3, 2008 in Las Vegas

As previously stated, the start-up and shut-down processes are modelled in detail in the transient simulation. During these processes, the hot HTF at the SF outlet is pumped to the cold tank if its temperature is below 485° C and to the hot tank if it is above. This causes higher temperature gradients in the cold and hot tanks, as shown in Figure 28. The annual average temperature of the hot tank is therefore 0.3% lower than that of the stationary simulation, whereas the temperature of the cold tank is 0.8% higher. This difference in hot and cold tank temperatures has three effects.

First, average SF temperature is higher because the cold tank temperature is higher, which results in 0.7% higher SF heat loss in the transient simulation. The annual energy out of the SF, calculated using Eq. (84), is therefore 0.02% higher in the steady simulation, as shown in Figure 27.

Second, the annual PB efficiency is decreased because the annual mean temperature of the hot tank is lower in the transient simulation. The annual PB efficiency is 40.51% in the transient simulation and 40.61% in the steady simulation. This causes a rise of 0.11% in the annual thermal input into the PB and in the annual PB gross electric output, as shown in Figure 27.

Third, the SF parasitics are reduced by 5.84% in the steady simulation. According to Eq. (3), the velocity of the HTF depends on a temperature rise through a PTC loop. In the transient simulation, the annual mean rise is 194.2° C, and in the steady simulation it is 198.4° C. HTF velocity is therefore lower in the steady simulation, and as a result, the SF pumping parasitics are reduced. This causes a rise of 0.15% to the annual gross and net electric output in Figure 27.

The PB operation hours for the two simulations are different. In the steady simulation, the PB operates three days more than in the transient simulation. This effect can be seen in Figure 28. At 14:45, the threshold level of 30% hot tank load is reached in the steady simulation, and the PB starts to operate. In the transient simulation, the 30% threshold level is not reached because more thermal energy is stored in the cold tank. The energy stored in the hot and cold tanks is used to maintain the SF outlet temperature. On the next day, the hot tank load is used to feed the SG (not shown in Figure 28). But its heat capacity and temperature is

reduced due to tank heat losses during the night. This causes a rise of 0.02% in annual SF energy output and PB energy input in Figure 27.

Because the steady simulation model does not simulate start-up and shut-down, it reflects 4.2% more thermal energy stored to the hot tank, and the AH is therefore activated more often, which results in an increased heat input of 7.4 GWh, as stated at the beginning of this chapter. During the morning hours, the AH is activated every 35 minutes to produce hot HTF, as the dashed green line, the temperature of the hot tank in the steady simulation, shows in Figure 28. The AH is only activated at one time instant, 09:45, in the transient simulation, as indicated in Figure 28.

4.4 Comparison of various time series time steps

In order to compare various time series time steps (TSs) in the time series dialog, the reference plant, described in Chapter 4.1, is modified. The value of the parameter $a_{\text{ts\_tsc}}$, listed in Appendix C, is changed from 600 s to 900 s, 1800 s, and 3600 s, which reflects to different TSs in the time series dialog. All other parameters are equal to the reference plant's parameters.

The Las Vegas solar data in one-minute resolution (527,040 data points) is averaged to 10-, 15-, 30-, and 60-minute resolution in order that the annual thermal input from the sun

$$Q_{DNI}(\Delta t_k) = \Delta t_k \sum_{j=1}^{n=\frac{527,040 \text{ min}}{\Delta t_k}} \dot{Q}_{DNI,j}, \quad \Delta t_k = 1, 10, 15, 30, 60 \text{ min} \tag{88}$$

be equal for each TS (Δt_k). The arithmetic mean DNI at a specific time step (t) for the four different TSs

$$\left(\overline{DNI}\left(t = \frac{\Delta t_k}{2} + j\Delta t_k\right)\right)_{\Delta t_k} = \frac{1 \text{ min}}{\Delta t_k} \sum_{l=j\Delta t_k}^{n=(j+1)\Delta t_k - 1} DNI_l,$$

$$j \epsilon \left[0, \dots, \frac{527,040 \text{ min}}{\Delta t_k}\right[, \quad \Delta t_k = 10, 15, 30, 60 \text{ min} \tag{89}$$

is calculated at the average TS (5, 7.5, 15, and 30 min). The arithmetic mean ambient temperature at a specific time step $\bar{T}_{amb}(t)$ is calculated using Eq. (89), replacing the parameters $\overline{DNI}$ to $\bar{T}_{amb}$, and DNI to T_{amb}.

Figure 29 shows the DNI discretization comparison for three different time steps (10, 30, and 60 minutes), and the original DNI data (1 min.). The time between sunrise at 06:53 and sunset at 16:34 is discretized in 10 time instants (60 min. discretization), 19 time instants (30 min.), 38 time instants (15 min.), 58 time instants (10 min.), and 582 time instants (original solar data). Generally, the maximum number of time instants between sunrise and sunset can be calculated.

$$\left\lceil n_{\Delta t_k, max} \right\rceil = \frac{t_{sunset} - t_{sunrise}}{\Delta t_k}, \quad \Delta t_k = 10, 15, 30, 60 \text{ min} \tag{90}$$

The 60-minute discretisation in Figure 29 shows one time instant at 06:30 with an arithmetic mean DNI, calculated with Eq. (89), higher than zero (0.025 W/m²). The 30-minute discretisation also has one time instant at 6:45 with a mean DNI higher than zero (0.05 W/m²). These instants of time occur before sunrise, and this solar
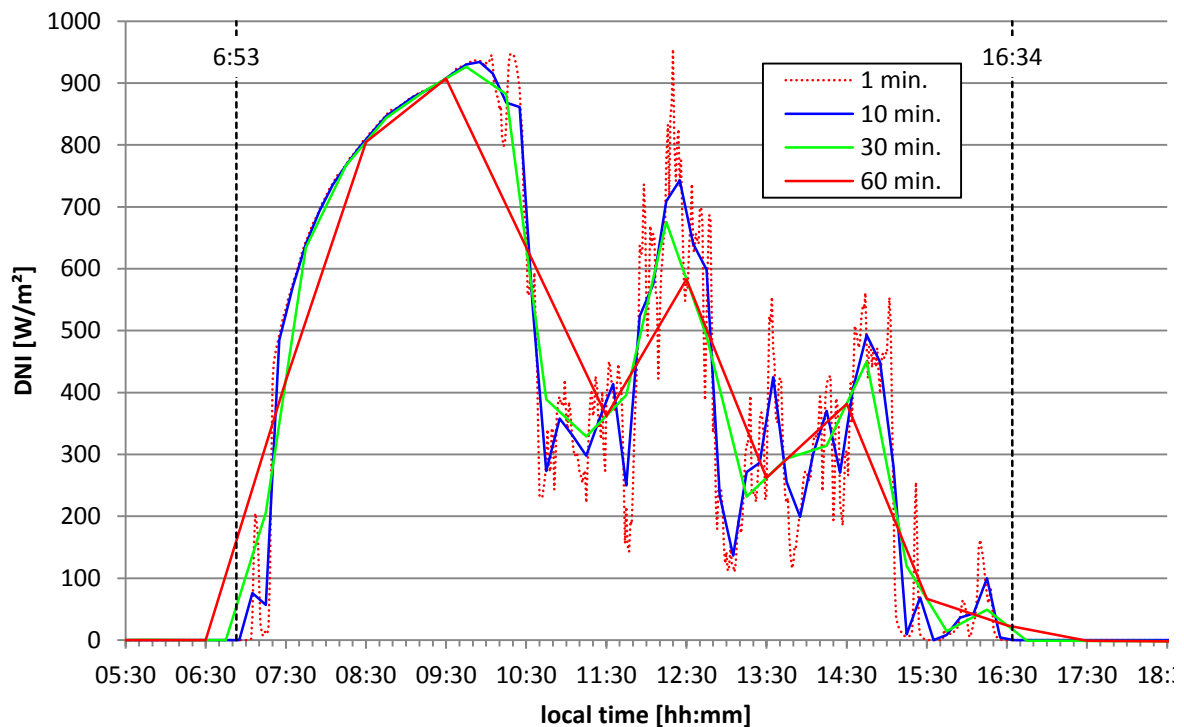
Figure 29: DNI discretization comparison for three different TSs in Las Vegas on January 1, 2008

energy cannot be collected by the PTCs ($\theta_i > 90°$ in Eq.(11)). Therefore the integral of the DNI from sunrise to sunset in the 30- and 60-minute discretisation is less than that in the original data. The probability that less energy is collected is 50% for each discretisation, and the energy loss

$$q_{loss,discretisation} = \overline{DNI}(t) \cdot \Delta t_k, \ \ \Delta t_k = 10, 15, 30, 60 \ \text{min} \tag{91}$$

can be calculated using the arithmetic mean DNI at the time instant before sunrise. The same probability that less energy is collected also occurs after sunset. The higher the discretisation, the higher the arithmetic mean DNI and TS, and the higher the energy loss. The maximum discretisation error is shown in Figure 30 for a summer day. No solar energy is collected during the time interval, which is between zero minutes and

$$\Delta t_{max} = \frac{\Delta t_k}{2}, \ \ \Delta t_k = 10, 15, 30, 60 \ \text{min} \tag{92}$$

minutes. These instants of time ($t_{sunrise} + \Delta t_{max}$) are shown in Figure 30 for the 60-minute discretisation (04:57) and the 30-minute discretisation (04:42). The loss
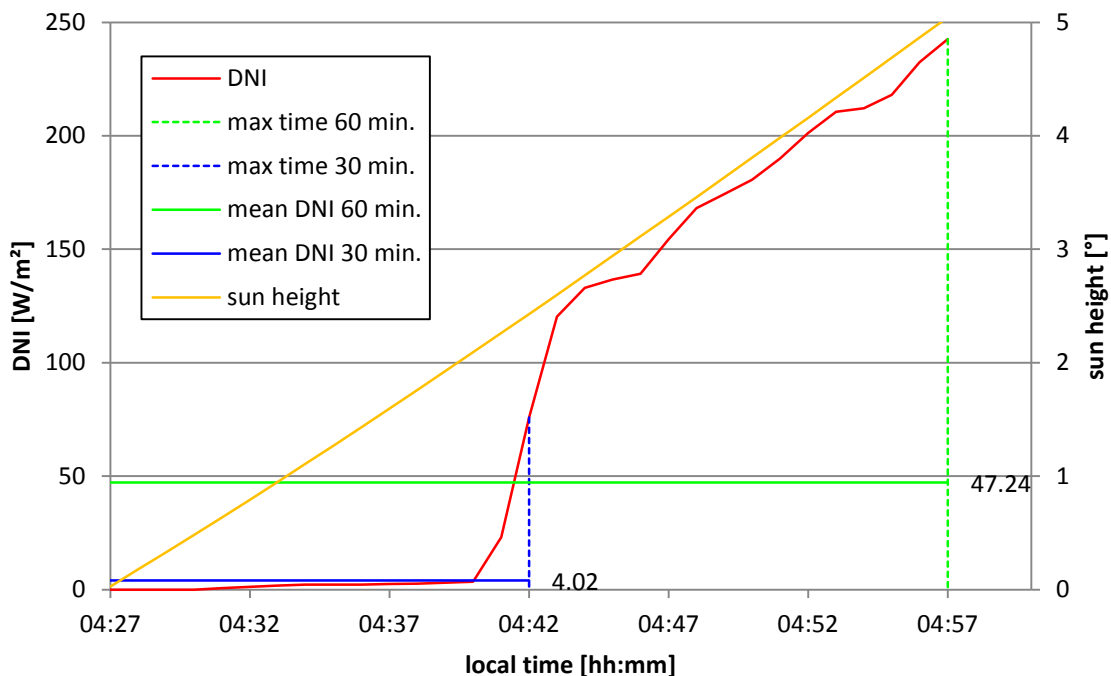
Figure 30: Maximum 60- and 30-minute discretization error due to less collected solar energy than the original 1-minute data, during a summer day

can therefore be calculated using Eq. (91) to be 170 kJ/m² (60-minute discretisation) and 7.2 kJ/m² (30-minute discretisation), which amounts to 0.5% and 0.02%, of the total collected specific energy on this day, respectively. The maximal inaccuracy of the 10- and 15-minute discretisation on this day is factually zero because the DNI at 5 and 7.5 minutes after sunset, respectively, is nearly zero.

In order to compare the results of the four simulations, the reference energy of the AH ($Q_{AH,ref}$=45 GWh) is introduced, as described in Chapter 4.3 and stated in Eq. (87). The AH heat input is 40.7, 40.3, 38.9, and 23.57 GWh (10-, 15-, 30-, and 60- min. discretization).

Figure 31 shows the relative results of the annual energy comparison for the 10-, 15-, 30-, and 60-minute TS, where 100% reflects the reference plant results (10-minute TS), shown in Figure 26. The absolute values are listed in Appendix O. As stated in Eq. (88), the solar energy input is independent from the TS, and therefore remains 100% in each of the four simulations. The effective energy input to the PTCs (Q_PTC_eff), without taking dumping of solar energy into account, is reduced due to the DNI discretisation error, shown in Figure 30, and the PTC efficiency discretisation error, described in Appendix N. It is reduced by 0.03%, 0.13%, and 1.13% (15-, 30-, and 60-min. discretisation). Because the energy input into the PTCs is calculated using the algebraic Eq. (11), no numerical inaccuracy, as described in Chapter 4.2.1, can occur, and therefore the differences are considered to be exact.

The light blue graph (Q_HT/Q_SF) in Figure 31 shows the ratio of annual SF energy stored in the hot tank to the total annual SF output energy, calculated using Eq. (85). The annual energy stored in the hot tank is also calculated with Eq. (85), but totals only the energy flows into the hot tank. This ratio is 102.51% in the reference plant, which means that the annual SF energy stored in the cold tank is negative (-34.5 GWh). This results from the nighttime HTF recirculation over the SF. The HTF is cooled by the piping element heat losses in the SF and stored back in the cold tank. The ratio Q_HT/Q_SF falls with higher TSs, which means
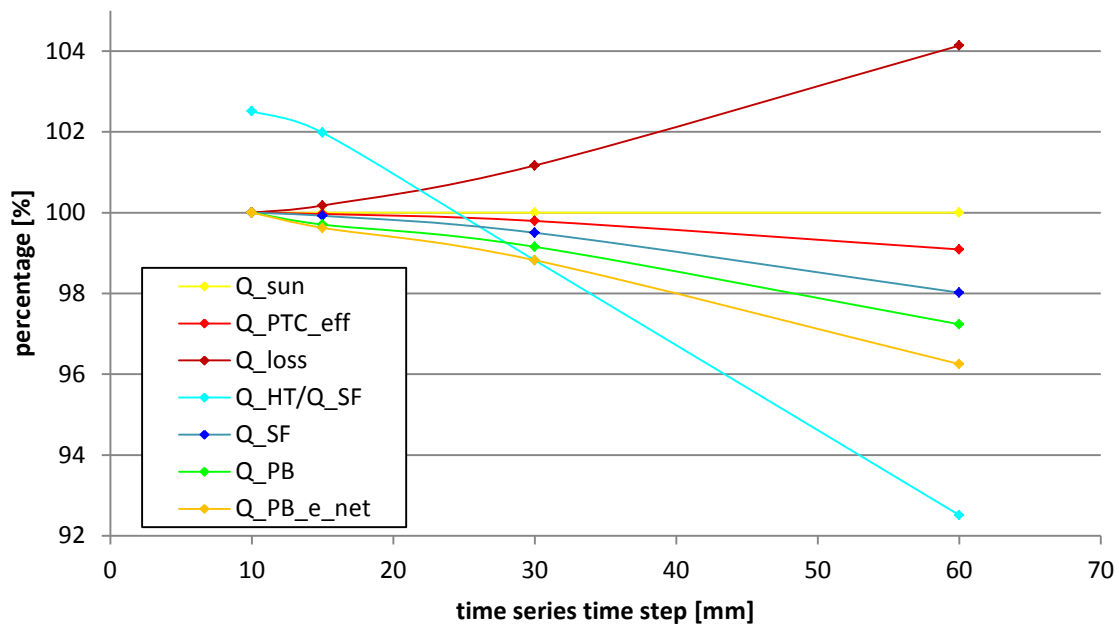
Figure 31: Annual energy comparison for 10-, 15-, 30-, and 60-minute TS – 100% is 10-minute TS

more energy is stored in the cold tank. This results from the simulated start-up and shut-down process. As described in Chapter 3.3, the HTF from the SF is stored in the cold tank if its temperature is lower than $a_{\mathrm{Hot\_Tank\_Low\_Temp}}$ (485° C) and to the hot tank if it is higher. The higher the TS, the more hot HTF is stored in the cold tank. For example, if the SF outlet temperature reaches 484° C at one time instant in the 60-minute discretisation, the hot HTF is stored in the cold tank for one hour.

This results in higher average cold tank and SF temperatures. Therefore the AH heat input decreases with higher TSs, because the cold tank thermal capacity is used to maintain the SF temperature. As described in Chapter 4.3, the heat losses and the SF pumping parasitics also increases with higher cold tank temperatures. The heat losses over the SF, the dark red line in Figure 31, are 0.18%, 1.17%, and 1.17% higher (15-, 30-, and 60-min. discretisation). Because of this, the difference between the annual effective PTC energy (Q_PTC_eff) and annual SF energy output (Q_SF) in Figure 31 decreases with higher TSs. The SF pumping parasitics are increased by 0.7%, 4.7%, and 7.9% (15-, 30-, and 60-min. discretisation).

Because less energy is stored in the hot tank, the annual average hot tank temperature also decreases, which results in lower PB net efficiency. It is 42.27%,

42.25%, 42.19%, and 42.07% (10-, 15-, 30-, and 60-min. discretisation). It also decreases because the pseudo-transient PB start-up process becomes longer with higher TSs. The PB start-up process lasts about 50 minutes and cannot be simulated properly using high TSs. Therefore the PB time in off-design is 6.9%, 7.3%, 8.1%, and 14.3% (10-, 15-, 30-, and 60-min. discretisation) and increases with higher TSs. The increased SF parasitics, and the lower PB efficiency explain the difference between annual PB heat input (Q_PB) and annual net electric output (Q_PB_e_net) in Figure 31.

A difference between the blue line (Q_SF) and the green line (Q_PB) can also be observed in Figure 31. This is because of the different PB operation hours. The PB operates during 57.9%, 57.7%, 57.0%, and 56.1% (10-, 15-, 30-, and 60-min. discretisation) of the total year, which results in 335, 333, 332, and 327 days (10-, 15-, 30-, and 60-min. discretisation) of operation. On bad days, described in Chapter 3.3, the threshold level of the hot tank for PB operations is not reached when high TSs are used. This causes lower PB operations hours, as described in Chapter 4.3.

In all, the net electric output of the PB decreases with increasing TSs. It is by -0.38%, -1.18%, and -3.75% (15-, 30-, and 60-minute discretisation) than that of the reference plant's electric output.

4.5 Comparison of three years with different direct normal irradiation averaged annual sum

To compare three years with different direct normal irradiation averaged annual sums, the reference plant, described in Chapter 4.1, is modified. The value of the parameter a_{Location}, listed in Appendix C, is changed from 1, or Las Vegas, to 2, or Almería. The latitude, longitude, and time zone of the sun element (component 117), are therefore changed from 36.06°, -115.08°, and Pacific Standard Time to 37.09°, 2.36°, and Central European Standard Time. All other parameters remain equal to the reference plant's parameters. The 2008 Las Vegas DNI and ambient temperature in the time series dialog inputs are changed to the 2010 and 2005 inputs, respectively. The direct normal irradiation averaged

annual sum is 2095 kWh/m²/y in Almería during 2010, 2300 kWh/m²/y in Almería during 2005, and 2659 kWh/m²/y in Las Vegas during 2010. Appendix M contains further discussions of these locations.

In order to compare the results of the three simulations, the model introduces reference AH energy ($Q_{AH,ref}$=45 GWh$_{th}$), as described in Chapter 4.3 and calculated using Eq. (87). The AH heat input is 40.7, 48.0, and 48.1 GWh (Las Vegas 2008, Almería 2005, and Almería 2010).

The economic and statistical model, as described in Chapter 3.4, is used to calculate the LECs of the three simulations. The economic model input parameters, and the employed distributions for those parameters, are listed in Appendix L under "Economic parameters". The design input parameters are the thermal capacity of the storage (2,7436,049 kWh$_{th}$), the aperture area (1.21 km²), the total area of the plant (4.25 km²), and the design power block electric output (125,000 kWh$_e$). These parameters are similar for all three simulations. The result of the simulation, the PB annual net electric output, is 572.0 MWh, 490.4 MWh, and 447.0 MWh (Las Vegas 2008, Almería 2010, and Almería 2005). The Sankey diagrams with the absolute energy flow values for the Almería 2010 and 2005 simulations can be found in Appendix P.

Figure 32 a) shows the pdf for the three simulations and for the improved power plant, described in Chapter 4.6. Figure 32 b) shows the cdf for these simulations. As stated in Eq. (78), the integral of the pdf results in the cdf. The mean value, according to Eq. (79), is plotted as a dashed line in the corresponding colour for the four simulations. The mode value is also indicated in both figures with a hash key in the corresponding colour. The mean, mode, and median LEC value for each simulation is not equal, as described in Chapter 3.4.2. The mean LEC result from the mean input parameters ($a_{Insurenace} = 0.003$, $a_{equipment} = 0.0125$, $a_{indirect} = 0.25$, $P_{PB} = 720$ €/kWh$_e$, P_{SF} =275 €/m², P_S=35 €/m², a_{dis} =0.09, n=25)

The maximum and minimum possible LECs, shown in Figure 32, are 0.09 to 0.23 €/kWh$_e$ (Las Vegas), 0.10 to 0.27 €/kWh$_e$ (Almería 2005), and 0.11 to 0.30 €/kWh$_e$ (Almería 2010).

a)
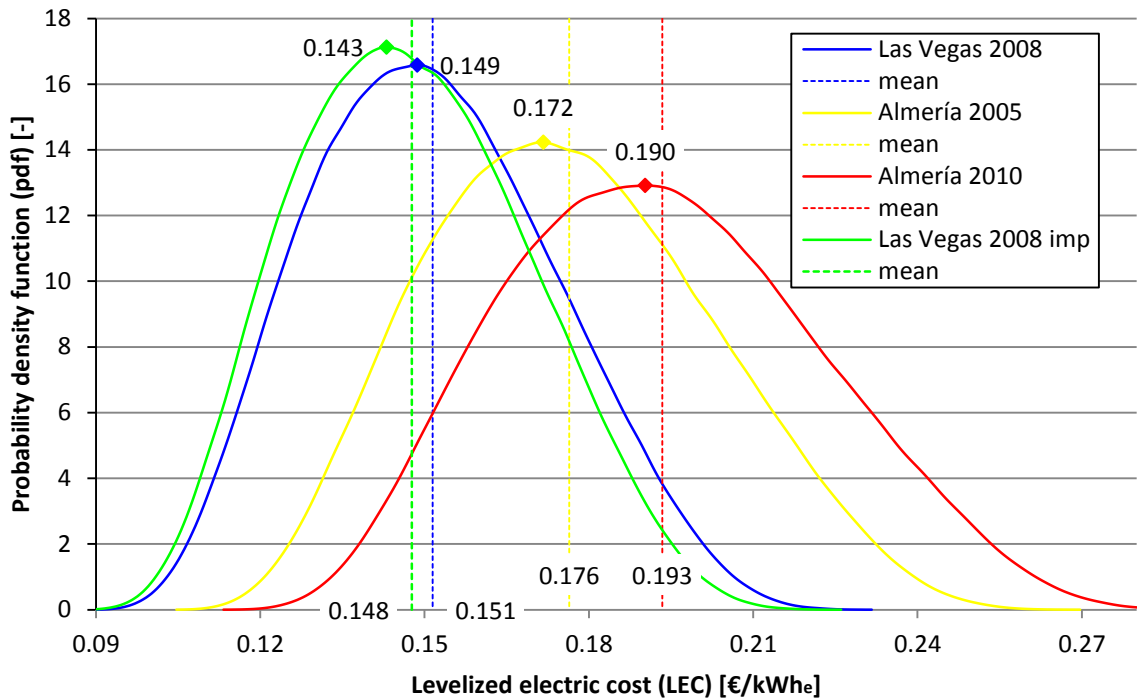
b)
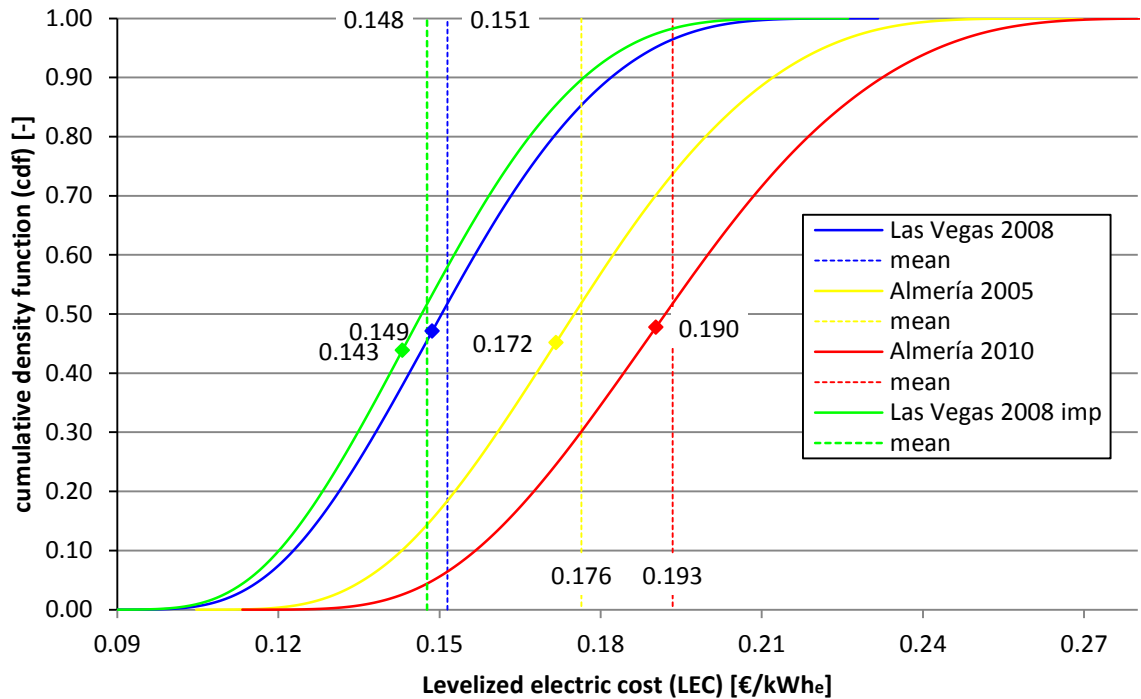
Figure 32: The a) probability density function and b) cumulative density function of the LECs for Las Vegas 2008 (2659 kWh/m²/y), Almería 2005 (2300 kWh/m²/y) and 2010 (2095 kWh/m²/y), and the improved PP of Las Vegas 2008

The range of probable LECs expands when the direct normal irradiation averaged annual sum decreases, and is increased by 16.2% for Almería in 2005 and 28.9% for Almería in 2010, compared to the reference plant's results. The LEC forecast is therefore less accurate, which results in a more uncertain financial situation for the project.

Another disadvantage is the increased LECs. The median LEC is 0.150 €/kWh$_e$ (Las Vegas 2008), 0.175 €/kWh$_e$ (Almería 2005), and 0.192 €/kWh$_e$ (Almería 2010). It is between the mode and mean LEC of the corresponding LEC distribution. The probability that the LEC of the solar thermal power plant is less than the median value is exactly 50%. With a 90% confidence interval ($50\% \pm 45\%$), the LECs are between 0.117 and 0.190 €/kWh$_e$ (Las Vegas 2010), 0.136 and 0.221 €/kWh$_e$ (Almería 2005), and 0.149 and 0.243 €/kWh$_e$ (Almería 2010).

The mode LEC, which is most probable, is 0.149 €/kWh$_e$ (Las Vegas 2008), 0.172 €/kWh$_e$ (Almería 2005), and 0.190 €/kWh$_e$ (Almería 2010). The mode LEC is increased by 13.3% (Almería 2005), and 23.8% (Almería 2010), whereas the normal irradiation averaged annual sum is reduced by 13.5% (Almería 2005), and 21.2% (Almería 2010), compared to the reference plant's results. The function $\overline{DNI}(LEC)$ is assumed to be an exponential function

$$\overline{DNI}(LEC) = a_1 + a_2 e^{-a_3 \cdot LEC} \tag{93}$$

with the limits

$$\lim_{LEC \to \infty} \overline{DNI}(LEC) = 0 \tag{94}$$

and

$$\lim_{LEC \to 0.080} \overline{DNI}(LEC) = \infty \quad , \tag{95}$$

where the mode LEC value of 0.080 €/kWh$_e$ refers to a solar thermal power plant in which the PB operates for the entire year at 100% load. According to this assumption, the calculated net electric output is 1050 GWh. The coefficients a_1 (0.080), a_2 (6275), and a_3 (5.796) can therefore be calculated. The simulated values for Las Vegas 2008, Almería 2005, and Almería 2010, as well as the resulting function of Eq. (93), are plotted in Figure 33. The LECs can therefore be estimated for other locations with direct normal irradiation averaged annual sums
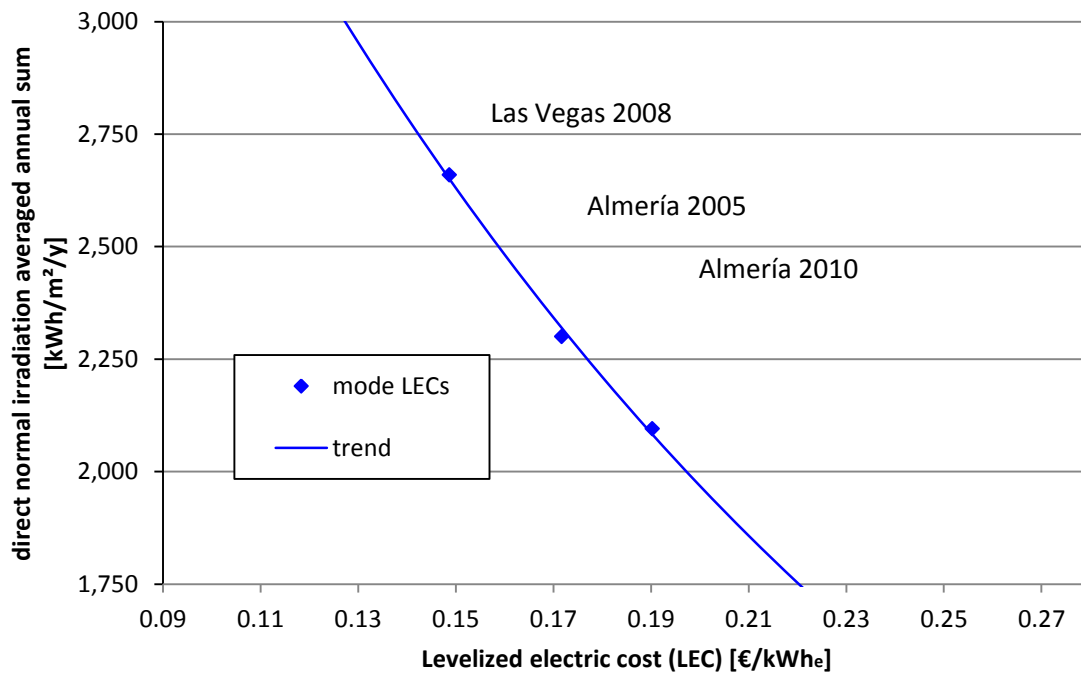
Figure 33: The LECs for Las Vegas 2008 (2659 kWh/m²/y), Almería 2005 (2300 kWh/m²/y) and 2010 (2095 kWh/m²/y), and the trend line of direct normal irradiation averaged annual sum function to LECs

different from that of the reference plant, if the absolute latitude of the location is comparable to Las Vegas' (36.06°) or Almería's absolute latitude (37.08°).

4.6 Improvement of the reference plant

The reference plant, described in Chapter 4.1, is modified to reduce its LECs of it by changing a parameter in the user interface. After each change, the "Design power plant script", shown in Appendix F, generates a redesign of the power plant, and a one-year re-simulation is run. Table 12 lists these improved parameters. The Sankey diagram with the absolute values is found in Appendix P.

The hot tank's temperature was set to 550° C, which is considered to be the maximum level for solar salt. The re-simulation therefore assumes a safety clearance of 50° C. The higher hot tank temperature results in a lower temperature at the SG outlet, and a cold tank design temperature of 290° C has therefore been chosen. During start-up and shut-down, the HTF from the SF is pumped to the hot tank if its temperature is higher than 450° C. More energy is therefore stored in the

Table 12: Changed parameters of the reference plant

Parameter	Reference plant	Improved plant
Hot_Tank_Design_Temp	510° C	550° C
Hot_Tank_Low_Temp	485° C	450° C
Cold_Tank_Design_Temp	310° C	290° C
loops	2H layout	3/2H layout
SM	2.233	2.165
Storage_time	10 h	13 h

hot tank and less in the cold tank. This results in lower SF pumping parasitics, less SF heat loss, and more PB operation hours. The simulation reveals the 3/2 H layout to be the best, reducing SF pumping parasitics and heat losses. The hot tank capacity is also expanded in order to realize 24-hour PB operation during summer days.

Figure 34 shows the comparison of energy flows over the entire simulated year, in which 100% always refer to the results of the reference plant energy flows, shown in Figure 26. Because the solar multiple is decreased by 0.068, the net aperture area of the SF is less, and the collected sun heat is therefore 3.37% less in the improved plant. The overall gross efficiency of the PTCs, without taking solar energy dumping into account, is equal to the reference plant's efficiency. This means that the relative solar heat input (Q_sun), and the effective PTC heat input (Q_PTC_eff) remains constant (96.63%).

The net efficiency is higher because the storage is expanded in the improved simulation, which results in less energy dumping during periods of high radiation. Defocusing of PTCs is 71.3% less than in the reference power plant. This causes a rise of 6.19% in annual net PTC heat input and annual gross PTC heat input (Q_PTC), as shown in Figure 34.

The average SF temperature is higher, so heat losses in the piping elements are also higher (+9.35%), which results in a reduced SF heat output (Q_SF). This output is reduced by 1.59%, as reflected in the annual gross PTC heat input, shown in Figure 34.
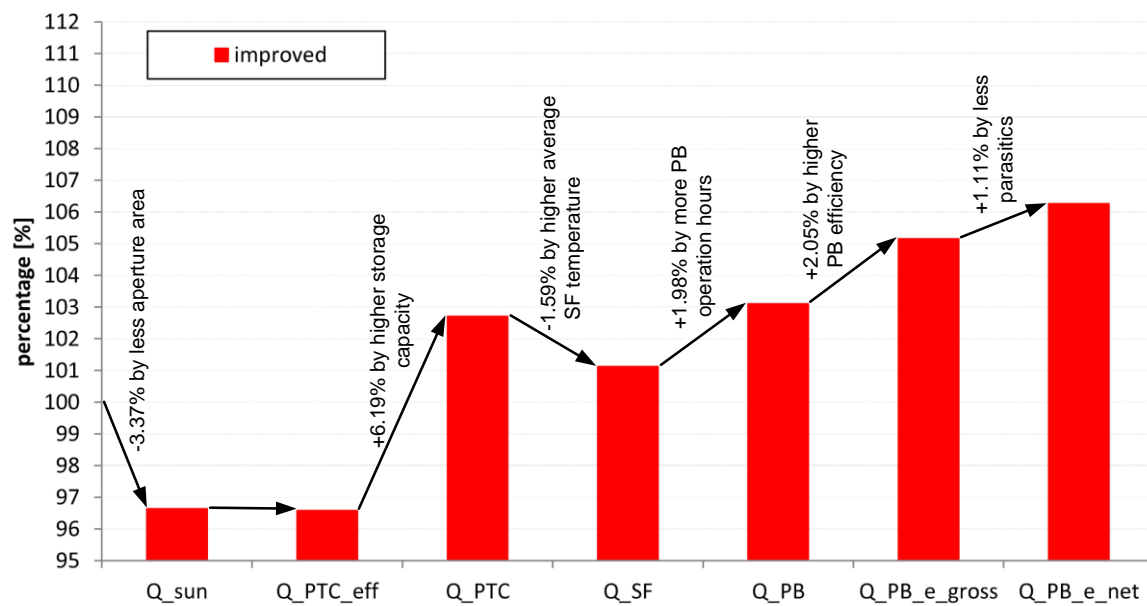
Figure 34: Annual energy comparison for the reference and improved solar thermal power plant – reference plant refers to 100%

Because of the expanded thermal storage system, the PTCs are defocused less, and more energy is stored in the hot tank. The PB operation hours are therefore expanded by 4.25%. During summer periods, 24-h PB operation is realized. As shown in Figure 34, the heat input to the PB (Q_PB) is 1.98% higher than the heat output by the SF. Because of the higher live steam temperature (540° C) at the PB design point, the efficiency increases to 45.1%. This results in a 1.99% higher annual PB gross efficiency. The net electric output of the PB is therefore increased by 2.05%, as measured by the relative change to the heat input into the PB in Figure 34.

The net efficiency of the entire power plant increases because the pumping parasitics are lower in the SF and PB. The pumping parasitics in the SF are reduced due to the optimized layout and the lower cold tank temperature, which is 297.6° C, 4.5% lower than that of the reference plant. The PB feed water mass flow is also reduced by 6.7% at the design point, which results in lower annual PB parasitics. In all, the annual net electric output of the PB increases by 6.3%, whereas the total investment costs increase by 3.1% (based on the mean cost input values listed in Appendix L under "Economic parameters").

The resulting LEC pdf, and cdf is shown in Figure 33. The same economic and statistical model, described in Chapter 4.5, is used to calculate these functions. The input values in this model are PB net electric output (607.8 GWh$_e$), AH reference energy ($Q_{AH,ref}$=45 GWh$_{th}$), total power plant area (3.87 km²), aperture area (1.15 km²), design gross PB capacity (125 MW$_e$), and storage capacity (3,888,112 kWh$_{th}$). The mode LEC is reduced by 0.6 cents/kWh$_e$, whereas the mean LEC is reduced by 0.3 cents/kWh$_e$. The distribution of probable LECs is reduced by 3.5%, so the LEC forecast is more accurate for the improved power plant. The 90% LEC confidence interval ($50\% \pm 0.45\%$) is between 0.114 and 0.184 €/kWh$_e$. This interval is 4.1% lower than that of the reference plant.

4.7 Comparison of various cooling methods

In order to compare various PB cooling methods, the reference plant, described in Chapter 4.1, is modified by changing the value of the parameter $a_{\mathrm{P\_turbine\_pack\_pressure}}$, listed in Appendix C, from 0.08 bar to 0.25 bar and 0.5 bar. The pressure of 0.25 bar reflects a hybrid cooling system, and the pressure of 0.5 bar reflects a dry cooling system (NREL 2009, p. 16). All other parameters remain equal to those of the reference plant.

The reference plant annual PB net efficiency is 41.4%, and the net efficiency of the entire solar thermal power plant is 18.4%. The PB net efficiency is plotted as a continuous blue line in Figure 35. It is approximately 43.9% at full PB load, and 39.1% at 40% PB load. The red line corresponds to the net efficiency of the PB with hybrid cooling system, and is 39.9% at full load and 35.6% at 40% load. The PB with dry cooling system (green line) has a net efficiency of 37.5% at full load and 33.1% at 40% load.

The ratio of the net PB efficiency with alternative cooling system ($\eta_{PB,j}$) to the net efficiency of the reference plant ($\eta_{PB,wet}$)

$$r_j = \frac{\eta_{PB,j}}{\eta_{PB,wet}}, \quad j = hybrid, dry \tag{96}$$

is plotted in Figure 35. It decreases with PB load and can be fitted by the following two functions.
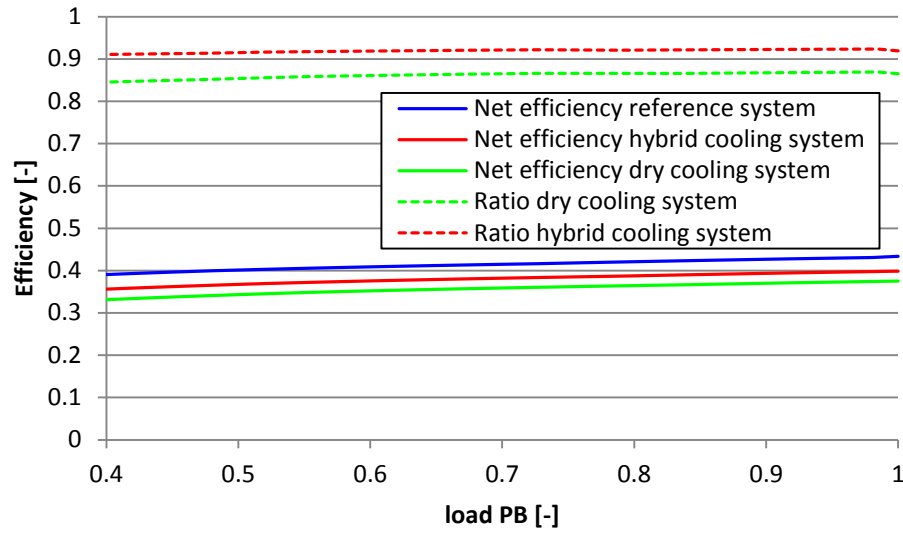
Figure 35: PB efficiency to the PB load for two different cooling systems.

$$r(x)_{hybrid} = 0.8768 + 0.1231x - 0.1075x^2 + 0.03x^3 \qquad (97)$$

$$r(x)_{dry} = 0.7741 + 0.2666x - 0.2521x^2 + 0.0791x^3 \qquad (98)$$

If the thermal input into the PB remains constant, the electrical output of the PB with alternative cooling system at a specific time instant

$$\dot{Q}_{el,j}(t) = r\left(\frac{\dot{Q}_{e,net,wet}(t)}{\dot{Q}_{e,net,D,wet}}\right)_j \dot{Q}_{e,net,wet}(t), \; j = hybrid, dry \qquad (99)$$

is calculated using the factors from Eqs (97) and (98), the electric power at the design point of the reference power plant ($\dot{Q}_{e,net,D,wet}$), and the electrical output of the time instant ($\dot{Q}_{e,net,wet}(t)$). Because the thermal power input into the PB is assumed to be equal to the thermal power input in the reference plant simulation, the results can be transferred to the PB with alternative cooling system without influencing the reference SF system behavior. Adopting Eq. (99) for the reference plant's time series dialogue results yields, electrical net outputs of 538.7 GWh (hybrid cooling) and 506.7 GWh (dry cooling). The electrical energy produced is 10.8% (hybrid), and 16.1% (wet) less than that of the reference plant. This result matches the 5% to 20% efficiency penalties proposed by (California Energy Commission 2002, p. 1-9).
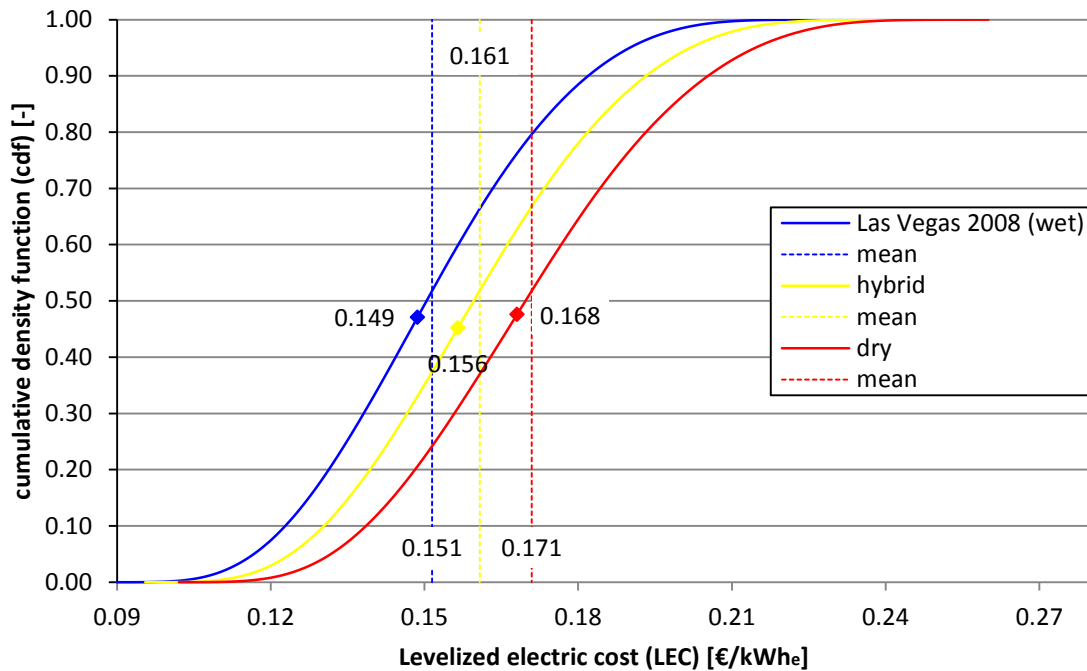
Figure 36: The cumulative density function of the LECs for Las Vegas 2008 with wet cooling system, hybrid cooling system, and dry cooling system

To calculate the LECs, the simulation assumes an overall water reduction of 30% and 70% (hybrid and dry cooling system, respectively). It also assumes that the costs of the reference plant cooling system are 1% of the overall costs of the PB and that a hybrid cooling system entails a 300% cost increase and a dry cooling system a 900% increase. It assumes no differences in operating and maintenance costs (California Energy Commission 2002, p.9-2ff).

Figure 36 shows the resulting LEC cdf for the three cooling systems. The mean LEC value increases by 1 and 2 dent/kWh$_e$, which translates to an increase of 6.6% (hybrid) and 13.2% (dry). The mode LEC increases by 0.7 and 1.9 Cent/kWh$_e$, which translates to an increase of 4.7% (hybrid) and 12.8% (dry). The cdf of hybrid and dry cooling system LEC values is also expanded by 5.6% and 11.3%, respectively, and the LEC forecast is therefore less accurate, resulting in less certain project finance. Further discussion of the power plant's cooling system is found in Appendix Q.

5 Summary and Conclusion

In this thesis, a transient thermodynamic model of a solar thermal power station is implemented into the commercial software tool EBSILON®Professional 10.01.01. The solar field is modelled in transient mode using both the indirect storage component and the direct storage component. The system behavior of the PB is modelled in pseudo-transient mode by an EbsScirpt that estimates the PB thermal inertia. A user interface allows up to 42 parameters to be specified to design an individual solar thermal power plant, including design parameters, operation strategy parameters, and simulation mode parameters.

Different choices of SF layout (I, H, 3/2, 2 H layout), PTC (EuroThrough 150, HelioTrough, UltimateTrough), solar multiple, storage time, and AH capacity allow the SF model to be individualized. Several SF pipe design parameters are also available, e.g. wall thickness, design HTF velocity, and pipe wall roughness. A ramp-up factor and start-up time can also be specified in the interface to model the pseudo-transient behavior of the PB. The gross capacity of the power plant and the turbine back-pressure can be specified.

The model uses plant operation management to identify the instant of time for PB, AH, and SF start-up, all of which can also be specified in the user interface.

Simulation mode can be set to transient or steady simulation. Only start-up, shut-down, and transient SF states during clouding can be simulated in transient mode, which results in a simulation wall clock time of about 12 hours at a common work station (one year with ten-minute resolution). The entire time between start-up and shut-down, or the entire year, can also be simulated in transient mode, which results in a very long simulation wall clock time (up to 10 times as long).

The implementation of the solar thermal power station into the EBSILON®Professional software was a "Husarenstück", because several problems occurred.

First, the instationary component 119 was introduced in the latest version, version 10, and is therefore new. The software uses only a second-order boundary condition between the environment and the component, which is not suitable for PTC simulation. A third boundary condition, simulating the specific heat input to the component, would be more realistic.

The EbsScript function "transferAllResults" could not be used in the implemented model because the component 119 matrix values (e.g. the temperatures in the indirect storage component), could not be transferred to other Ebsilon profiles. This Ebsilon bug prevented the use of Ebsilon profile selection, and an EbsScript instead implemented the profile selection into the model. Various profiles must therefore be implemented by a code instead of the Ebsilon graphical user interface. If this bug were to be solved in the future, the standard Ebsilon profile selection could be used to enable a more user-friendly implementation of new profiles.

Another problem was that numeric controllers (Component 39 and 12) are only able to operate during stationary simulations. During transient simulations, these components cause errors. The "Forecast salt mass flow", shown on the left side of the screenshot in Appendix A, was therefore implemented. This model calculates the SF mass flow for the next time instant, performing a steady simulation. This result is used in the next time instant if a transient simulation is in progress.

Second, it was difficult to determine the numerical accuracy of the simulation. If the simulation does not converge to the desired residuals of 10^{-7}, the value of the function "@calcoptions.res.status" is 3. However, the value of the function "@calcoptions.sim.matprec" was always 3, indicating residuals of 10^{-7}. Ebsilon does not offer a tool for tracking numerical accuracy for simulations in the time series dialog. Therefore the numerical accuracy was estimated, as described in Chapter 4.2.1. The accuracy was identified as being between 10^{-5} to 10^{-3}, for the simulation of the entire year.

In order to simulate the solar thermal power plant's LECs, a stationary simulation with a ten-minute discretization is proposed. For Las Vegas, the difference in the net electric output between stationary and transient simulation is identified as 0.53%, which is relatively low. The simulation wall clock time is 50% lower than the transient simulation. The transient simulation offers more realistic results, wherefore a time resolution of less than 15 minutes is proposed.

The LECs were calculated for a reference plant for three different years with different averaged direct normal irradiation annual sums (2095 kWh/m²/y, 2300 kWh/m²/y, and 2659 kWh/m²/y). The reference plant's PB has a gross design capacity of 125 MW, and its live steam parameters are 150 bar and 550° C. The solar field layout is assumed to be a 2 H layout with 352 collector loops, each consisting of four Eurotrough ET150 collectors. The solar multiple is therefore 2.233. The storage time is 10 h.

Given the 90% confidence interval ($50\% \pm 45\%$), the LECs are between 0.117 and 0.190 €/kWh$_e$ (2659 kWh/m²/y), 0.136 and 0.221 €/kWh$_e$ (2300 kWh/m²/y), and 0.149 and 0.243 €/kWh$_e$ (2095 kWh/m²/y). The mode LECs are 0.149 €/kWh$_e$, 0.172 €/kWh$_e$, and 0.190 €/kWh$_e$. An improved solar thermal power plant was identified, so the mode LEC is reduced by 0.6 cents/kWh$_e$. The 90% LEC confidence interval is between 0.114 and 0.184 €/kWh$_e$.

The economic impact of wet, hybrid, and dry PB cooling methods were also compared. The mode LEC increased by 0.7 for hybrid cooling and 1.9 Cent/kWh$_e$ for dry cooling.

The solar thermal power plant model offers much scope for parameter variation, allowing further investigation. The designed solar thermal power plants can be compared by using the implemented statistic and economic model to calculate the LECs. Further investigations in the simulation mode (transient or steady), and varying time series time steps are also possible.

Plant operation management strategy is kept as simple as possible. For example, the auxiliary heater only operates when the temperature in the solar field is critical. The model accounts for no SF or PB support during start-up. Plant operation management could therefore be modelled in more detail in order to raise the economic performance of the entire plant.

Appendix

Appendix A: Screenshot of the Ebsilon model of the solar field
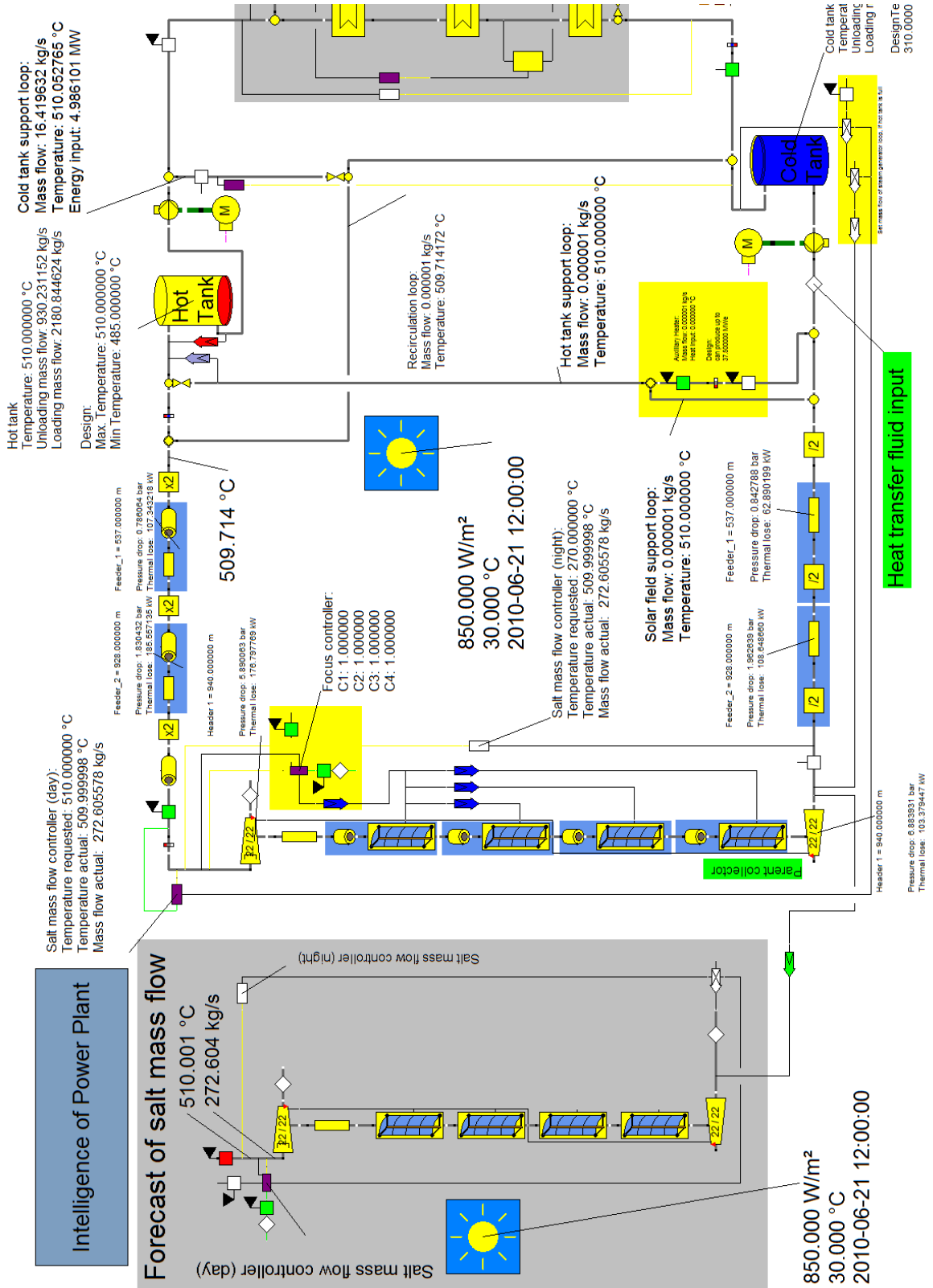
Appendix B: Screenshot of the Ebsilon model of the power block
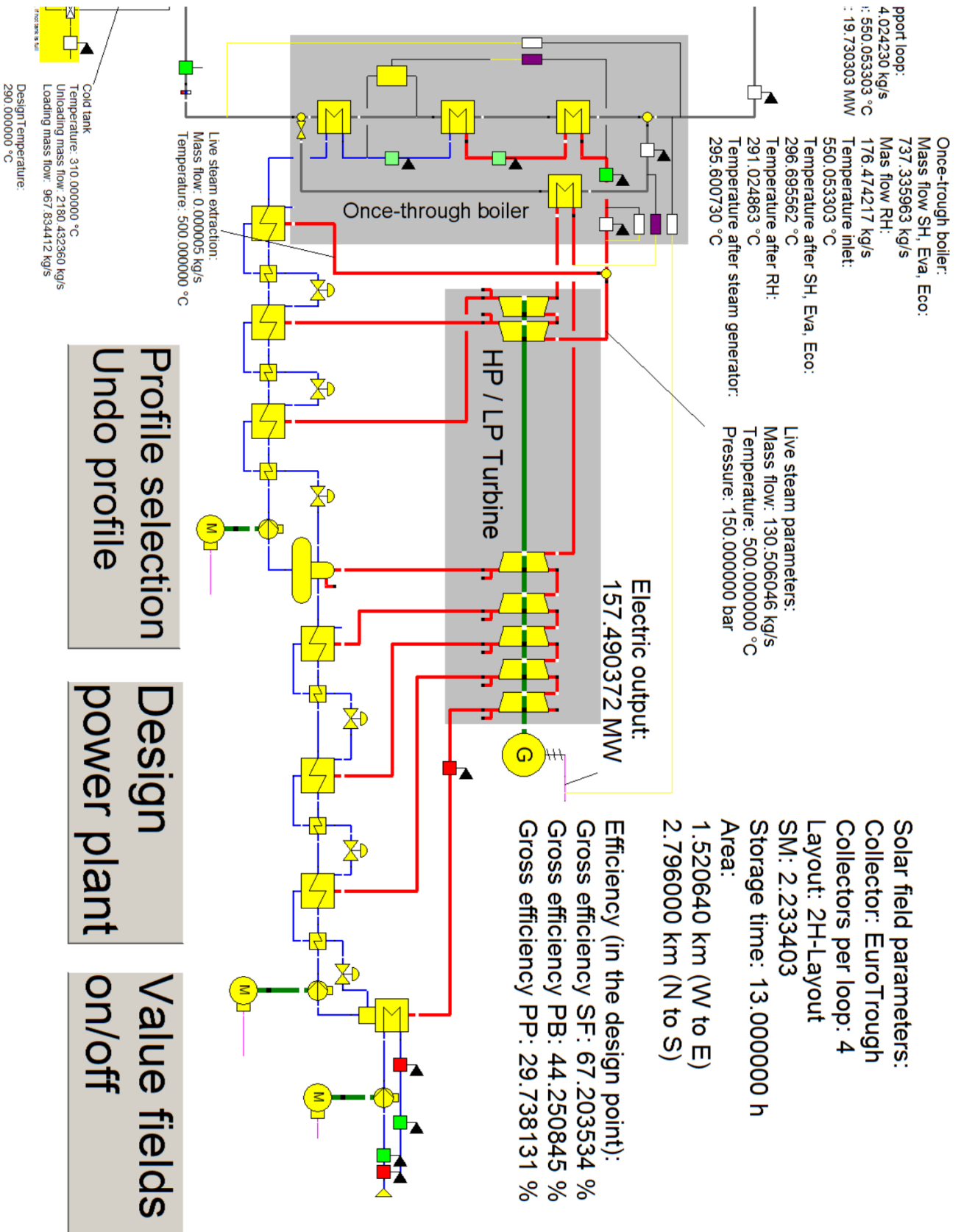
Appendix C: User input parameters and output parameters for the design process of the solar thermal power plant

User input parameters to design the solar field and the power block

Parameters for the design point of the SF

Location	The location of the power plant (Las Vegas, Almería or user-defined at sun component), described in Chapter 3.1.2 and used for the DNI-5034 algorithm
T_amb_design	Temperature at design point of the solar thermal power plant used for the Eq. (26) and (33)
DNI_design	DNI at the design point of the solar thermal power plant
Date_design	Date at the design point of the solar thermal power plant

Parameters for solar field layout

loops	Layout of the solar field (I, H, 3/2 H and 2 H layout), described in Chapter 3.1.3
SM	Solar multiple of the solar thermal power plant
PTC_type	Type of parabolic trough collector, listed in Appendix H and described in Chapters 2.2, 2.3 and 3.1.4 (EuroTrough + PTR 70, HelioTrough + PTR 90, UltimateTrough + PTR 90, user-defined at parent collector component)
PTC_loop	Number of collectors in a loop (four, six, eight, or ten), described in Chapter 3.1.3 and employed in Eq. (10)
W_PP	Width of balance of plant, described in Chapter 3.1.5 and employed in Eq. (19) and (20)
D_u_pipe	Distance between two u-pipe elements for thermal tension release, described in Chapter 3.1.5 and employed in Eq. (23)

S_u_pipe_f1	Side length of u-pipe for feeder 1, described in Chapter 3.1.5 and employed in Eq. (24)
S_u_pipe_f2	Side length of u-pipe for feeder 2, described in Chapter 3.1.5 and employed in Eq. (24)
S_u_pipe_h	Average side length of u-pipe in header, described in Chapter 3.1.5 and employed in Eq. (24)
Parameters for pipe design	
Heat_losses_pipe	Heat losses of all piping elements (except parabolic trough receiver) and distributing and collecting header, described in Chapter 3.1.5 and employed in Eq. (26)
V_Design	Design velocity for piping elements and headers, described in Chapters 3.1.5, 3.1.8.2, and 3.1.8.3 and employed in Eq. (28), (44), (47), (52) and (53)
KS	Pipe wall roughness for piping elements and headers, described in Chapter 3.1.5 and employed in Eq. (28)
Parameters for storage system described in Chapter 3.1.6	
Storage_time	Time electricity can be produced at 100% load of power plant using only thermal capacity of storage, described in Chapter 3.1.6 and employed in Eq. (31)
Delta_T_tank	Temperature drop of full hot storage tank over one day, described in Chapter 3.1.6 and employed in Eq. (33)
Hot_Tank_Design_Temp	Design temperature of hot tank, described in Chapter 3.1.6 and employed in Eq. (33)
Cold_Tank_Design_Temp	Design temperature of cold tank
Parameters for auxiliary heater design	
Load_AH	Percentage of total gross capacity that only auxiliary heater can produce, described in Chapter 0

Parameters for transient simulation	
t_feeder	Thickness of feeder and header pipes, described in Chapters 3.1.8.2 and 3.1.8.3 and employed in Eq. (51)
D_outer_PTR	Outer diameter of parabolic trough receiver (must only be defined if user-defined collector is used for simulation)

Parameters for PB	
Gross_capcity	Gross capacity of power plant
P_turbine_pack_pressure	Turbine pack pressure, described in Chapter 0

User input parameters for plant operation management	

Simulation mode	
ts_tsc	Time step of time series calculation
Forecast_Timesteps	Transient simulation mode, used in EbsScript in Appendix G "1" calculates whole day transient (slow), or whole year transient (very slow, comment lines 508-528 in EbsScript Intelligence) "2" calculates start-up, shut-down, and low-clouding periods during day transient (fast)
Mode_SF	Simulation mode of C unit, described in Chapter 3.2.5 "1" Transient "0" Quasi-stationary
Mode_H	Simulation mode of F-H unit, described in Chapter 3.2.5 "1" Transient "0" Quasi-stationary

Pseudo-transient behavior of PB, described in Chapter 3.2.6	
d_SMF_d_t	Gradient of salt mass flow during power block start up in kg/s/s employed in Eq. (67)
Delta_t_startup	Time for PB start-up employed in Eq. (64)

Parameters to identify the weather conditions of a day, described in Chapter 3.3	
Min_DNI_PB	Minimum DNI over one day to start-up power block
DNI_bad_day	Maximum average DNI for bad day
DNI_very_good_day	Minimum average DNI for very good day

Parameters to identify whether power block can operate, described in Chapter 3.3	
Min_HT_Level_PB_OP	Minimum hot tank level if power block is operating
Min_HT_Level_bad_day	Minimum hot tank level for power block operations for a bad day
Min_HT_Level_good_day	Minimum hot tank level for power block operations for a good day
Min_HT_Level_very_good_day	Minimum hot tank level for power block operations for a very good day
Min_HT_Level_Day_AH	Minimum hot tank level for AH during day
Min_HT_Level_Night_AH	Minimum hot tank level for AH during night

Parameters to identify whether solar field can operate, described in Chapter 3.3	
Min_Salt_M	Minimum salt mass flow for solar field operations

Further parameters for plant operation management, described in Chapter 3.3	
Hot_Tank_Low_Temp	Lowest temperature of hot tank
Salt_Low_Temp	Lowest temperature of molten salt

Design output parameters

Parameters of the SF capacity	
M_tank	Total mass of hot and cold storage tanks
C_tank	thermal capacity of hot tank
SM_real	The real solar multiple after design process (exact SM can normally never be achieved)

Salt mass flow at design point	
SMF_PB_Design	Salt mass flow into power block
SMF_SF_Design	Salt mass flow into solar field
SMF_Aux_Design	Salt mass flow into auxiliary heater

Geometric parameters of the SF	
L_Feeder_1	Length of first feeder (with u-pipes) employed in Eqs (26) and (28)

L_Feeder_2	Length of second feeder (with u-pipes) employed in Eqs (26) and (28)
Nbranch	Number of header branches used in Eqs (47), (49), (51) and (52)
L_Header	Length of collecting and distributing header (with u-pipes) employed in Eqs (25), (26), (29) and (30)
A	Land use of entire power plant
W_O	Length of entire power plant from west to east
N_S	Length of entire power plant from north to south
Aperture_Area	Total gross aperture area of collectors
Efficiency parameters	
Gross_eff_SF	Gross efficiency of solar field
Net_eff_SF	Net efficiency of solar field
Gross_eff_PB	Gross efficiency of PB
Net_eff_PB	Net efficiency of PB
Gross_eff_PP	Gross efficiency of power plant
Net_eff_PP	Net efficiency of power plant

Appendix D: The time series dialog in Ebsilon

Time-Series-Calculation

TimeSeries Calculate View Edit Extras

Las_Vegas_2008_10_Min [1] ◄ ►   Break   Recalc time   ☑ auto-scroll   Profile   Design ◄

#	A	B	C	D	E	F	G	H	I	J	K	L	M	N
1	Comment				Sun Height	Prediction of...	SolarField op...	Time steps o...	Time steps o...	Simulation M...	Profile	Error Code	Hot tank	Cold tank
2	Type		spec	spec	result	result	result	result	result	result	result	result	result	result
3	Definition	Calculation options	Sun.DNI	Sun.TAMB	Sun.RSHEIGHT									
4	Processing	ebsscript:"Intelligence";profil...				Intelligence.....		Intelligence.....	Intelligence.....	Intelligence.....	Intelligence.....	@calcoption....	Intelligence.....	Intelligence.....
5	Date/Time | Unit ->	auto-inserted	W/m²	°C	°	kg/s	-	-	-	-	-	-	-	-
6	2008-01-01 00:05:00			4.5353	-2.000	351.129606	0.000000	0.000000	0.000000	0.000	4.000	1.000	0.022	0.978
7	2008-01-01 00:15:00			4.4901	-2.000	351.136878	0.000000	0.000000	0.000000	0.000	4.000	1.000	0.022	0.978
8	2008-01-01 00:25:00			4.4503	-2.000	353.167898	0.000000	0.000000	0.000000	0.000	4.000	1.000	0.020	0.980
9	2008-01-01 00:35:00			4.5641	-2.000	354.167342	0.000000	0.000000	0.000000	0.000	4.000	1.000	0.019	0.981
10	2008-01-01 00:45:00			4.3026	-2.000	354.202080	0.000000	0.000000	0.000000	0.000	4.000	1.000	0.017	0.983
11	2008-01-01 00:55:00			4.0483	-2.000	354.249085	0.000000	0.000000	0.000000	0.000	4.000	1.000	0.016	0.984
12	2008-01-01 01:05:00			3.8343	-2.000	354.289938	0.000000	0.000000	0.000000	0.000	4.000	1.000	0.014	0.986
13	2008-01-01 01:15:00			3.7731	-2.000	354.307184	0.000000	0.000000	0.000000	0.000	4.000	1.000	0.013	0.987
14	2008-01-01 01:25:00			4.0454	-2.000	354.271170	0.000000	0.000000	0.000000	0.000	4.000	1.000	0.012	0.988
15	2008-01-01 01:35:00			3.8573	-2.000	354.294841	0.000000	0.000000	0.000000	0.000	5.000	1.000	0.016	0.984
16	2008-01-01 01:45:00			3.2207	-2.000	355.409511	0.000000	0.000000	0.000000	0.000	4.000	1.000	0.015	0.985
17	2008-01-01 01:55:00			3.2483	-2.000	356.443305	0.000000	0.000000	0.000000	0.000	4.000	1.000	0.013	0.987
18	2008-01-01 02:05:00			3.4061	-2.000	356.401456	0.000000	0.000000	0.000000	0.000	4.000	1.000	0.012	0.988
19	2008-01-01 02:15:00			3.206	-2.000	356.413672	0.000000	0.000000	0.000000	0.000	5.000	1.000	0.016	0.984
20	2008-01-01 02:25:00			3.0306	-2.000	357.466322	0.000000	0.000000	0.000000	0.000	4.000	1.000	0.015	0.985
21	2008-01-01 02:35:00			2.7376	-2.000	358.540423	0.000000	0.000000	0.000000	0.000	4.000	1.000	0.013	0.987
22	2008-01-01 02:45:00			2.4173	-2.000	358.561524	0.000000	0.000000	0.000000	0.000	4.000	1.000	0.012	0.988
23	2008-01-01 02:55:00			2.5199	-2.000	358.524816	0.000000	0.000000	0.000000	0.000	5.000	1.000	0.016	0.984
24	2008-01-01 03:05:00			2.3938	-2.000	359.567904	0.000000	0.000000	0.000000	0.000	4.000	1.000	0.015	0.985
25	2008-01-01 03:15:00			2.1012	-2.000	360.644787	0.000000	0.000000	0.000000	0.000	4.000	1.000	0.013	0.987
26	2008-01-01 03:25:00			1.6947	-2.000	360.662307	0.000000	0.000000	0.000000	0.000	4.000	1.000	0.012	0.988
27	2008-01-01 03:35:00			1.5661	-2.000	360.645321	0.000000	0.000000	0.000000	0.000	5.000	1.000	0.016	0.984
28	2008-01-01 03:45:00			1.2548	-2.000	361.729040	0.000000	0.000000	0.000000	0.000	4.000	1.000	0.015	0.985
29	2008-01-01 03:55:00			1.1801	-2.000	362.782102	0.000000	0.000000	0.000000	0.000	4.000	1.000	0.013	0.987
30	2008-01-01 04:05:00			1.4261	-2.000	362.678172	0.000000	0.000000	0.000000	0.000	4.000	1.000	0.012	0.988
31	2008-01-01 04:15:00			1.3203	-2.000	362.624149	0.000000	0.000000	0.000000	0.000	5.000	1.000	0.016	0.984
32	2008-01-01 04:25:00		0	1.2099	-2.000	363.682065	0.000000	0.000000	0.000000	0.000	4.000	1.000	0.015	0.985

Appendix E: Input and output parameters in the time series dialog

Input parameters	
At each iteration step	
Date/Time	Date and the time of current simulation
Sun.DNI	Solar radiation
Sun.TAMB	Dry bulb ambient temperature
At first Iteration step (boundary conditions)	
Hot_tank.TSTO	Temperature of hot tank
Cold_tank.TSTO	Temperature of cold tank
Hot_tank.LEVACT	Mass stored in hot tank
Cold_tank.LEVACT	Mass stored in cold tank
Output parameters	
Parameters for power plant management	
I.Salt_M_Prediction	Predicted salt mass flow predicted by forecast collector loop
I.Solarfield_operation	"0" if SF is unable to operate, "1" if SF is able to operate
I.profile	Selected profile for this time instant: "1" refers to "Solar field / power block profile (steady)" "2" refers to "Solar field / - profile (steady)" "3" " refers to " - / Power block - profile (steady)" "4" refers to "- / - profile (steady)" "5" refers to "- / - profile with Auxiliary Heater (steady)" "6" refers to "Solar field / power block profile (transient)" "7" refers to "Solar field / - profile (transient)" "8" refers to "Solar field / - profile with Auxiliary Heater (transient)"

Parameters for transient simulation

I.transient_ts	Number of time steps of transient simulation of collector loop
I.transient_ts_2	Number of time steps of transient simulation of collecting header and hot feeder pipelines
I.sim_mode	Mode of simulation of C unit: "0" refers to steady simulation, "1" to start-up procedure during morning, and "2" to transient behavior because of clouding during day or shut-down procedure at the end of the day
I.sim_mode_2	Like I.sim_mode for the H-F unit

Parameters of storage system

I.Hot_Tank_Level	Level of hot tank
I.Cold_Tank_Level	Level of cold tank
I.Hot_tank.TSTO	Temperature of hot tank
I.Cold_tank.TSTO	Temperature of cold tank

Temperatures of the SF

H2._2.T	Temperature at outlet of collecting header
IS_7._2.T	Temperature at outlet of feeder 1

PTCs parameters

Focus.H	Focus of all collectors (from 0 to 1)

Parameters of power block

S5._1.M	Mass flow into power block
Power.Q	Simulated electric power of power plant
Real Power	Real electric power of power plant
I.Q_startup	Thermal energy into power block

Thermal energy flow in solar thermal power plant

I.Q_PB	Thermal power into steam generator
I.Q_Sun	Thermal power of sun on net aperture area of collectors
I.Q_PTC	Thermal power that HTF absorbs
I.Q_SF	Thermal power to HTF over entire solar field

I.Q_PTR	Thermal losses in collector
I.Q_Piping	Thermal losses in pipings and headers
I.Q_tank	Thermal losses of hot and cold tanks
I.Q_IS_F_H	Positive if thermal power is transferred from HTF into steel of the headers and feeders; negative if thermal power is transferred in opposite direction
I.Q_IS_C	Positive if thermal power is transferred from HTF into steel of PTCs; negative if thermal power is transferred in opposite direction
I.Q_pump_SF	Thermal energy input into HTF by two submersion pumps of SF

| Parasitics of solar thermal power plant	
I.Parasitics_PB	Pumping parasitics of PB
I.Parasitics_SF	Pumping parasitics of SF
I.Parasitics_AH	Thermal energy consumed by auxiliary heater
I.Parasitics_Hot_tank	Thermal power into cold tank by HTF from hot tank

Parameters of sun	
Sun.RSHEIGHT	Height of sun
Sun.RSAZIM	Azimuth angle of sun
Sun.RPHIINC	Incident angle of sun

| Calculation results	
@calcoptions.res.status	Status of current simulation "0" Successful "1" Successful with warnings "2" Maximum number of iterations reached "3" Maximum number of iterations reached with warnings "4" Calculation error "5" Error before calculation "6" General error
@calcoptions.res.time	Time needed for simulation of this time instant in milliseconds

@calcoptions.res.iter	Iterations needed for simulation of this time instant
@calcoptions.sim.matprec	Residuals of simulation
	"3" correlates to 10^{-7}
	"2" correlates to 10^{-6}
	"1" correlates to 10^{-5}
	"0" correlates to 10^{-4}
I.Check_simulation	Status of simulation check
	"0" no simulation check required
	"1...99" Changed salt mass flow into solar field in ± 1 kg/s steps
	"100" turned off instationary component IS7
	"101" turned off instationary component IS6
	"102" turned off instationary component IS5
	"103" set salt mass flow into solar field to 0 kg/s
Intelligence.Check_tank	Status of tank check
	"" no tank check
	">0" Mass defect due to error $\rightarrow$ overcharge deduced from cold tank

Appendix F: Schematic of the EbsScript to design the power plant
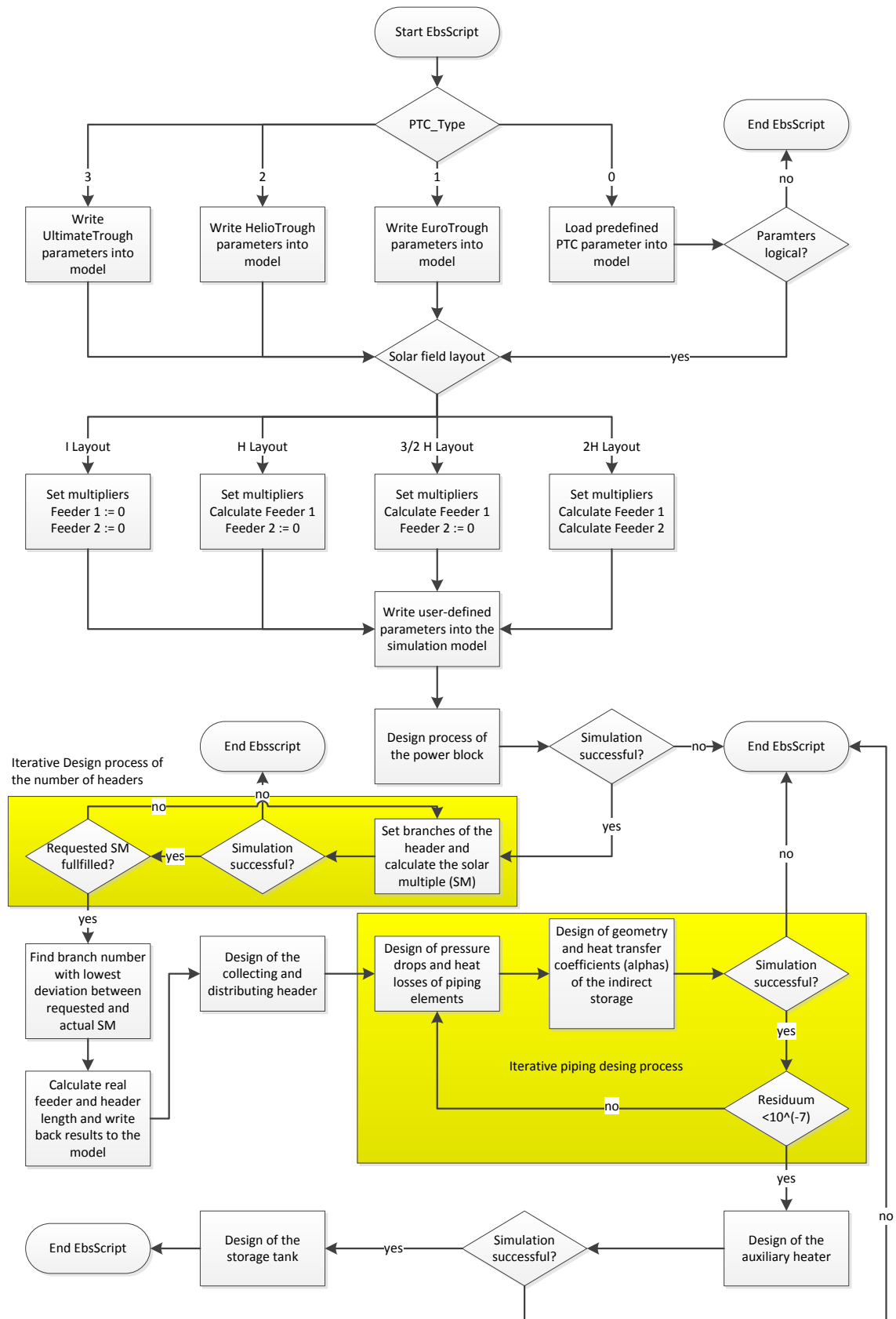
Appendix G: Schematic of the EbsScript for plant operation management, executed before each time instant of the time series dialog
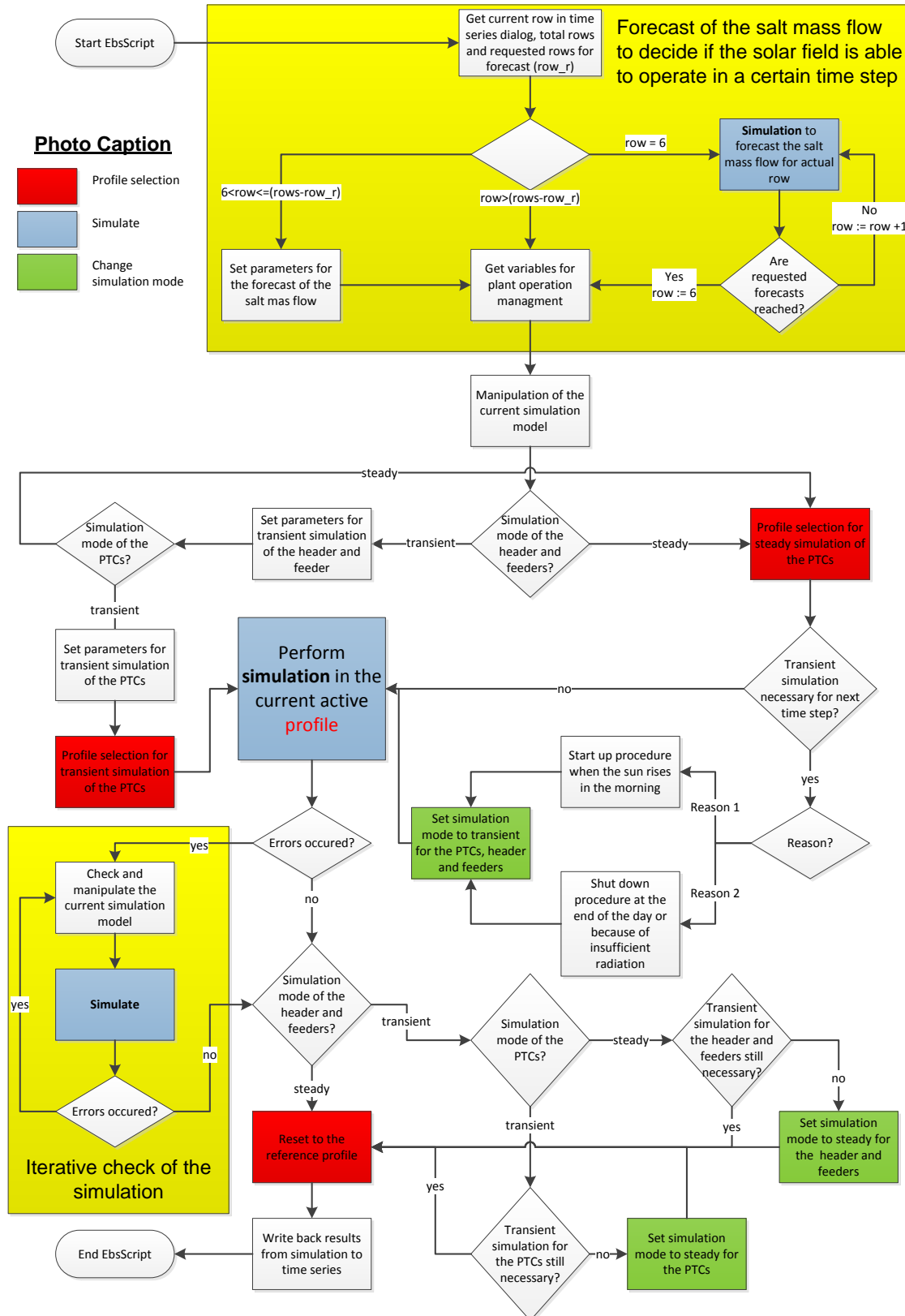
## Appendix H: The parameters of the three implemented PTCs

Property	EuroTrough ET150 + PTR 70	HelioTrough + PTR 90	UltimateTrough + PTR 90
Geometric parameters			
Outer diameter	0.07 m	0.09 m	0.09 m
Inner diameter	0.064[a] m	0.082[a] m	0.082[a] m
Focal length	1.71 m	1.86[1] m	1.95[1] m
Aperture width	5.77 m	6.78 m	7.5 m
Length	148.5 m	191 m	242 m
Radial distance	17.28 m	20.92[2] m	23.2[2] m
Net aperture area	817.5 m²	1263 m²	1689 m²
Pipe wall roughness	10^{-6} m	10^{-6} m	10^{-6} m
Optical Parameters			
Optical efficiency	76.8%	81[a]%	80[a]%
Cleanliness factor	98%	98%	98%

Incident angle modifier[3] $IAM = \max\left(0, (1 + a_1\theta_i + a_2\theta_i^2)\right)$

a_1	0.00010596
a_2	0.00017091

Heat losses[3] $\dot{q} = b_1 \cdot T_{PTR} + b_1 \cdot T_{PTR}^4$

b_1	0.141
b_1	$6.48 \cdot 10^{-9}$

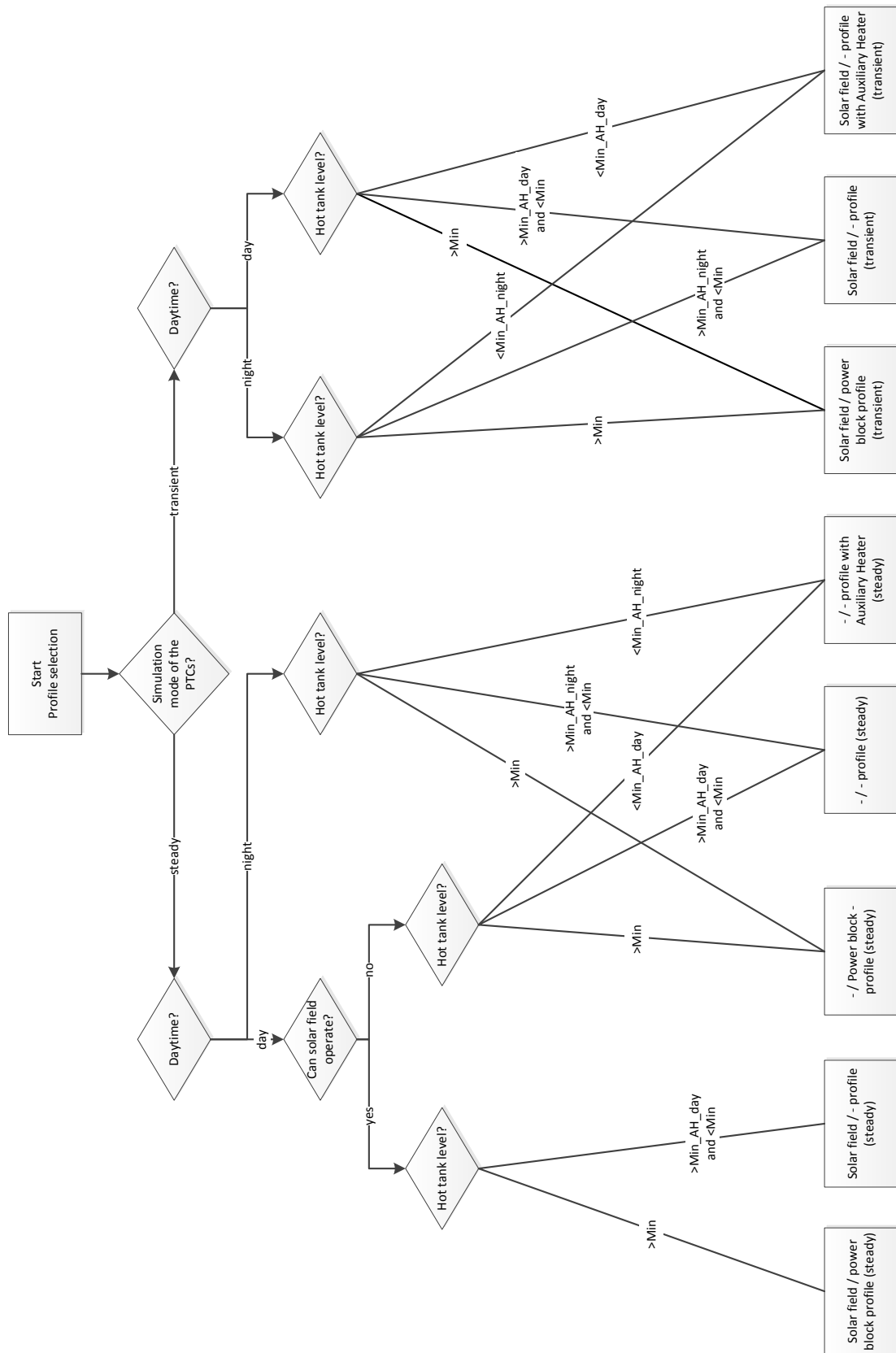[a] assumption [1] assumption based on $\sqrt{2 \cdot Aperture\ width}$
[2] assumption based on $\frac{17.28}{5.77} \cdot Aperture\ width$
[3] because no data is available in literature, parameters are adapted to all three PTCs

Appendix I: T-S diagram of the designed power block
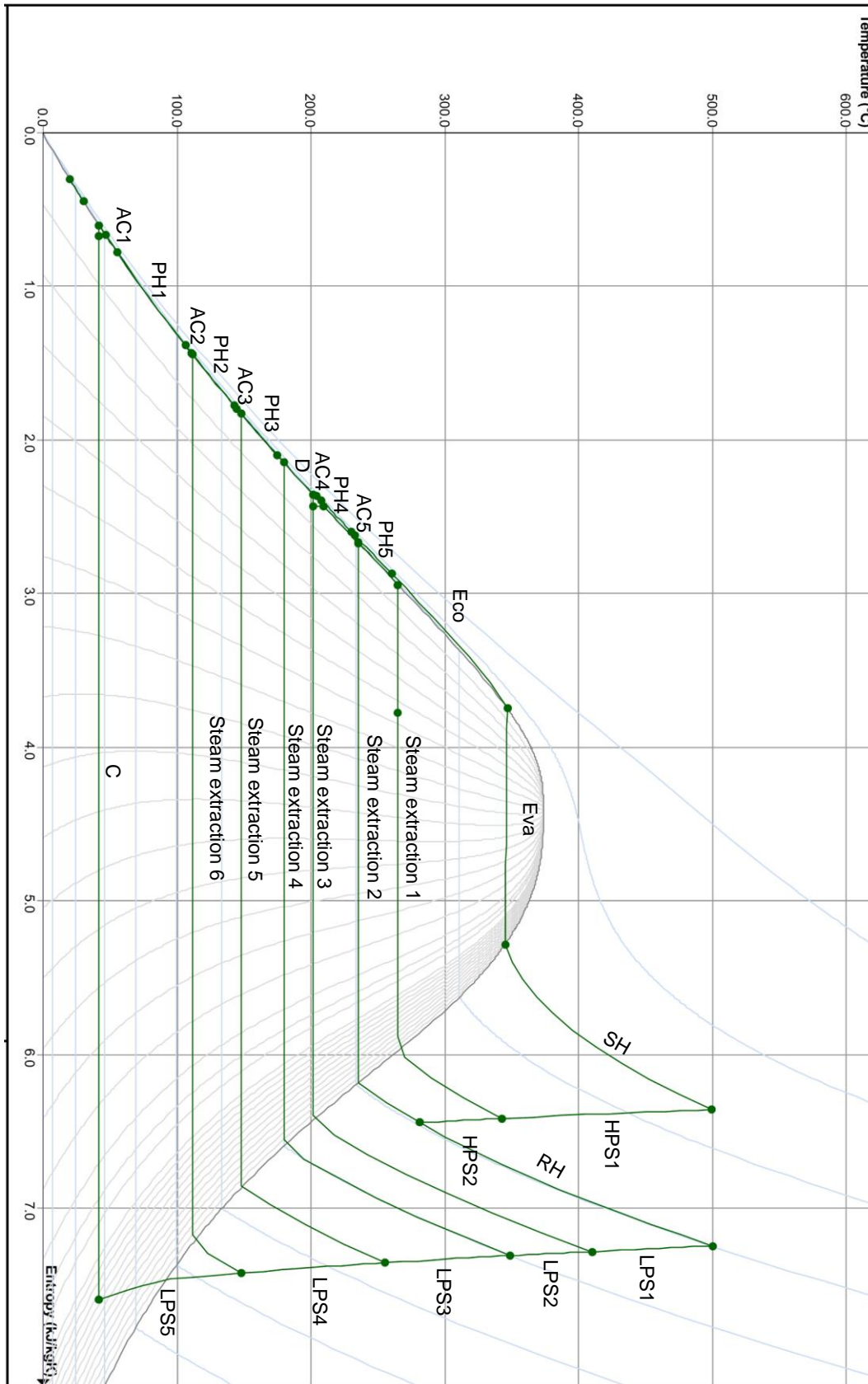
Appendix J: Schematic of the profile selection implemented in EbsScript

Appendix K: Matlab Script for LEC calculation

```matlab
%%
%_____
%Results of simulation

%Aperture area [m²]
A_ap = 1206437.76;
%Total area of the plant [km²]
A = 4.25170944;
%Design gross electrical output[MW]
Q_PB = 125000;
%Thermal capacity of the storage [kWhth]
C_sto = 2773085.681;
%Thermal energy from auxiliary heater [MWh]
Q_AH = 55000;
%Annual net electricity output produced solar [MWh]
Q_PB_e = 492282.4245;


%_____
%O&M Input

%Labor costs per employee [€/a]
C_p = 48000;
%Number of persons (without field maintenance) [-]
p = 30;
%Specific number of persons for field maintenance [1/1000m²]
a_p = 0.03;
%Annual O&M cost factor [-]
a_OM = 1;
%Total number of persons [-]
p_t = p + a_p*A_ap/1000;
%Specific water consumption [€/MWh]
a_w = 1.3;
%O&M Equipment costs percentage of investment [-]
a_equ = 0.01;


%_____
%Cost Input

%Specific investment cost for solar field [€/m²]
P_SF = 260;
%Specific investment cost for power block [€/kWhe]
P_PB = 720;
%Specific Investment cost for storage [€/kWhth]
P_Sto = 30;
%Specific land cost [€/m²]
P_A = 5;
%Gas cost [€/MWh]
P_g = 25;
%Annual insurance cost [-]
a_i = 0.003;
%Life time [years] [-]
n = 25;
%Dept interest rate [-]
k = 0.08;
%Surcharge for construction [-]
a_c = 0.2;


%_____
%Cost Output (fix parameters)

%Investment land [€]
L = A*1000*1000*P_A;
%Annual O&M costs [€]
OM_fix = (p_t*C_p + Q_PB_e*a_w + P_g*Q_AH);

%%
```

```
%_____
%Monte Carlo simulation

%number of iterations
i= 1000000;

%Initialise vector for LECs
LEC = zeros( 1,i);
%res = zeros(1,i);


%i iterations to calculate LEC
for j=1:i
%normal distributed
P_PB = 720 + 72*randn/2.576;

%equally distributed
n = 20 + (30-20)*rand(1);
k = 0.06 + (0.12-0.06)*rand(1);
P_SF = 220 + (350-220)*rand(1);
P_Sto = 30 + (40-30)*rand(1);
a_c = 0.2 + (0.3-0.2)*rand(1);
a_equ = 0.005 + (0.02-0.005)*rand(1);
a_i = 0.002 + (0.004-0.002)*rand(1);

%calculate Data
CRF = (k * (1+k)^n) / ( (1+k)^n -1);
SF = P_SF*A_ap;
PB = P_PB*Q_PB;
ST = P_Sto*C_sto;
I = (1+a_c)*(L+ST+PB+SF);
OM = OM_fix + a_equ*I;

LEC(j) = (I*(CRF+a_i) + OM)/(Q_PB_e*1000);
%Calculate residuals
%{
for k=3:j
    res(j) = res(j)+LEC(k);
end
res(j)=res(j)/(k-3);
res(j-2)=res(j-1)-res(j);
%}
end
%%
%%_____
%Plot result of LEC calculation

%Calculate mean LEC
mean_LEC = mean(LEC);

%Calculate mode LEC
x=min(LEC):0.001:max(LEC);
y = ksdensity(LEC,x);
[val, row] = max(y);
LEC_most_probable = x(row);

%comulative density function (cdf)
y = ksdensity(LEC,x,'function','cdf');

%plot function
plot(x,y, 'r','LineWidth',2);
xlabel('LEC [€/kWhe]');
ylabel('comulative density function (cdf) [-]');
axis([min(LEC) max(LEC) 0 max(y)]);
legend('comulative density function (cdf)','location','NorthWest');
```

Appendix L: Parameters of the reference solar thermal power plant

Parameters of the simulation	
Residuals	10^{-7}
Maximum iterations	500
Calculation mode	Off-design
Time step (Comp 119)	10 s
Frequency of instationary calculations (Comp 119)	At every 2nd iteration step
User input parameters to design the solar field and the power block	
Parameters for the design point of the SF	
Location	Las Vegas
T_amb_design	30° C
DNI_design	850 W/m²
Date_design	21.06.2010
Parameters for solar field layout	
loops	8
SM	2.2
PTC_type	EuroTrough + PTR 70
PTC_loop	4
W_PP	150 m
D_u_pipe	50 m
S_u_pipe_f1	10 m
S_u_pipe_f2	9 m
S_u_pipe_h	6 m
Parameters for pipe design	
Heat_losses_pipe	200 W/m²
V_Design	2.5 m/s
KS	0.1 mm
Parameters for the storage system used in Chapter 3.1.6	
Storage_time	10 h

Delta_T_tank	1.1 K
Hot_Tank_Design_Temp	510° C
Cold_Tank_Design_Temp	310° C

Parameters to design the auxiliary heater	
Load_AH	0.3

Parameters for the transient simulation	
t_feeder	71 mm

Parameters for the PB	
Gross_capcity	125 MW
P_turbine_pack_pressure	0.08 bar

User input parameters for plant operation management	
Simulation mode	
ts_tsc	600 s
Forecast_Timesteps	2
Mode_SF	1
Mode_H	1

Pseudo-transient behavior of the PB, described in Chapter 3.2.6	
d_SMF_d_t	0.166 kg/s/s
Delta_t_startup	0.5 h

Parameters to identify the weather conditions of a day, described in Chapter 3.3	
Min_DNI_PB	300 W/m²
DNI_bad_day	500 W/m²
DNI_very_good_day	800 W/m²

Parameters to identify whether power block can operate, described in Chapter 3.3	
Min_HT_Level_PB_OP	0.04
Min_HT_Level_bad_day	0.3
Min_HT_Level_good_day	0.1
Min_HT_Level_very_good_day	0.04
Min_HT_Level_Day_AH	0.013
Min_HT_Level_Night_AH	0.013

Parameters to identify whether solar field can operate, described in Chapter 3.3	
Min_Salt_M	150 kg/s

Further parameters for plant operation management, described in Chapter 3.3

Hot_Tank_Low_Temp	485° C
Salt_Low_Temp	270° C

Design output parameters

Parameters of the SF capacity

M_tank	33,555 t
C_tank	2,7436,049 kWh
SM_real	2.233

Salt mass flow in design point

SMF_PB_Design	914 kg/s
SMF_SF_Design	2,180 kg/s
SMF_Aux_Design	253 kg/s

Geometric parameters of the SF

L_Feeder_1	537 m
L_Feeder_2	928 m
Nbranch	22
L_Header	893 m
A	4.25 km²
W_O	1,520 m
N_S	2,796 m
Aperture_Area	1.21 km²

Efficiency parameters (at design point)

Gross_eff_SF	67.204 %
Net_eff_SF	67.198 %
Gross_eff_PB	44.251 %
Net_eff_PB	43.862 %
Gross_eff_PP	29.738 %
Net_eff_PP	29.474 %

Pressure drops in the piping elements

P1	0.842 bar
P2	1.962 bar
H1	6.478 bar

C1	0.495 bar
C2	0.472 bar
C3	0.459 bar
C4	0.455 bar
P3	0.5 bar
H2	5.539 bar
P4	1.830 bar
P5	0.786 bar

Heat transfer coefficients in indirect storages	
IS1	2,245 W/m²/K
IS2	2,500 W/m²/K
IS3	2,684 W/m²/K
IS4	2,812 W/m²/K
IS5	3,718 W/m²/K
IS6	3,414 W/m²/K
IS7	3,133 W/m²/K

Discretization of indirect storages (X, Y)	
IS1, IS2, IS3, IS4	(10, 1)
IS5	(15, 1)
IS6	(20,1)
IS7	(20,1)

Steel masses in indirect storages	
IS1, IS2, IS3, IS4	0.750 t
IS5	44.569 t
IS6	66.874 t
IS7	54.443 t
Total	1,789 t

HTF masses in indirect storages	
IS1, IS2, IS3, IS4	3.648 t
IS5	55.231 t
IS6	220.012 t
IS7	254.638 t

Total	3,115 t
Heat transfer coefficients in steam generator	
Eco	
Primary	8,650 W/m²/K
Secondary	2,100 W/m²/K
Eva	
Primary	49,100 W/m²/K
Secondary	2,400 W/m²/K
SH, RH	
Primary	3,750 W/m²/K
Secondary	2,775 W/m²/K
Heat transfer areas in steam generator	
Eco	1,322 m²
Eva	1,145 m²
SH	1,243 m²
RH	3,045 m²
Economical parameters (Matlab script shown in Appendix K	
P_{gas}	25 €/MWh
$a_{Insurance}$	0.002-0.004 (uniformly distributed)
n_{em}	30
$a_{SF,maintance}$	0.030 1/1000 m²
P_{em}	48,000 €/a
P_{water}	1.30 €/MWh
$a_{equipment}$	0.005 – 0.02 (uniformly distributed)
$a_{indirect}$	0.2 – 0.3 (uniformly distributed)
P_{PB}	720 €/kWh$_{el}$ (normally distributed – 99% of values within ±72 €/kWh$_{el}$)
P_{SF}	200 - 350 €/m² (uniformly distributed)
P_S	30 – 40 €/kWh$_{th}$ (uniformly distributed)
P_{land}	5 €/m²
a_{dis}	0.06 – 0.12(uniformly distributed)
n	20 - 30 (uniformly distributed)

Appendix M: The location used for the simulation of the solar thermal power plant

The following criteria are defined for the location's weather data set:

- Direct normal irradiation averaged annual sum at least 2000 kWh/m²/y

- Availability of solar data, especially for direct normal irradiation and dry bulb temperature of at least ten minutes' resolution over one year

Almaría in Spain and Las Vegas in the United States of America fulfil these criteria, as detailed in the following section.

Figure 37 shows the worldwide annual direct normal irradiation in kWh/m²/y. The two selected locations are indicated on the map. Almería is located in an area with annual direct normal irradiation of between 2001 to 2200 kWh/m²/y, Las Vegas between 2401 to 2600 kWh/m²/y. Solar data for Las Vegas is provided by the NREL in one-minute resolution for the years 2007 to 2011 (NREL 2012), for Almería by the DLR in ten-minute resolution for the years 2001 to 2011.

Figure 38 shows a plot of the annual direct normal irradiation of Almería and Las Vegas. The average annual direct normal irradiation of Almería between 2002 and
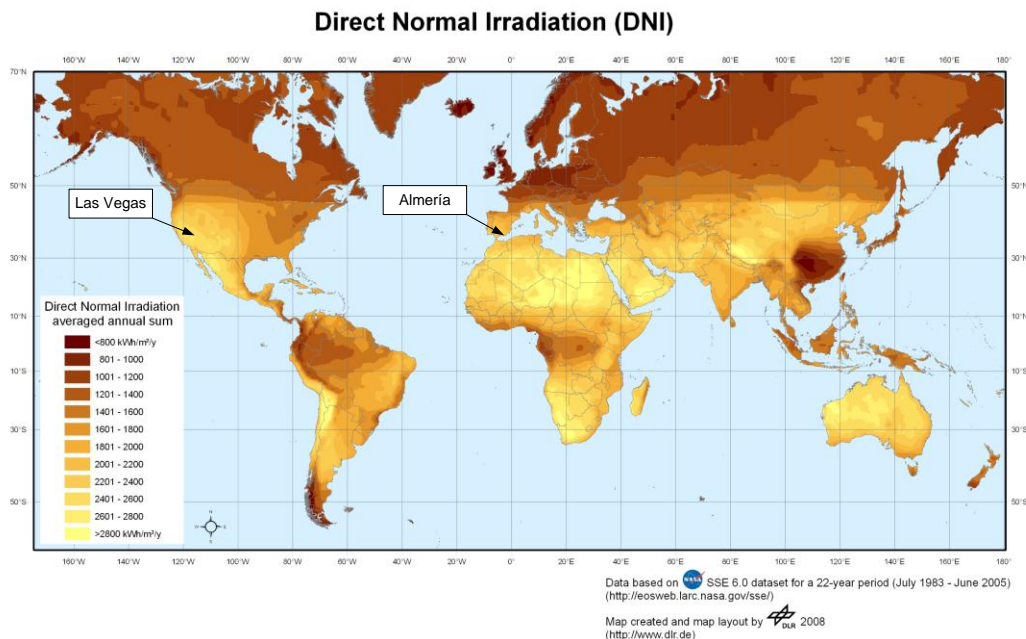
Figure 37: Worldwide annual direct normal irradiation in kWh/m²/y from NASA SSE 6.0 adapted from (Trieb 2009)

2011 is 2141.4 kWh/m²/y. In Las Vegas, the average is 2578.6 kWh/m²/y. To investigate the influence of various direct normal irradiation averaged annual sums, three years within the following DNI classes at these two locations are selected:

- Class 1: 2000 – 2100 kWh/m²/y → Almería (2010): 2095 kWh/m²/y
- Class 4: 2300 – 2400 kWh/m²/y → Almería (2005): 2300 kWh/m²/y
- Class 7: 2600 – 2700 kWh/m²/y → Las Vegas (2008): 2659 kWh/m²/y

A total of 25,729,646 km² of potential global sites for solar thermal power stations with average annual direct normal irradiation exceeding 2000 kWh/m²/y exist worldwide. However, only 25.5% of this area has irradiation higher than 2600 kWh/m²/y (Trieb 2009), much of it located in Africa, Australia, and the Middle East, as Figure 37 shows. This means that the 2010 Almería yield analysis results in correspond to a much larger area than those of the 2008 Las Vegas simulation.

The observation stations in Las Vegas (36.06°) and Almería (37.08°) lie on roughly the same geographical latitude in the northern hemisphere. Nevertheless, the two locations have different climates – Almería is Csa (warm temperate climate with dry and hot summer, also known as Mediterranean climate) and Las Vegas BWh (hot, arid desert climate) in the Köppen climate classification (Kottek 2006).
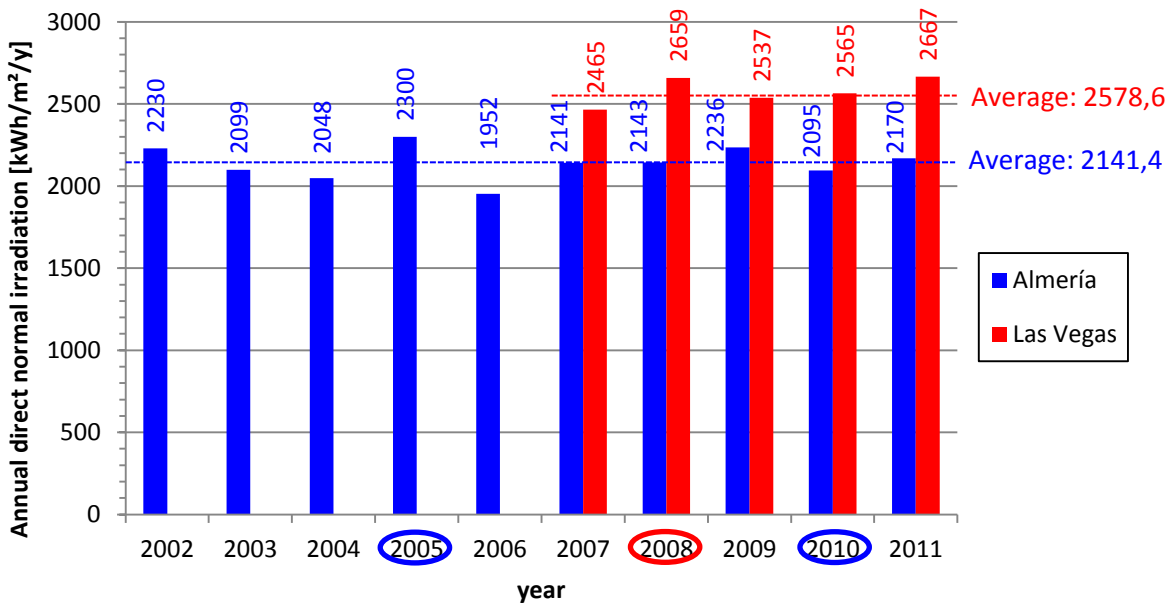
Figure 38: Annual direct normal irradiation for Almería from 2002 to 2011 and Las Vegas from 2007 to 2011

Table 13 shows the weather data (maximum, minimum, and average temperature and direct normal intensity) for the years 2005 and 2010 in Almería, and 2008 in Las Vegas. The annual average temperature in Las Vegas is almost 22° C, more than 5° C higher than in Almería. High ambient temperature causes lower thermal losses from pipes and storages.

Figure 39 and Figure 40 show the temperature course of 2010 in Almería and 2008 in Las Vegas. The x-axis shows the number of days and the y-axis the local time. A comparison of the two reveals that summer days in Las Vegas are hotter than those in Almería, and the temperature drop at night is lower. Lowest

Table 13: Maximum, minimum, and average weather data for the year 2010 in Almería and 2008 in Las Vegas

Location	year	DNI [W/m²]			Temperature [° C]		
		max	min	average	max	min	average
Almaría	2005	1077	0	263	40.8	-4.1	16.3
	2010	1033	0	239	41.7	-3.9	16.5
Las Vegas	2008	1026	0	302	44.2	-1.4	21.8
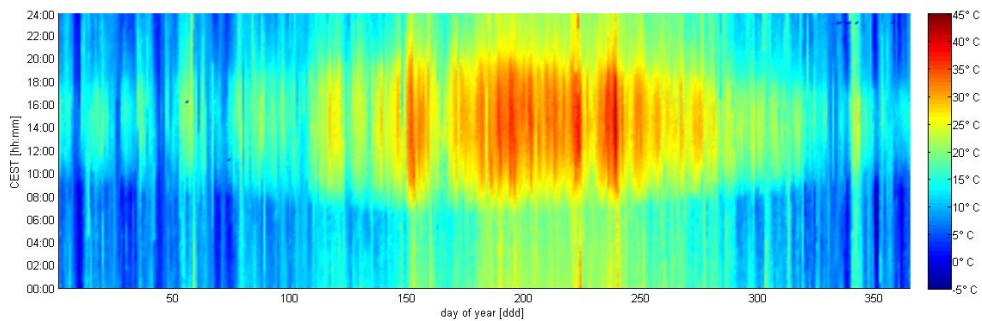
Figure 39: Temperature progress in Almería during 2010
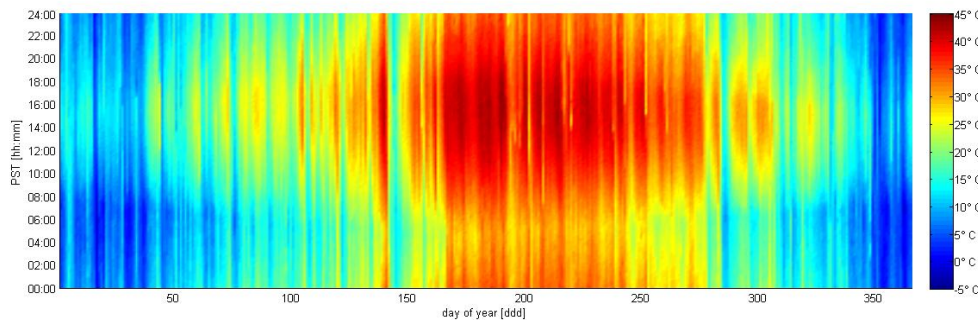
Figure 40: Temperature progress in Las Vegas during 2008

temperatures are always reached in the hour after sunrise. During June, July, and August, the temperature never falls below 18° C in Las Vegas, while it drops as low as 12° C in Almería. The average temperature in the two regions during the months of December, January, and February is comparable – 9.6° C in Almería and 9.7° C in Las Vegas. Almería suffers the lowest temperatures (-4° C).

Figure 41 and Figure 42 show the course of the direct normal radiance of 2008 in Las Vegas and 2010 in Almería. During 2008, Las Vegas had only six days of maximal direct normal irradiance of less than 300 W/m², whereas Almería had 22 during 2010. These days appear in the figures as blue vertical lines. During such days, the PB cannot operate because the SF is unable to start-up. Figure 41 also shows many more blue dots and lines during daytime in Almería, which indicates clouding – in fact, direct normal irradiance remained below the 300 W/m² threshold for 38 % of daytime. In Figure 42, the blue area during daytime is smaller – Las Vegas fell below the threshold for only 24 % of daytime.
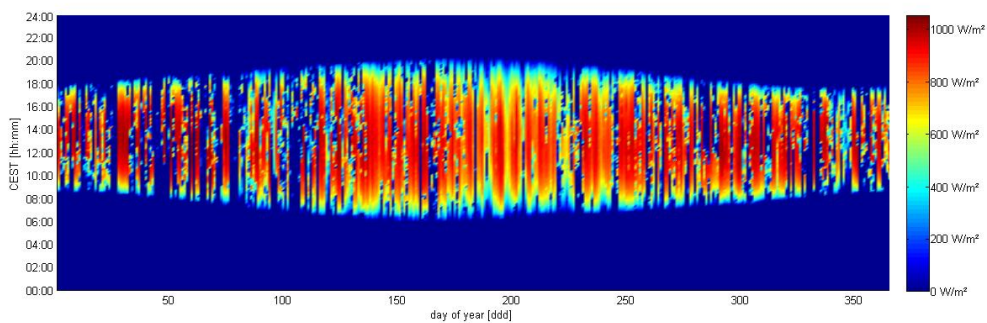
Figure 41: Direct normal radiance progress in Almería during 2010
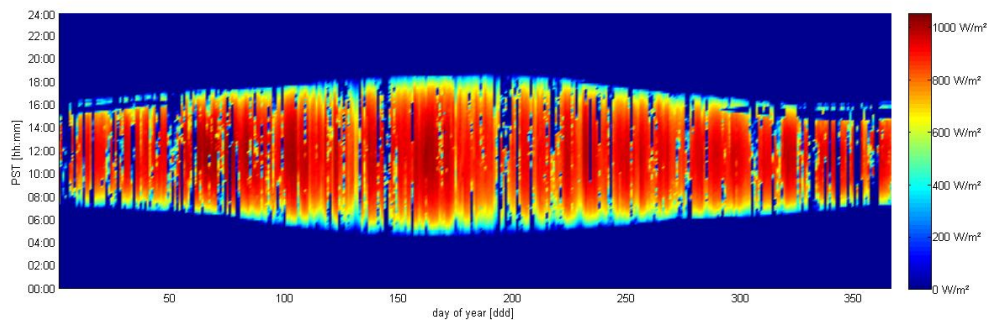
Figure 42: Direct normal radiance progress in Las Vegas during 2008

Appendix N: Effect of the time discretization on the PTC efficiency

As described in Chapter 4.4, the effective heat input into the PTCs falls with larger time series time steps (TSs) by 0.03%, 0.13%, to 1.13% (15-, 30-, 60- minute discretization). The effect of the direct normal irradiation discretization error is outlined in Chapter 4.4. This appendix outlines the discretization error of the PTC efficiency, which is also increased by higher TSs.

Figure 43 a) shows the PTC efficiency during 2008 in Las Vegas. Highest efficiency (as high as 75.3%) is achieved during June. During December, efficiency reaches only 54.6%. Three days have been chosen: the summer solstices in the northern hemisphere (June 21) and in the southern hemisphere

a)

b)
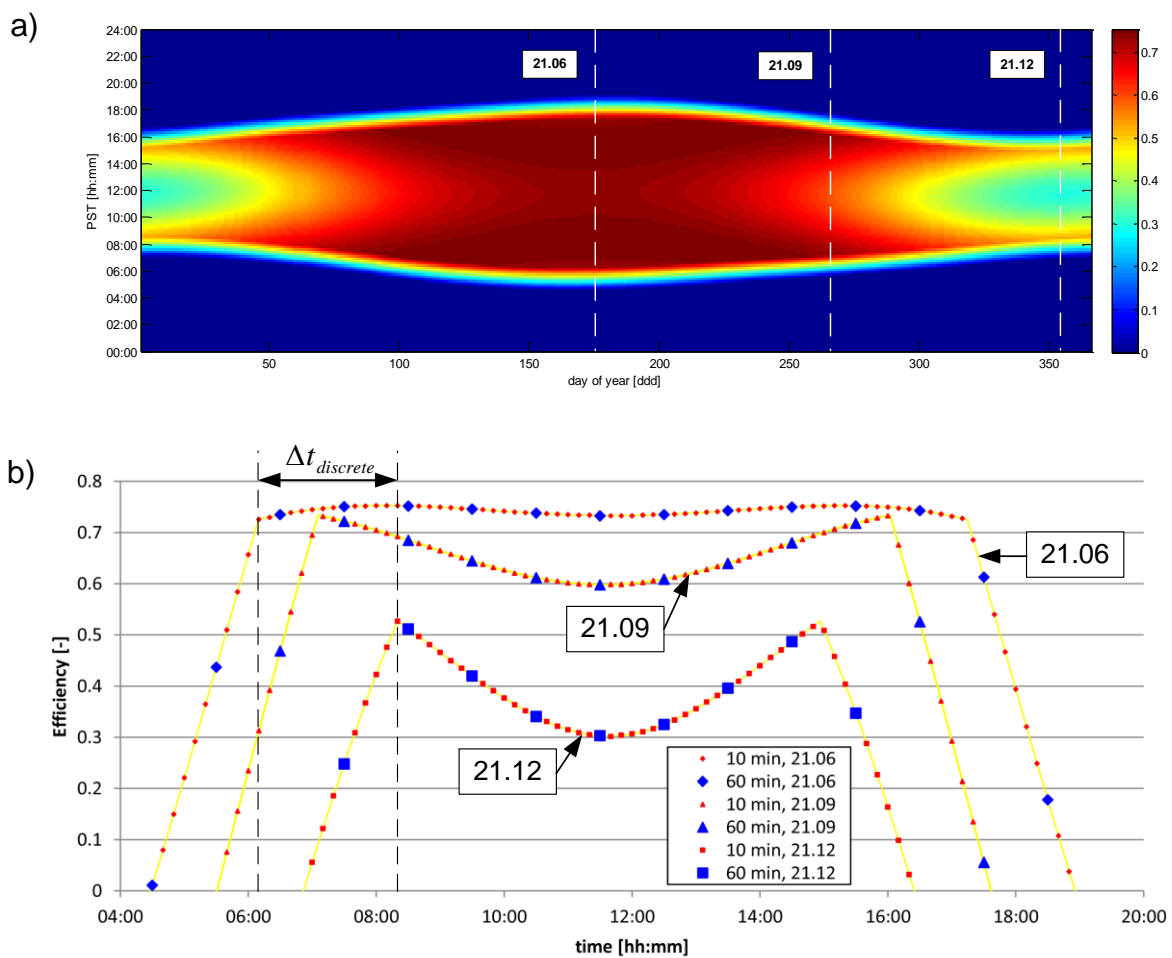
Figure 43: PTC efficiency a) over one year, and b) over three selected days (21.06, 21.09, 21.12)

(December 21), and September 21. These days are shown in Figure 43 b). The 10-minute discretization is marked red, the 60-minute discretization blue.

The 60-minute discretization error on these days is -0.32%, -1.29%, and -0.46% (June 21, September 21, and December 21), and +0.011%, -0.017%, and +0.028% (June 21, September 21, and December 21) for the 10-minute discretization, compared to the integral of the PTC efficiency over one day, calculated with a one-second discretization (the yellow line in Figure 43 b)). The discretization error on these days is nearly zero with the 10-minute discretization and the simulation can therefore be assumed to be exact. The main PTC efficiency discretization error with the 60-minute discretization is located next to the two discrete points in the efficiency plot. These points are at 08:23 and 14:53 (December 21), 07:06 and 16:01 (September 21), and 6:09 and 17:13 (June 21).

To investigate the PTC efficiency discretization error in detail, the efficiency plot of December 21 is fitted by two fifth-order polynomal functions. One function reflects the PTC efficiency between sunrise and the first discrete point (08:23), and the second from this discrete point to the local minima at 11:38. The rest of the day from this minima to sunset is calculated by reflecting the two functions on the y-axis.

A Monte Carlo simulation is performed, as explained in Chapter 3.4.2. The input value of the Monte Carlo simulation is the first discretization time instant

$$t_{0,j} = t_{sunset} + \Delta t_k, \quad \Delta t_k = 1, 10, 15, 30, 60 \text{ min} \tag{100}$$

that is varied between the minimum value ($t_{0,j}=t_{sunset}$), and the maximum value ($t_{0,j} = t_{sunset} + \Delta t_k$). The output of the Monte Carlo simulation is the PTC efficiency integral over the whole day, and the mean value of the PTC efficiency. According to the central limit theorem, stated in Eq.(79), the mean value of the PTC efficiency must be asymptotic given an infinite number ($n \rightarrow \infty$) of simulations and independent of the discretization of time. The number of simulations has been chosen to reach a residual of the mean efficiency of 10^{-7} in order to calculate the resultung cdf. The desired residuals were reached within 100 (1 minute), 1,000 (10-minute discretization), up to 1,000,000 iterations (60-minute discretization). In all, the convergence is slower with increasing discretization of time. The resulting

cdf of this simulation for the 1-minute (yellow line), 10-minute (orange line), 15-minute (green line), 30-minute (blue line), and 60-minute (red line) discretizations is shown in Figure 44. The distribution of the 1-minute discretization is not visible in this diagram resolution, so it can be assumed to be the mean efficiency value.

The probability of underestimating the PTC collector efficiency is 53.5% (60-minute resolution), 20.0% (30-minute resolution), 38.8% (15-minute resolution), and 50.3% (10-minute resolution). On this day, the 30-minute discretization has the highest probability of overestimating the collector efficiency, whereas the 60-minute discretization has the lowest. This is the results of the time difference between the first indiscrete point at 08:23 and the second at 14:53, which is exactly 6.5 hours. This time difference is divisible by the 10-, 15-, and 30-, but not by the 60-minute discretization. The possibility of overestimating the PTC efficiency is therefore higher for the 10-, 15-, and 30-minute discretizations. If one discretization point is exactly on or near the discrete point in the efficiency function, another point of discretization is also on or near the other discrete point. This results in an overestimation of the PTC efficiency. Therefore many calculated PTC efficiencies are overestimated, which can be seen in the nearly vertical steps in the cdfs of the 10-, 15-, and 30-minute discretization.
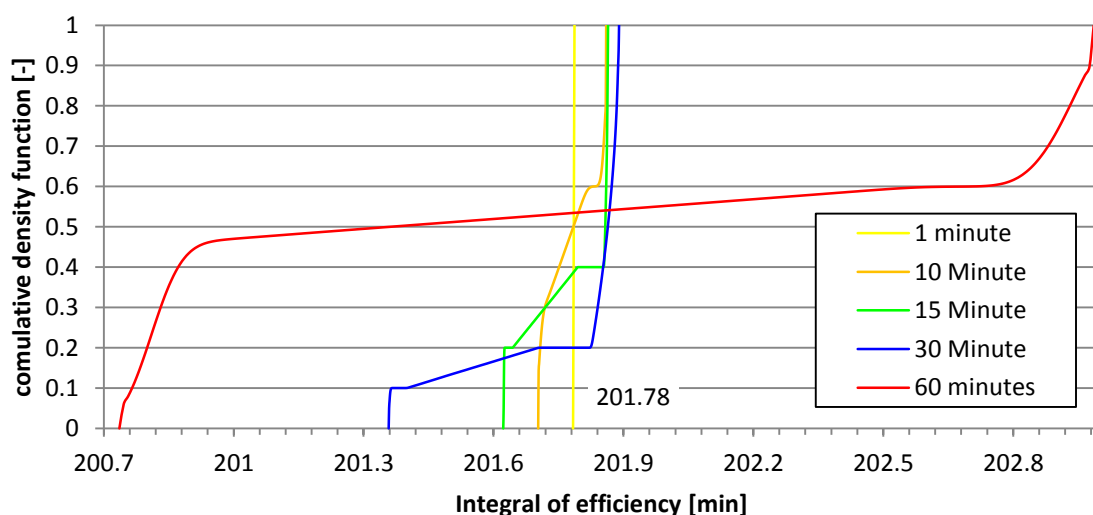
Figure 44: CDF for the PTC efficiency integral over the day of December 21 – efficiency is discretized in 1-, 10-, 30-, and 60-minute resolution

Figure 43 introduces the time interval between the discrete point of June 21 and September 21. High probability of PTC efficiency overestimation is therefore given for a maximum of

$$[n] = \frac{\Delta t_{discret}}{2\Delta t_k}, \quad \Delta t_k = 1, 10, 15, 30, 60 \text{ min} \qquad (101)$$

times during the entire year. The time interval $\Delta t_{discret}$ is 130 minutes in the 2008 Las Vegas simulation. A high probability of PTC efficiency is therefore given for 13-14 times, 8-9 times, 3-4 times, and 1-2 times (10-, 15-, 20-, 30-, and 60-minute discretization) over the entire year. The probability that the maximum number of PTC efficiency overestimations from Eq.(101) will occur increases as the time

$$t_{min} = min|\Delta t_{discret} - j\Delta t_k|, \quad \Delta t_k = 1, 10, 15, 30, 60 \text{ min, } j \in \mathbb{N} \qquad (102)$$

decreases. This time is 0, 5, 10, and 10 minutes (10-, 15-, 30-, and 60-minute discretization), but at most $\Delta t_k/2$, and therefore increased by higher TSs.

Even without exact mathematical proof, it can be stated that there is a tendency for the solar heat input into the PTC to decrease with increased TSs. As stated in Chapter 4.4, heat input is decreased by the DNI discretization error. Secondly, the probability of overestimating PTC efficiency is lower with higher TSs. The convergence to the real mean PTC efficiency is also slower with higher TSs. Residuals of 10^{-7} were not reached within 365 simulations for the examined day, December 21.

Appendix O: Absolute value comparison of for 10-, 15-, 30-, and 60-minute time series time step

Value	10 minutes	15 minutes	30 minutes	60 minutes
Annual energy flows [GWh$_{th}$]				
Q_sun	3057.2	3057.2	3057.2	3057.2
Q_PTC_eff	1849.5	1848.9	1845.7	1832.6
Q_loss	327.8	328.4	331.6	341.3
Q_HT	1406.7	1394.1	1338.5	1246.4
Q_CT	-34.5	-27.0	15.9	100.8
Q_SF	1372.2	1367.0	1354.5	1347.2
Q_PB	1415.5	1411.3	1403.5	1376.4
Q_PB_e_gross	598.4	596.3	592.2	579.1
Q_PB_e_net	573.4	571.3	566.7	551.9
Efficiency [-]				
PTC_eff	60.50	60.47	60.37	59.94
SF_gross	44.88	44.71	44.30	44.07
PB_gross	42.27	42.25	42.19	42.07
PB_net	40.51	40.48	40.38	40.10
PP_gross	19.57	19.50	19.37	18.94
PP_net	18.76	18.69	18.54	18.05
Parasitics [GWh$_e$]				
PB	12.2	12.2	12.0	11.7
SF	12.6	12.7	13.2	13.6
Average tank temperature [° C]				
Hot tank	505.7	505.4	504.6	503.7
Cold tank	311.6	312.2	314.8	322.2
PB operation mode [%]				
On	57.9	57.7	57.0	56.1
Design	93.1	92.7	91.9	85.7
Off-design	6.9	7.3	8.1	14.3

Appendix P: Sankey diagrams of the Almería 2005, Almería 2010, and Las Vegas 2008 improved simulation
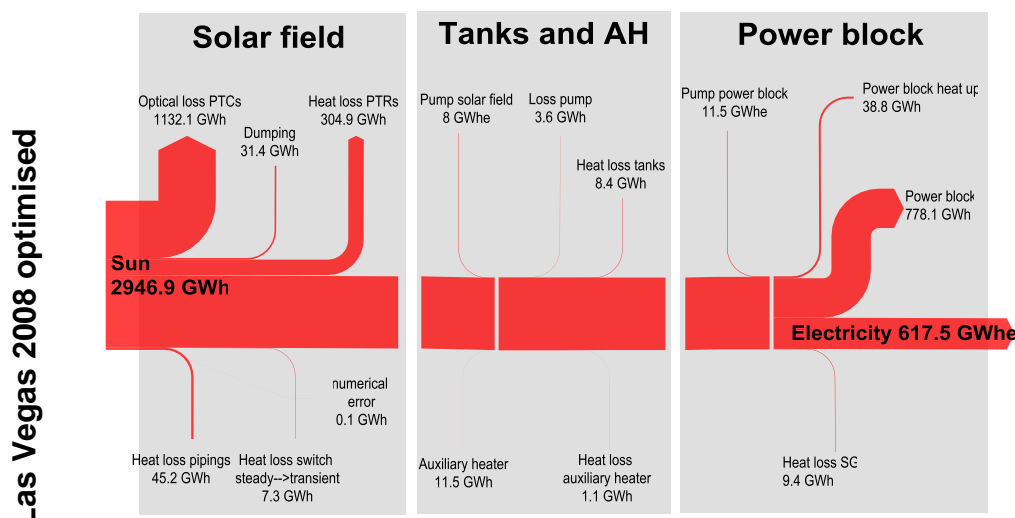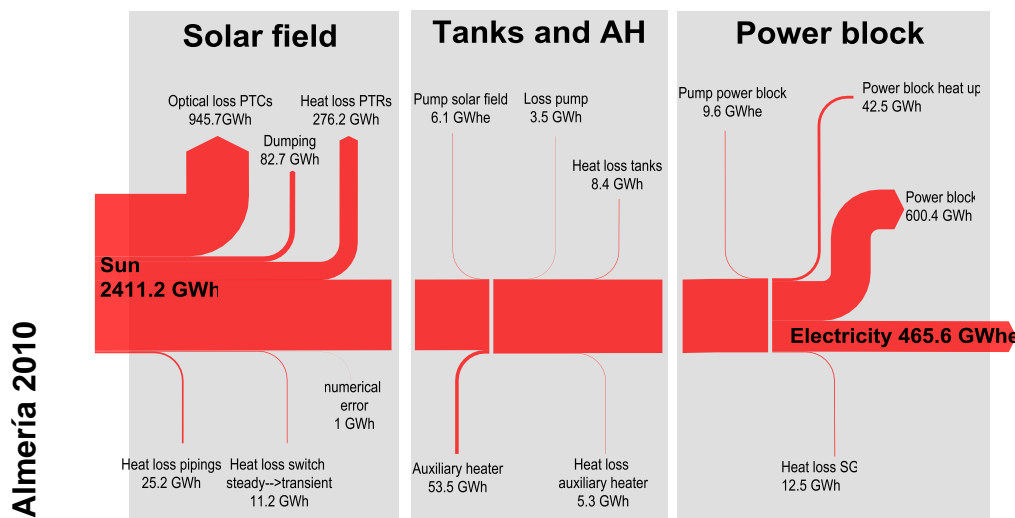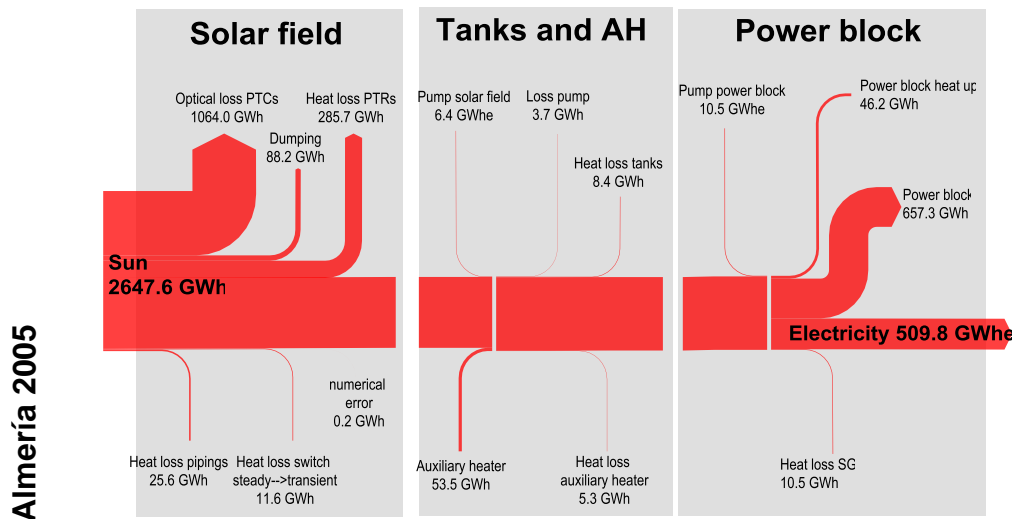
Appendix Q: Ethical impact of steam turbine back-pressure in solar thermal power plants

While lying on the shore next to a lake on a hot summer day and enjoying the sun, you can feel its power. The sun is the reason for all life on earth. Without it, the earth would be a desolate ice planet. Nearly all energy that the human race consumes, except for tidal power, geothermal power, and nuclear power, comes from the sun. The sun evaporates water and keeps rivers running. Its energy flow is converted into electricity by hydro power stations. The temperature gradients on earth keep the wind blowing constantly, and its energy is converted into electricity by wind turbines. The wind itself forms ocean waves whose energy can be used to produce electricity. The photosynthesis that takes place in nearly all plants depends on the sun, whose energy humans consume as food, gas, oil, or coal. One of the purest forms of electricity production may be to use the power of the sun directly. This can be done either by photovoltaic or by solar thermal power plants, such as the ones this thesis describes.

Chapter 4.1 contains the details of such a power station. The turbine back pressure of this system is assumed to be 0.08 bar when equipped with a wet cooling system. The water consumption of such a system is relatively high at 2200 to 3400 litres per MWh_{el} (California Energy Commission 2002, p. 2-5). Dry cooling system water consumption is approximately 5% of the wet cooling system level (California Energy Commission 2002, p. 1-9). The disadvantages are that dry cooling systems have higher installation costs, site space usage, steam turbine load limits on very hot days, and efficiency penalties (California Energy Commission 2002, p. 2-9)of between 5% to 20%. Chapter 4.7 shows that the most likely costs of a solar thermal power station with molten salt as a heat transfer fluid and a dry cooling system are 2 cents per produced kilowatt hour of electric power higher than the reference plant's LECs.

As stated in the report "Perspectives on a Sustainable Power System for EUMENA" referenced in Chapter 1, the CSP capacity will rise until 2050, mostly in regions with high solar radiation, such as the Middle East and North Africa. These regions in particular suffer water shortages, which will be even greater in the

future. The report "Feeding a Thirsty World – Challenges and Opportunities for a Water and Food Secure Future" (Jägerskog 2012) states that by 2050 there will not be enough water available worldwide to water current cropland if we follow our current diet of 3,000 kcal per day and 20% animal food. This dilemma can only be solved if animal food is reduced to 5% and nations engage in virtual water transfer, which involves food from water-rich countries being exported to water-poor countries (Jägerskog 2012, p.14ff). Facing the water problem as it affects feeding the world's future population will meant the intensification of controversy over water usage in energy generation in the future.

Although solar energy seems to be the purest energy available on the market and is considered to be the future "green" energy, its effects on water usage require consideration. Water shortages will be a major future issue. Along with the food vs. biofuel conflict, the main future conflict will be water vs. energy. At an electric consumption of about 2000 kWh per person and year, the annual electricity cost per person would increase by 40 € if a water-reduced cooling system for the solar thermal reference plant would be used. The question will be whether the consumer will be willing to pay more for electric power in order to realize solar thermal power stations with reduced water consumption.

References

Archimede Solar Energy: ASE receiver tube datasheet: http://www.archimedesolarenergy.com/hems11_en.pdf, retrieved August 2, 2012.

Baudis, Ulrich: Technologie der Salzschmelzen. Wärmebehandlung, Härtetechnik, Wärmeübertragung, Reinigung, Landsberg/Lech 2001.

Benmarraze, Marc M. et al.: Hazard issues in parabolic trough technology using molten salt & synthetic oil with regard to oxiding and toxicity properties - SolarPaces 2010 2010, Procedings of SolarPaces2010 conference, September 21-24th 2010, Perpignan, France.

Benz, Nikolaus: Parabolrinnenkollektoren: Feldtest, Optimierung und Weiterentwicklung von Receivern (PARFOR) 2008.

Beurskens, L.W.M et al.: Renewable Energy Projections as Published in the National Renewable Energy Action Plans of the European Member States: http://www.eea.europa.eu/data-and-maps/figures/national-renewable-energy-action-plan-1/nreap_2011.pdf, retrieved August 15, 2012.

Boerema, Nicholas et al.: Liquid sodium versus Hitec as a heat transfer fluid in solar thermal central receiver systems. in: Solar Energy, Vol. 86 (2012), S. 2293–2305: http://www.sciencedirect.com/science/article/pii/S0038092X12001703.

Bradshaw, R. W.; Meeker, D. E.: High-temperature stability of ternary nitrate molten salts for solar thermal energy systems. in: Solar Energy Materials, Vol. 21 (1990), S. 51–60: http://www.sciencedirect.com/science/article/pii/016516339090042Y.

Bradshaw, R.W; Carling, R.W: A review of the chemical and physical properties of molten alkali nitrate salts and their effect on materials used for solar central receivers, United States of America 1987.

Burgaleta, Juan Ignacio et al.: Gemasolar, the first tower thermosolar commercial plant with molten salt storage 2011, Proceedings of SolarPaces2011 conference, September 20-23th 2011, Granada, Spain.

Burkholder, F.; Kutscher, C.: Heat Loss Testing of Schott's 2008 PTR70 Parabolic Trough Receiver 2009: http://www.nrel.gov/docs/fy09osti/45633.pdf, retrieved July 25, 2012.

California Energy Commission: Comparison of Alternative Cooling Technologies for California Power Plants. Economic, Environmental and Other Tradeoffs 2002: http://www.energy.ca.gov/reports/2002-07-09_500-02-079F.PDF, retrieved July 25, 2012.

Coscia, K. et al.: The heat transfer characteristics and phase modeling of molten binary nitrate salt systems (2011), retrieved 22.08.2012, Proceedings of SolarPaces2011 conference, September 20-23th 2011, Granada, Spain.

Crescenzi, T. et al.: Italian research on Concentrated Solar Power: http://www.enea.it/it/internazionali/eventi-internazionali/enea-in-japan-2011/energy/crescenzi.pdf, retrieved August 8, 2012.

Deutsches Zentrum für Luft- und Raumfahrt: DLR Portal - News-Archiv - Solarkraftwerke: Flüssiges Salz wird als Wärmeträgermedium getestet: http://www.dlr.de/dlr/desktopdefault.aspx/tabid-10202/334_read-742/, retrieved July 25, 2012.

Dii GmbH: Desert Power 2050: Dii - Bringing the Desertec vision into reality: http://www.dii-eumena.com/de/desert-power-2050.html, retrieved August 15, 2012.

Dow Chemical Company: Dowtherm_A_GA: http://msdssearch.dow.com/PublishedLiteratureDOWCOM/dh_08a5/0901b803808a5b98.pdf?filepath=heattrans/pdfs/noreg/176-&fromPage=GetDoc, retrieved August 10, 2012.

Drouot, L.P; Hillairet, M.J: The Themis program and the 2500-KW Themis solar power station at Targasonne. in: Journal Name: J. Sol. Energy Eng.; (United States); Journal Volume: 106:1, Vol. 1984, S. Medium: X; Size: Pages: 83-89.

ENEA: Solar thermal energy production: Guidelines and future programmes of ENEA 2007: http://www.solaritaly.enea.it/Documentazione/Solar%20Thermal%20Energy%20Production.pdf, retrieved August 7, 2012.

ENEL: At Priolo ENEL Inaugurates the "Archimede" Power Plant: http://www.enel.com/eWCM/salastampa/comunicati_eng/1634858-1_PDF-1.pdf, retrieved August 8, 2012.

NREL: Concentrating Solar Power Commercial Application Study: Reducing Water Consumption of Concentrating Solar Power Electricity Generation 2009: http://www1.eere.energy.gov/solar/pdfs/csp_water_study.pdf, retrieved August 29, 2012.

European Parliament, Council: Renewable Energy Road Map. Renewable energies in the 21st century: building a more sustainable future 2007: http://eur-lex.europa.eu/LexUriServ/LexUriServ.do?uri=CELEX:32009L0028:en:NOT, retrieved July 30, 2012.

European Parliament, Council: Directive 2009/28/EC of the European Parliament and of the Council of 23 April 2009. on the promotion of the use of energy from renewable sources and amending and subsequently repealing Directives 2001/77/EC and 2003/30/EC 2009: http://eur-lex.europa.eu/LexUriServ/LexUriServ.do?uri=CELEX:32009L0028:en:NOT, retrieved July 30, 2012.

Falchetta, M.: Control and Automation of the Archimede Molten Salt Operated Solar Field 2009a, Proceedings of SolarPaces2009 conference, September 15-18th, 2009, Berlin, Germany.

Falchetta, Massimo et al.: Design of the archimede 5 MW molten salt parabolic trough solar plant 2009b, Proceedings of SolarPaces2009 conference, September 15-18th, 2009, Berlin, Germany.

Falchetta, Massimo et al.: Commissioning of the Archimede 5 MW molten salt parabolic trough solar plant 2010, Proceedings of SolarPaces2010 conference, September 21-24th, 2010, Perpignan, France.

Flagsol: Parabolrinne - Flagsol GmbH: http://www.flagsol.com/flagsol/deutsch/technologie/solarthermische-kraftwerke/parabolrinne/index.html, retrieved July 25, 2012.

Frommhold, Hanns; Fleischmann, Hans Dieter: Wohnungsbau-Normen. Normen, Verordnungen, Richtlinien, 25. Aufl., Berlin 2008.

Gaggioli, Walter: Studio dell'impiego delle tecnologie di processo a sali fusi e del solare termodinamico a concentrazione ad alta temperatura, sviluppate dall'ENEA, in sistemi trigenerativi di piccola-media taglia asserviti a processi termici in applicazioni civili e industriali, Rom 2007.

Geyer, Michael et al.: EuroTrough - Parabolic Trough Collector Developed for Cost Efficient Solar Power Generation 2002, Proceedings of SolarPaces2002, September 4-6th, 2002, Zurich, Switzerland.

Grote, Karl-Heinrich; Feldhusen, Jrg: Dubbel, New York 2007.

Price, Hank et al.: Advances in Parabolic Trough Solar Power Technology. in: Journal of Solar Energy Engineering, Vol. 124 (2002), S. 109–125: http://link.aip.org/link/?SLE/124/109/1.

Hirsch, Tobias; Schenk, Heiko: Dynamics of oil-based parabolic trough plants - a detailed transient simulation model 2010, Proceedings of SolarPaces2010 conference, September 21-24th, 2010, Perpignan, France.

International Energy Agency: Guidelines for the economic analysis of renewable energy technology applications. Based on the findings of the International Energy Agency Workshop on the Economics of Renewable Energy Technologies, Chateau Montebello, Quebec, Canada, Paris, France, Washington, D.C 1991.

Jägerskog, A. Jønch Clausen: Feeding a Thirsty World – Challenges and Opportunities for a Water and Food Secure Future. Report Nr. 31. SIWI, Stockholm.: http://www.siwi.org/documents/Resources/Reports/Feeding_a_thirsty_world_2012 worldwaterweek_report_31.pdf, retrieved September 4, 2012.

Kearney, D. et al.: Evaluation of a Molten Salt Heat Transfer Fluid in a Parabolic Trough Solar Field. in: ASME Conference Proceedings, Vol. 2002 (2002), S. 293–299.

Kearney, D. et al.: Assessment of a Molten Salt Heat Transfer Fluid in a Parabolic Trough Solar Field. in: Journal of Solar Energy Engineering, Vol. 125 (2003), S. 170–176: http://link.aip.org/link/?SLE/125/170/1.

Kearney, D. et al.: Engineering aspects of a molten salt heat transfer fluid in a trough solar field. SolarPACES 2002. in: Energy, Vol. 29 (2004), S. 861–870: http://www.sciencedirect.com/science/article/pii/S0360544203001919.

Kelly, Bruce et al.: Adopting Nitrate/Nitrite Salt Mixtures as the Heat Transport Fluid in Parabolic Trough Power Plants. in: ASME Conference Proceedings, Vol. 2007 (2007), S. 1033–1040.

Klefenz, Günter: Die Regelung von Dampfkraftwerken, 2. Aufl., Mannheim, Wien, Zürich 1973.

Kottek, Markus et al.: World Map of the Köppen-Geiger climate classification updated. in: Meteorologische Zeitschrift, Vol. 15 (2006), S. 259–263.

Kramer, C. M.; Wilson, C. J.: The phase diagram of NaNO3—KNO3. in: Thermochimica Acta, Vol. 42 (1980), S. 253–264: http://www.sciencedirect.com/science/article/pii/0040603180850854.

Kuckelkorn, Thomas et al.: Advances in Receiver Technology for Parabolic Trough Collectors - A step forward towards higher Efficiency and longer lifetime 2009, Proceedings of SolarPaces2009 conference, September 15-18th, 2009, Berlin, Germany.

Lippke, Frank: Simulation of the part-load behavior of a 30 MWe SEGS plant 1995: http://www.osti.gov/bridge/purl.cover.jsp?purl=/95571-J2jgHW/webviewable/, retrieved August 13, 2012.

Maccari, Augusto: ENEA Activities on CSP Technologies: http://www.nrel.gov/csp/troughnet/pdfs/maccari_enea_trough_activities.pdf, retrieved July 24,2012.

Martini, Paolo: SolarPACES 2010 – HEMS08 Archimede Solar Energy Receiver Tube, designed for thermodynamic solar power plants operating high temperature (up to 550°C) with molten salts as Heat Transfer Fluid (HTF). 2010, Proceedings of SolarPaces2010 conference, September 21-24th, 2010, Perpignan, France.

Merziger, Gerhard: Formeln + Hilfen höhere Mathematik, 5. Aufl., Barsinghausen 2007.

Metzger, Christian: Bewertung der salzbasierten Parabolrinnentechnologie als solarthermisches Kraftwerkskonzept der nächsten Generation, Aachen 2010.

Meyer, Lutz et al.: Optimisation of the configuration of parabolic trough power plants in the range of 250 MW (2010), retrieved 21.08.2012, Proceedings of SolarPaces2010 conference, September 21-24th, 2010, Perpignan, France.

Mohr, M. et al.: Praxis solarthermischer Kraftwerke, Berlin; New York 1999.

NREL: MIDC/University of Nevada, Las Vegas (36.06 N, 115.08 W, 615 m, GMT-8): http://www.nrel.gov/midc/unlv/, retrieved July 23, 2012.

Pfleiderer, Carl; Petermann, Hartwig: Strömungsmaschinen, 7. Aufl., Berlin 2005.

Polifke, Wolfgang; Kopitz, Jan: Wärmeübertragung. Grundlagen, analytische und numerische Methoden, München 2005.

Pulyaev, Sergej: Untersuchung der instationären Prozesse im Kraftwerksbetrieb und deren Berücksichtigung in der Simulation mit EBSILON®Professional, Darmstadt 2011.

Raade, Justin W. et al.: Low melting point molten salt heat transfer fluid with reduced cost 2011a, Proceedings of SolarPaces2011 conference, September 20-23th, 2011, Granada, Spain.

Raade, Justin W.; Padowitz, David: Development of Molten Salt Heat Transfer Fluid With Low Melting Point and High Thermal Stability. in: Journal of Solar Energy Engineering, Vol. 133 (2011b), S. 31013.

Reilly, Hugh E.; Kolb, Gregory J.: An Evaluation of Molten-Salt Power Towers Including Results of the Solar Two Project 2001: http://www.osti.gov/energycitations/purl.cover.jsp?purl=/791898-6mGeQ8/native/, retrieved August 22, 2012.

Relloso, Sergio; Delgado, Emilio: Experience with molten salt thermal storage in a commercial parabolic trough plant. Andasol-1 commissioning and operation 2009,

Proceedings of SolarPaces2009 conference, September 15-18th, 2009, Berlin, Germany.

Ren, Nan et al.: Preparation and experimental study of molten salt with low melting point 2011, Proceedings of SolarPaces2011 conference, September 20-23th, 2011, Granada, Spain.

Schenk, Heiko; Eck, Markus: Yield analysis for parabolic trough solar thermal power plants - a basic approach 2012.

Schilling, Rudolf: Numerische Simulation realer Strömungen 2010.

Schott Solar CSP GmbH: Schott PTR 70 Receiver Setting the benchmark: http://www.schottsolar.com/no_cache/de/produkte/solarstromkraftwerke/schott-ptr-70-receiver/?cid=1692&did=568&sechash=9c45c72a, retrieved August 2, 2012.

Schweitzer, Axel et al.: Ultimate Trough® - the next generation collector for parabolic trough power plants 2011, Proceedings of SolarPaces2011 conference, September 20-23th, 2011, Granada, Spain.

Siemens AG: Presseinformation: Siemens errichtet solarthermische Testanlage in Portugal: http://www.siemens.com/press/pool/de/pressemitteilungen/2011/renewable_energy/ERE201102037d.pdf, retrieved August 9, 2012.

Solutia Inc.: Therminol VP-1 - Synthetic heat transfer fluid used during the vapor phase - North America: http://www.therminol.com/pages/products/vp-1.asp, retrieved August 10, 2012.

Steag EBSILON®Professional 2012.

Trieb, Franz et al.: Global Potential of Concentrating Solar Power 2009: http://www.dlr.de/tt/en/Portaldata/41/Resources/dokumente/institut/system/projects/reaccess/DNI-Atlas-SP-Berlin_20090915-04-Final-Colour.pdf, retrieved July 23, 2012.

VDI: VDI-Wärmeatlas, 10. Aufl., Berlin 2006.

Wagner, Walter: Wärmeträgertechnik. Mit organischen Fluiden, 7. Aufl., Würzburg 2005.

Wittmann, Michael et al.: Optimization of Molten Salt Parabolic Trough Power Plants using different Salt Mixtures 2012, Proceedings of SolarPaces2012 conference, September 11-14th, 2012, Marrakesch, Marokko.

Acknowledgment

von solarthermischen Kraftwerken abgebildet hat, und stets mit fachlichen Ratschlägen weiterhelfen konnte.

Allgemein möchte ich mich bei allen Mitarbeiteten des Instituts für Solarforschung am Standort Stuttgart bedanken. Besonders bei Dr.-Ing. Tobias Hirsch, der die jour fixe Termine in der Abwesenheit meines Betreuers übernommen hat. Besonderer Dank geht an meinem Betreuer, Dr.-Ing. Michael Wittmann, für die wöchentlichen jour fixe Termine, in denen er mir ausführlich zu allen Fragen und Problemstellungen mit Rat und Tat zur Seite stand. Auch möchte ich mich bei ihm dafür bedanken, dass er das Matlabskript für die Untersuchung der unterschiedlichen Zeitdiskretisierungen geschrieben hat, sowie für das Gegenlesen dieser Diplomarbeit.

Der Steag GmbH, insbesondere Dr. Reiner Pawellek, Dr. Tobias Löw und Dipl-Ing. Sergej Pulyaev, möchte ich für die Unterstützung und die kostenlose Bereitstellung der Software EBSILON®Professional danken.

Eine weitere Danksagung gilt meinem Betreuer an der TU München, Dipl.-Ing. Christoph Wieland. Besonders auch an Prof. Dr.-Ing. Hartmut Spliethoff, der diese Arbeit erst ermöglich hat.

Ein großes Dankeschön gilt meiner gesamten Familie, die mich während meines Studiums immer unterstützt hat. Besonders möchte ich meinem Vater, Lorenz Wagner, und meiner Mutter, Manuela Wagner, danken, ohne deren finanzielle und logistische Unterstützung diese Arbeit nie zustande gekommen wäre. Letztendlich möchte ich mich bei meiner Schwester, Melissa Wagner, bedanken, auf die ich mich immer verlassen kann, auch wenn sie gerade mehr als 7000 km von mir entfernt ist.